PITHA 94 / 21

Juni 1994

Measurement of the strong coupling constant α_s from jet rates in deep inelastic scattering

by

Richard Nisius

PHYSIKALISCHE INSTITUTE
RWTH AACHEN
Sommerfeldstr.
52056 AACHEN, GERMANY

Measurement of the strong coupling constant α_s from jet rates in deep inelastic scattering

Von der Mathematisch– Naturwissenschaftlichen Fakultät
der Rheinisch– Westfälischen Technischen Hochschule Aachen
genehmigte Dissertation zur Erlangung des akademischen Grades
eines Doktors der Naturwissenschaften

Vorgelegt von

Diplom– Physiker

Richard Nisius

aus Aachen

Referent	:	Universitätsprofessor Dr. Ch. Berger
Korreferent	:	Universitätsprofessor Dr. S. Bethke
Tag der mündlichen Prüfung	:	14.06.1994

Abstract

Based on $R_{2+1}(Q^2)$, the rate of (2+1)-jet events as defined by a modified JADE algorithm, the strong coupling constant α_s is measured as a function of the momentum transfer Q^2 in the range $10 < Q^2 < 4000\ GeV^2$, using data from deep inelastic electron proton scattering at the HERA collider. The result is consistent with the running of α_s according to the QCD prediction of the renormalization group equation. The extrapolation of the measured values to the mass of the Z° leads to $\alpha_s(M_z^2) = 0.121 \pm 0.015$. This preliminary result shows the sensitivity to α_s using jets in deep inelastic scattering. The method developed in this thesis will provide a precise measurement of α_s in future.

Contents

Chapter 1

Introduction

1.1 Motivation

The present understanding of high energy physics is based on interactions of fundamental spin 1/2 particles, called fermions, via the exchange of spin 1 particles, the gauge bosons (γ, Z°, $W^\pm$, g). The fermions are subdivided into quarks (q) and leptons (l) and occur in lefthanded doublets and righthanded singlets.

$$\begin{pmatrix} \nu_e \\ e^- \end{pmatrix}_L \begin{pmatrix} \nu_\mu \\ \mu^- \end{pmatrix}_L \begin{pmatrix} \nu_\tau \\ \tau^- \end{pmatrix}_L \begin{pmatrix} u \\ d \end{pmatrix}_L \begin{pmatrix} c \\ s \end{pmatrix}_L \begin{pmatrix} t \\ b \end{pmatrix}_L e_R^- \; \mu_R^- \; \tau_R^- \; u_R \; d_R \; c_R \; s_R \; t_R \; b_R$$

Figure 1.1: *The fundamental fermions. The leptons are called (l = e, μ, τ, ν_e, ν_μ, ν_τ) and the quarks are denoted by (q = u, d, c, s, t, b). L means lefthanded and R righthanded.*

From this basic pattern only the top quark and the ν_τ have not yet been observed directly in experiments. In addition the discovery of the spin 0 Higgs boson, which enters via the spontaneous electroweak symmetry breaking of the theory, is still missing. The discovery of the missing objects and the measurement of their properties are the mayor tasks of ongoing and future experiments.

All other particles, besides the gauge bosons, are built out of the fundamental fermions, for example, the proton (p) basically consists of three quarks ($p = u\ u\ d$). Given this basis, all observed phenomena in elementary particle physics can be described quantitatively with high precision in the framework of a gauge theory based on the group structure $U(1)_Y \times SU(2)_W \times SU(3)_C$ [1]. This theory, the theory of the standard model (SM), describes the electromagnetic, weak and strong interactions between elementary 'charged' fermions via exchange of gauge bosons. The gauge bosons only couple to particles which carry the corresponding 'charge'. In electromagnetism this charge is the well known electric charge, in strong interactions it is the 'colour' charge, for example the gluons couple to the coloured quarks in the proton.

One fundamental difference between the γ and $(Z^\circ, W^\pm, g)$ is that the former does not carry the 'charge' of the interaction it mediates, however, e.g. the gluon does, it is coloured. This means a gluon can interact directly with other gluons.

The strength of the interactions is controlled by coupling constants g_i. The values of the coupling constants are not predicted by the theory and have to be determined by experiments.

[1] The subscripts denote the 'charge', Hypercharge (Y), weak charge (W) and colour (C).

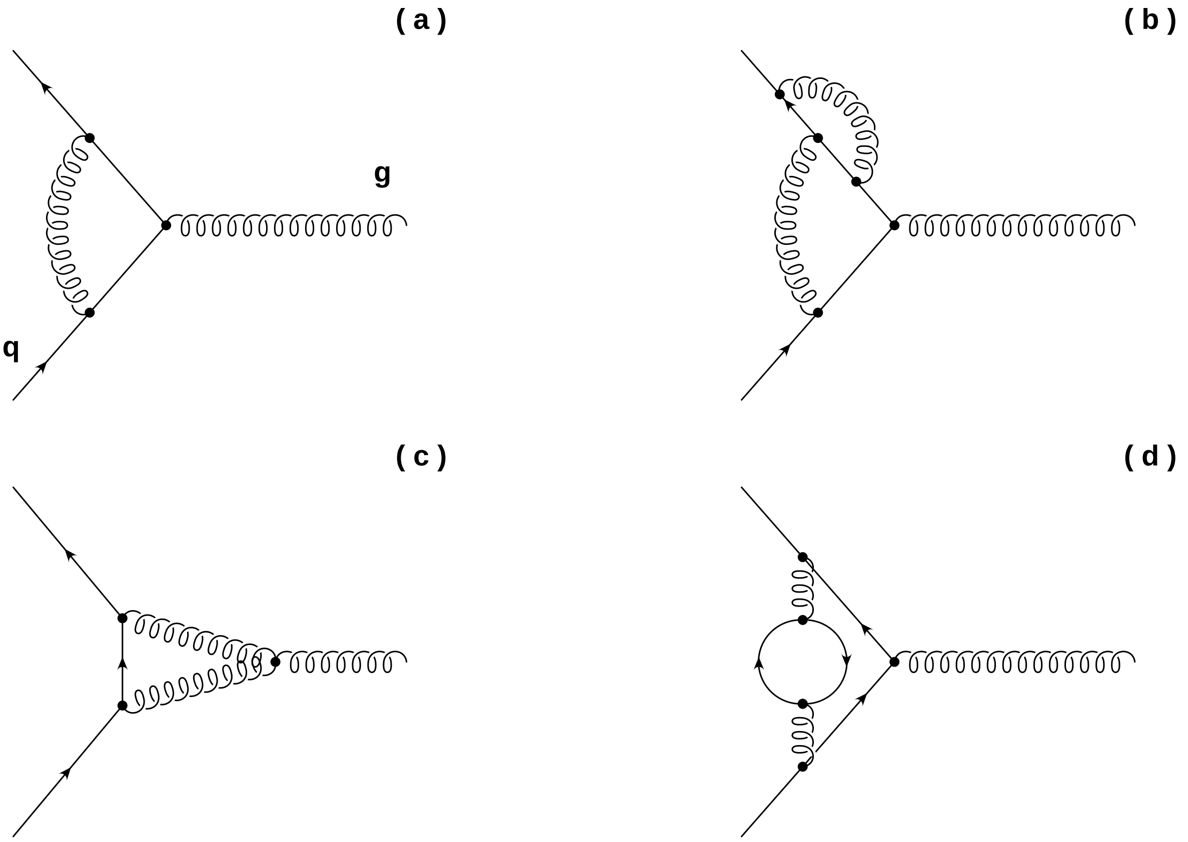

Figure 1.2: *Typical Feynman diagrams of the 1-loop and 2-loop corrections to the quark gluon vertex. The diagrams contain quarks (full lines) and gluons (wiggled line).*
(a,c) Examples of 1-loop Feynman diagrams
(b,d) Examples of 2-loop Feynman diagrams

In fact the so called constants depend on the renormalization scales μ_i^2 (see below). This is known as the running of coupling constants. The renormalization scales are usually identified with a typical energy scale of the interaction.

The basic idea to explain the running of the coupling constants is that one consideres the physical vacuum to be polarizable, like dielectric matter. With this feature screening of 'charge' is possible, and for example, in a scattering process the 'effective' charge depends on the kinematic circumstances. Technically in the framework of a gauge theory, one has to calculate the modifications to the couplings of the gauge bosons which mediate the force. In order to get finite probabilities for the interactions one has to reformulate the theory by absorbing infinite parts of the contributions into a redefinition of observables. This redefinition concerns masses, couplings and wave functions. For example the bare coupling constant is changed to give the renormalized one, which can be observed in experiments.

In Quantum Chromodynamics (QCD) [1] the modification of the coupling of gluons to other gluons and quarks have to be calculated. Typical diagrams which contribute are shown in figure 1.2. They are called loop diagrams since they contain closed paths of internal lines of quarks and gluons.

In Quantum Electrodynamics (QED) the corresponding diagrams are found to give a negative contribution, leading to screening of the electric charge. The closer one gets to the charge the stronger it acts, thus $g_1(\mu^2)$ increases with μ^2. In QCD the corrections are positive, resulting in 'anti screening' of the colour charge. The theoretical framework is given by the renormalization group theory. In the case of strong interactions, the running of g_3 or α_s ($g_3^2 \equiv g = 4\pi\alpha_s$) is described by equation 2.1, the renormalization group equation (RGE) of QCD. In deep inelastic scattering μ^2 is usually identified with the momentum transfer Q^2 (cf. section 3.1), the typical energy scale involved.

Due to its importance α_s has been determined using several observables in various reactions (cf. section 2.2). Most of the experiments have measured α_s at a particular center of mass energy. Identifying the center of mass energy with μ^2, this experimental constraint allows only to access the value of α_s at a fixed scale μ^2. In order to test the QCD prediction concerning the running of α_s, one has to combine measurements using several observables and/or different experiments and verify that they obey the predictions of the RGE. This involves the difficult treatment of partly common and partly different systematic uncertainties of the various experiments. A compilation of the results of α_s measurements can be found in [2].

Although α_s has been measured in various experiments, today it is still the fundamental parameter of the SM which is measured with the least accuracy (cf. table 1.1).

Variable	Value	relative error $\cdot 10^6$
$\alpha(m_{e^2})$	$1/137.0359895 \pm 0.0000061$	0.045
G_F/GeV^2	$1.16639 \cdot 10^{-5} \pm 0.00002 \cdot 10^{-5}$	17
$\sin^2\theta_W(\overline{MS})$	0.2325 ± 0.0008	3441
$\alpha_s(M_z^2)$	0.1134 ± 0.0035	31000

Table 1.1: *Measurements of fundamental parameters of the SM as quoted by the Particle Data Group [3].*
The velocity of light (c) and the Planck constant ($\hbar$) are set to unity $c = \hbar = 1$. This will be done throughout.

The different evolution behaviour of the coupling constants may result in a unification point at some large energy scale, where all forces act with equal strength. The extrapolation up to this scale needs as input the precise values obtained from the low energy measurements. As a consequence, for example predictions in the framework of supersymmetric theories as extensions of the SM mainly suffer from the inaccurate value for α_s [4], showing how important α_s measurements are.

The following will outline how, at HERA, one can test the prediction of QCD for the running of α_s at various scales by using only one observable in a single experiment.

1.2 How everything comes about

With the commissioning of HERA, the 'Hadron Elektron Ring Anlage', in 1992, a new way to determine α_s has been opened. At HERA a pointlike electron (e) scatters off a structured proton. The dominating process in ep scattering with high momentum transfer is the pure electromagnetic scattering of a quark inside the proton off an electron via single photon exchange. The electron radiates photons of various energies, this means the probed energy scale μ^2, identified with the momentum transfer Q^2 as discussed above, varies from event to event. This process is seen as a (1+1)-jet event, one jet originates from the hard subprocess and an additional jet results from the proton remnant [2]. In this case the hard interaction can be explained as purely electromagnetic scattering.

If the outgoing quark radiates a gluon, or if instead of a quark a gluon inside the proton is picked up then, to describe these reactions, one needs also predictions in the framework of QCD, which allows a calculation of the strength of the quark gluon coupling depending on α_s. These processes are (2+1)-jet events. Their rate is to first approximation proportional to α_s. From this it is evident that measuring the μ^2 dependence of the number of (1+1)-jet and (2+1)-jet events gives a handle on measuring, by using only this observable, the evolution of α_s with respect to μ^2 in one single experiment.

Following the description of the strategy, this thesis proposes a method for the measurement of α_s based on jets in ep interactions recorded with the H1 detector at HERA.

[2] For details see section 3.2.

Chapter 2

The strong coupling constant α_s

2.1 The running of α_s

The renormalization group equation controls the running of the strong coupling constant g, and as a consequence α_s ($g^2 = 4\pi\alpha_s$), as a function of the renormalization scale μ^2, provided g is small and perturbation theory is applicable.

$$\beta(g) = \mu^2 \frac{2\partial g}{\partial \mu^2} = -\frac{\beta_0}{(4\pi)^2} \cdot g^3 - \frac{\beta_1}{(4\pi)^4} \cdot g^5 + ... \tag{2.1}$$

The coefficients β_i can be calculated using the type of diagrams shown in figure 1.2 loop by loop. Keeping only the first term in the expansion and integrating within the limits $g(\mu^2), g^{'}(\mu^{'2})$ yields

$$\log \frac{\mu^2}{\mu'^2} = \frac{(4\pi)^2}{\beta_0} \left(\frac{1}{g^2} - \frac{1}{g'^2} \right) \tag{2.2}$$

This equation shows that the RGE relates the values of g or α_s at two different scales (e.g. $\mu^2, \mu^{'2}$). This means, if one measures the value at an arbitrary scale $\mu^{'2}$ the values at all other scales μ^2 are predicted by equation 2.2.

Although it is not necessary this relation is often rewritten by fixing one scale. Here the scale Λ^2 is chosen, so that the dependence on g' is replaced by a dependence on Λ^2. If one defines

$$\log \frac{\mu^{'2}}{\Lambda^2} = \frac{(4\pi)^2}{\beta_0} \frac{1}{g'^2} \tag{2.3}$$

and replaces g'^2 by Λ^2 in equation 2.2, the 1-loop [1] formula of α_s follows.

$$\alpha_s(\mu^2, \Lambda^2) \quad = \quad \frac{4\pi}{\beta_0 \log \frac{\mu^2}{\Lambda^2}} \tag{2.4}$$

If $\mu^2 \to \infty$ then $\alpha_s(\mu^2)$ approaches zero and the coupling vanishes. In this limit the particles are free, the so called asymptotic freedom of QCD. In 1-loop the definition of Λ is independent of the scheme in which the renormalization, given below, of the coupling is performed.

[1] It is called 1-loop expression because it is based on the calculation of 1-loop diagram corrections to the gluon propagator (cf. figure 1.2).

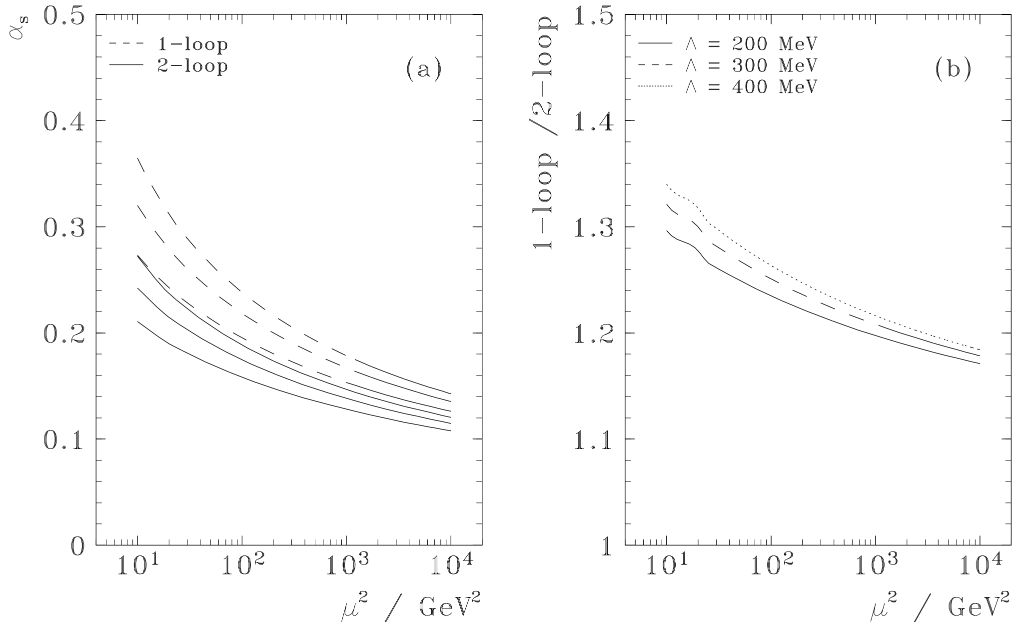

Figure 2.1: *The 1-loop and 2-loop α_s expressions at different Λ values.*
(a) α_s in 1-loop (dashed line) and 2-loop (full line) approximation as a function of μ^2 for $\Lambda_{4,\overline{MS}} = 400, 300, 200$ MeV from top to bottom.
(b) The 1-loop expression divided by the 2-loop formula for the three Λ values as a function of μ^2.

In general the coupling constant can be expressed as a series in $(\log \frac{\mu^2}{\Lambda^2})^{-n}$, where $n = 1, 2, \ldots$. If one keeps the first two terms of the RGE one gets, in a similar way as equation 2.4, the well known 2-loop formula for α_s.

$$\alpha_s(\mu^2, \Lambda_{n_f,\overline{MS}}) = \frac{4\pi}{\beta_0 \cdot L} \cdot \left(1 - \frac{\beta_1}{\beta_0^2} \cdot \frac{\log L}{L}\right) \tag{2.5}$$

with:

$$\beta_0 = \frac{33 - 2 \cdot n_f}{3}, \quad \beta_1 = \frac{306 - 38 \cdot n_f}{3}, \quad L = \log\left(\frac{\mu^2}{\Lambda^2_{n_f,\overline{MS}}}\right)$$

Here the term proportional to $(\log \frac{\mu^2}{\Lambda^2})^{-2}$ is absorbed into the definition of Λ. This choice of renormalizing the coupling constant is called the modified minimal subtraction scheme ($\overline{MS}$) and the corresponding Λ is named $\Lambda_{n_f,\overline{MS}}$.

The coefficients β_0 and β_1 contain n_f, which is the number of active quark flavours. This number changes as a function of μ^2. Loosely speaking, if μ^2 is smaller than the mass m_f^2 of a quark of flavour f ($f = u, d, \ldots$) this quark flavour cannot be produced and it does not count in n_f. This gives a discontinuity in the description. On the other hand α_s is a continuous function and correspondingly $\Lambda_{n_f,\overline{MS}}$ has to change if a quark mass boundary is crossed. There exist different recipes for changing n_f, the one used in this thesis is the definition of Marciano [5] [2]. The boundary requirement fixes the relation between the $\Lambda_{n_f,\overline{MS}}$ values e.g.

$$\begin{aligned}
\alpha_s(m_b^2, \Lambda^2_{5,\overline{MS}}) &= \alpha_s(m_b^2, \Lambda^2_{4,\overline{MS}}) \\
\Lambda_{5,\overline{MS}} &\approx \Lambda_{4,\overline{MS}} \cdot \left(\Lambda_{4,\overline{MS}}/m_b\right)^{2/23} \cdot \left[\log \frac{m_b^2}{\Lambda^2_{4,\overline{MS}}}\right]^{-963/13225} \qquad (2.6) \\
\Lambda_{5,\overline{MS}} &\approx 0.66 \cdot \Lambda_{4,\overline{MS}} \qquad \text{for } \Lambda_{4,\overline{MS}} = 200\, MeV
\end{aligned}$$

This shows the importance of quoting Λ together with n_f (cf. figure 2.2 (b)). In the 1-loop approximation this is not important, because a change in Λ only changes the higher order term. This can be seen by a similar calculation as the one given in section 2.2 for the variation in the renormalization scale. Using the 1-loop equation one may simply use a single Λ value at all scales, the choice of Λ is not fixed.

In the following the numerical differences of the 1-loop and 2-loop equations are investigated. Figure 2.1 (a) shows the 1-loop and 2-loop expression of α_s as a function of μ^2. As seen from equation 2.5 the α_s value rises with $\Lambda_{4,\overline{MS}}$. The lines in figure 2.1 (a) correspond to $\Lambda_{4,\overline{MS}} = 400, 300, 200\ MeV$ with $400\ MeV$ giving the highest curve. Due to the negative sign of the second term, the 2-loop expression reduces α_s compared to the 1-loop equation. The relative amount changes with μ^2 as seen from figure 2.1(b) which shows the ratio of 1-loop and 2-loop expressions for the three $\Lambda_{4,\overline{MS}}$ values. The difference rises with decreasing μ^2 and amounts to $30 - 35\,\%$ at $\mu^2 = 10\ GeV^2$.

Even within the 2-loop expression the variation with $\Lambda_{4,\overline{MS}}$ is large. Figure 2.2 (a) shows the ratio of α_s for $\Lambda_{4,\overline{MS}} = 300$ and $400\ MeV$ divided by α_s for $\Lambda_{4,\overline{MS}} = 200\ MeV$ as a function of μ^2. A change in $\Lambda_{4,\overline{MS}}$ of from 200 to 400 MeV at $\mu^2 = 10\ GeV^2$ gives a $29\,\%$ change of α_s. The same change in $\Lambda_{4,\overline{MS}}$ at $\mu^2 = M_z^2$ would change α_s only by $12\,\%$, which shows the higher sensitivity to $\Lambda_{4,\overline{MS}}$ at low μ^2 values. This sensitivity is demonstrated in figure 2.3. Shown is the error band on $\Lambda_{4,\overline{MS}}$ which would be reached if one measures α_s at a particular μ^2 with a precision of $10\,\%$. The three curves correspond to the assumption that the measured α_s value leads to a central value of $\Lambda_{4,\overline{MS}} = 400, 300, 200\ MeV$. Two observations can be made, firstly the sensitivity decreases with μ^2 and secondly the higher the Λ value the broader is the error band. A measurement of α_s, corresponding to $\Lambda_{4,\overline{MS}} = 200\ MeV$ at $\mu^2 = 10\ GeV^2$, constrains $\Lambda_{4,\overline{MS}}$ to $\approx^{+65}_{-60}\ MeV$, whereas at $\mu^2 = 10^3\ GeV^2$ $\Lambda_{4,\overline{MS}}$ is only measured with a precision of $\approx^{+130}_{-90}\ MeV$.

Results are usually quoted in terms of $\Lambda_{4,\overline{MS}}$ or $\Lambda_{5,\overline{MS}}$, in order to translate between both the equation 2.6 is shown in figure 2.2 (b). As a convention, in the following, $\Lambda_{4,\overline{MS}}$ is abbreviated with Λ unless stated differently.

[2]For example, it can either by changed at m_q^2 or $(2m_q)^2$, the choice made is m_q^2.

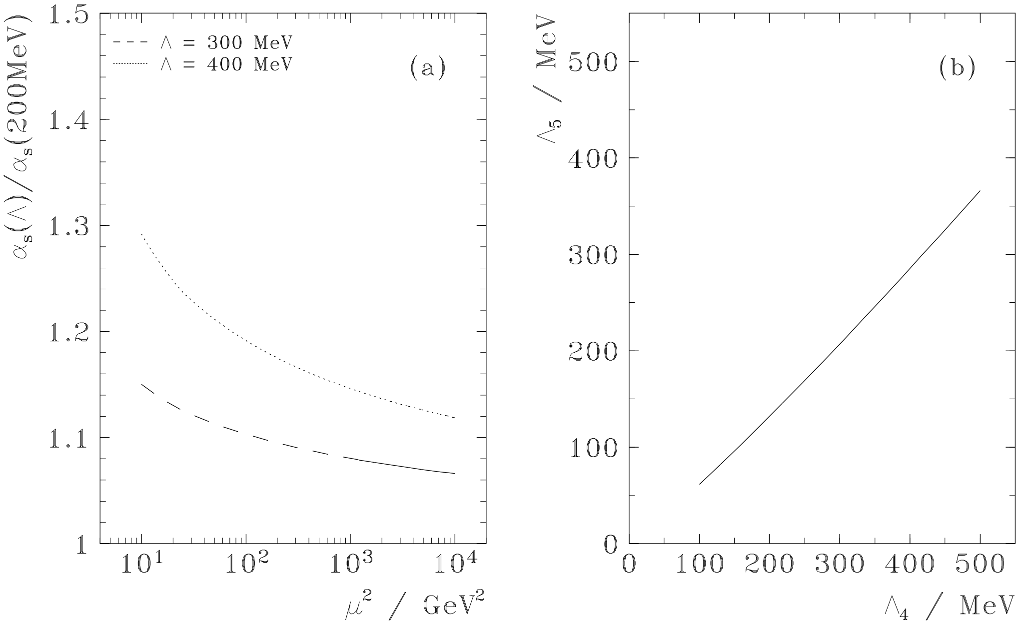

Figure 2.2: *The variation of α_s in 2-loop with Λ as a function of μ^2.*
(a) The α_s variation with Λ as a function of μ^2.
(b) The relation between $\Lambda_{4,\overline{MS}}$ and $\Lambda_{5,\overline{MS}}$.

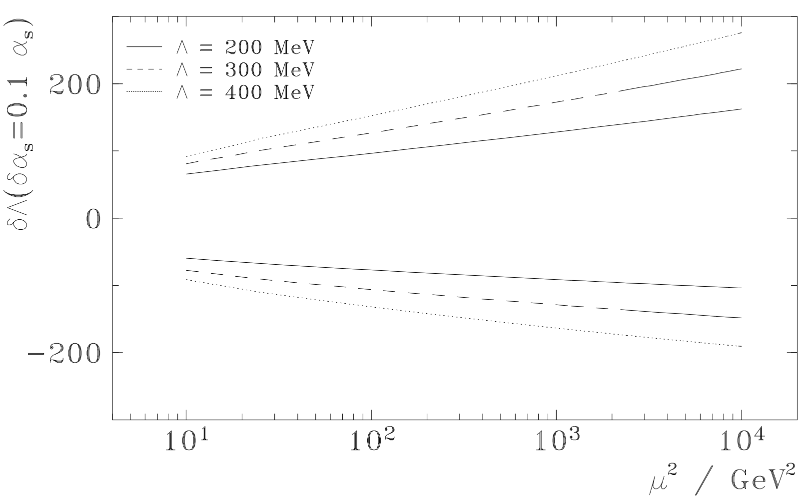

Figure 2.3: *The Λ variation for a fixed relative α_s change of* 10 %*. For explanation see text.*

2.2 Status of α_s determinations

The strong coupling constant has been measured with different observables at various experiments. A compilation of the present status can be found in table 2.1 obtained from [6].

Process	Q [GeV]	$\alpha_s(Q)$	$\alpha_s(M_{Z^0})$	$\Delta\alpha_s(M_{Z^0})$ exp.	$\Delta\alpha_s(M_{Z^0})$ theor.	Theory
GLS [ν-DIS]	1.73	0.32 ± 0.05	0.115 ± 0.006	0.005	0.003	NNLO
R_τ [LEP]	1.78	0.360 ± 0.040	0.122 ± 0.005	0.002	0.004	NNLO
DIS [ν]	5.0	$0.193\ ^{+0.019}_{-0.018}$	0.111 ± 0.006	0.004	0.004	NLO
DIS [μ]	7.1	0.180 ± 0.014	0.113 ± 0.005	0.003	0.004	NLO
$c\bar{c}$ mass splitting	5.0	0.174 ± 0.012	0.105 ± 0.004	0.000	0.004	LGT
$J/\Psi + \Upsilon$ decays	10.0	$0.167\ ^{+0.015}_{-0.011}$	$0.113\ ^{+0.007}_{-0.005}$	0.001	$^{+0.007}_{-0.005}$	NLO
e^+e^- [σ_{had}]	34.0	$0.146^{+0.031}_{-0.026}$	$0.124^{+0.021}_{-0.019}$	$^{+0.021}_{-0.019}$	–	NLO
e^+e^- [ev. shapes]	35.0	0.14 ± 0.02	0.119 ± 0.014	–	–	NLO
e^+e^- [ev. shapes]	58.0	0.130 ± 0.008	0.122 ± 0.007	0.003	0.007	NLO
$p\bar{p} \to b\bar{b}X$	20.0	$0.138\ ^{+0.028}_{-0.019}$	$0.109\ ^{+0.016}_{-0.012}$	$^{+0.012}_{-0.007}$	$^{+0.011}_{-0.010}$	NLO
$p\bar{p} \to$ W jets	80.6	0.123 ± 0.025	0.121 ± 0.024	0.017	0.016	NLO
$\Gamma(Z^0 \to \mathrm{had.})$	91.2	0.122 ± 0.008	0.122 ± 0.008	0.007	0.004	NNLO
Z^0 [ev. shapes]	91.2	0.119 ± 0.006	0.119 ± 0.006	0.001	0.006	NLO
Z^0 [ev. shapes]	91.2	0.123 ± 0.006	0.123 ± 0.006	0.001	0.006	resum.

Table 2.1: *A Summary of measurements of α_s from [6]. The α_s values are obtained using the solution to the RGE to $\mathcal{O}(\alpha_s^3)$. The abbreviations NLO, NNLO and resum. are explained in section 3.2 and 5.2.*

Very precise measurements are derived from event shape variables at the Z° pole from e^+e^- annihilations at LEP, and from scaling violations in structure functions of deep inelastic neutrino nucleon ($\nu\mathcal{N}$) or muon nucleon ($\mu\mathcal{N}$) scattering (DIS [ν],DIS [μ] in table 2.1). An interesting effect is that the DIS and LEP measurements differ by one standard deviation, with DIS giving the lower α_s value.

Motivated by the subject of this work, the measurements from jet rates are reviewed in more detail. Figure 2.4 shows the various measurements from jet rates and table 2.2 gives the present status of these measurements from the LEP experiments [7]. The extracted mean value is $\alpha_s = 0.119 \pm 0.010$ that means an 8 % error. In principle the evaluation is done as follows, for details see [7]. Using a Monte Carlo based on the parton shower approach (cf. section 7.1.2) which describes the observed data with high precision, the measured data distributions are

	ALEPH	DELPHI	L3	OPAL	average
$\alpha_s(M_z^2)$	0.119 ± 0.012	0.118 ± 0.010	0.116 ± 0.012	$0.120 ^{+0.009}_{-0.008}$	0.119 ± 0.010
$\Lambda_{5,\overline{MS}}\,[MeV]$	$239 ^{+197}_{-125}$	$226 ^{+153}_{-104}$	$202 ^{+177}_{-110}$	$253 ^{+144}_{-94}$	$239 ^{+158}_{-108}$
$\Lambda_{4,\overline{MS}}\,[MeV]$	$341 ^{+243}_{-165}$	$325 ^{+191}_{-138}$	$293 ^{+221}_{-150}$	$359 ^{+179}_{-123}$	$341 ^{+197}_{-143}$

Table 2.2: *α_s measurements at LEP with jets in E0 scheme (cf. table 4.1) using fixed order perturbative QCD predictions. The α_s values in this table are from table 1 in [7].*

corrected for detector acceptance and resolution. The errors of this procedure are derived using different parametrizations of the detector simulation. The hadronization correction is applied and checked using different fragmentation models or varying parameters within one model. In total these errors amount to $\approx 1-3\,\%$.

It was shown by OPAL that by applying only these corrections, for different observables, the deduced α_s values disagree significantly [8], the reason being the unknown higher order perturbative corrections, which may be different for the various observables. These uncertainties are usually parametrized by variation of the renormalization scale μ^2, since in infinite order perturbation theory the result should not depend on the choice of μ^2, while in finite order it does.

The choice of scale to use as the renormalization scale μ^2 is not defined by first principles in QCD. What is most commonly used is a 'typical' scale of the process e.g. μ^2 equals M_z^2 at LEP. For gluon radiation from an outgoing quark in e^+e^- scattering another reasonable scale is the transverse momentum of the gluon with respect to the quark. This is numerically important, because, a change in the scale e.g. μ^2 to μ'^2 is equivalent to a change in the coefficient of the higher order terms of the perturbative expansion [9]. Starting from the leading order formula, equation 2.4, one derives:

$$
\begin{aligned}
\frac{\partial \alpha_s}{\partial \log \mu^2} &= -\frac{4\pi}{\beta_0}(\log \frac{\mu^2}{\Lambda^2})^{-2} \\
\frac{\alpha_s(\mu'^2) - \alpha_s(\mu^2)}{\log \mu'^2 - \log \mu^2} &= -\frac{\beta_0}{4\pi}\alpha_s^2(\mu^2) \\
\alpha_s(\mu'^2) &= \alpha_s(\mu^2) \cdot \left[1 + \frac{\beta_0}{4\pi} \cdot \log \frac{\mu^2}{\mu'^2} \cdot \alpha_s(\mu^2)\right] \qquad (2.7)
\end{aligned}
$$

So in the 1-loop approximation, α_s does not change while changing $\mu^2 \rightarrow \mu'^2$. As can be seen from equation 2.7 the change in α_s introduced by a change in μ^2 is proportional to α_s^2. This means, although the numerical value of α_s changes while changing μ^2 in equation 2.4, formally in the framework of a perturbative expansion this change appears only the 2-loop coefficient, the 1-loop coefficient remains unchanged. Therefore, only calculations using the 2-loop formula are useful to measure α_s. Changing the scale means only reorganizing the relative sizes of the terms in the perturbative expansion. In principle, if a dimensionless observable $\hat{O}(\mu^2)$ is calculated to all orders the choice does not matter, the dependence on the unphysical scale μ^2

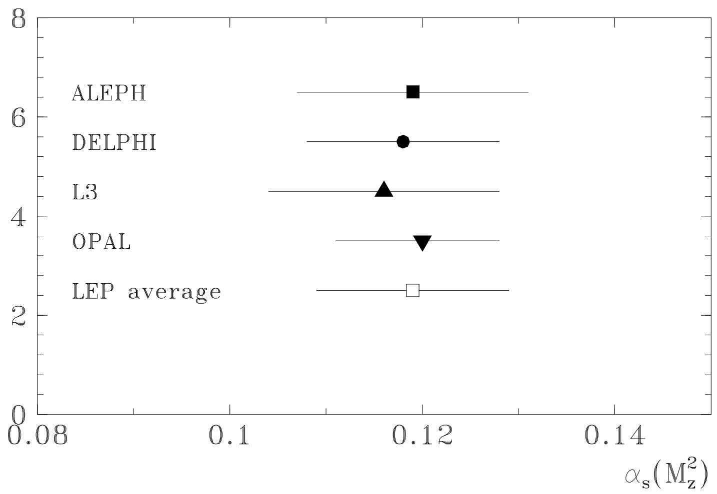

Figure 2.4: *Status of α_s measurements from jet rates at LEP using fixed order perturbative QCD predictions (cf. table 2.2).*

must vanish.

$$\mu^2 \frac{d}{d\mu^2} \widehat{O}(\mu^2) = 0 \tag{2.8}$$

However only calculations to finite order are available, and a number of theoretically motivated concepts are suggested, to 'decide' what is the best scale to use.

One is the principle of fastest apparent convergence [10], which means one chooses μ^2 such that the term of highest calculated order vanishes. Another attempt is the principle of minimal sensitivity [11], which is a scheme where one chooses μ^2 at the point where the derivative with respect to μ^2 vanishes. The μ^2 value corresponds to a local extreme of $\widehat{O}(\mu^2)$, where the variation is smallest. Finally the effective charge scheme [12] is mentioned. Although the motivations are different the various attempts suggest scales μ^2 which are smaller than M_z^2 for e^+e^- [7], resulting in higher α_s values.

From an experimental point of view, without any theory inspired model, one may simply regard μ^2 as a free parameter and fit it to the data.

In general if any of these approaches leads to a scale μ^2 which is far away from the typical mass scale of the process e.g. M_z^2 at LEP, this is an indication that the theoretical expression is unreliable [3], and because of the reorganizing of terms by changing the scale (cf. equation 2.7) it can be interpreted as a hint for important higher order corrections. With this in mind it is clear that evaluating a scale error is a difficult task.

Usually at LEP a parameter $x_\mu = \mu^2/M_z^2$ is introduced and varied in a reasonable range resulting in a scale error which is the main source of the theoretical uncertainty. It accounts for an error in the order of 10 % on α_s and it is different for various observables [7]. The low values for μ^2 favoured in the LEP jet analysis, where data is compared to second order calculations,

[3] Then $\log(\mu^2/M_z^2)$ is large and the convergence of the series may be spoiled as well.

shows the importance of higher order terms and lead to the concept of resummed calculations (cf. section 5.2) to account for at least a part of them. The results of the LEP experiments show a much reduced scale dependence (x_μ close to 1) for observables calculated with resummed higher order terms [7].

The scale problem will also be observed in DIS scattering. Here it is even more complex because more scales are involved in the hard scattering process (cf. section 3.1) and in addition one has to deal with the scales in the parton density functions (cf. section 3.3).

Because of the logarithmic dependence of α_s on μ^2 the relative error of $\alpha_s(M_z^2)$ is smaller if one measures α_s at a lower energy scale and consequently at a lower μ^2 (cf. figure 2.3), however the result is in general less reliable for two reasons. First, at low μ^2 the evolution parameter α_s is large, indicating that the justification to use perturbation theory gets weaker, and second non perturbative effects, meaning terms of the form $(\Lambda/\mu)^N$, namely target mass effects and higher twist contributions, play a more important role. They vanish for $\mu^2 \to \infty$.

First indication that an α_s determination, using the hadronic final state in deep inelastic scattering, may be possible is reported from the E665 Collaboration. The dependence of the average squared transverse energy of jets, which in leading order is proportional to α_s, is studied in $(\mu \mathcal{N})$ scattering [13]. The data are corrected to the hadron level and then compared to a leading order parton level QCD prediction in the range $3 < Q^2 < 25\ GeV^2$.

Chapter 3

Deep inelastic scattering DIS

The term deep inelastic scattering (DIS) denotes the process in which a lepton l, either charged (e, μ), or neutral ($\overset{(-)}{\nu_e}$, $\overset{(-)}{\nu_\mu}$), scatters off a nucleon $\mathcal{N}$ ($\mathcal{N} = p,\ n$), involving a large momentum transfer ($Q^2 \gg \Lambda^2$). This interaction is mediated via a neutral (γ, Z°) or charged ($W^\pm$) boson and is called a neutral current (NC) and a charged current (CC) interaction respectively.

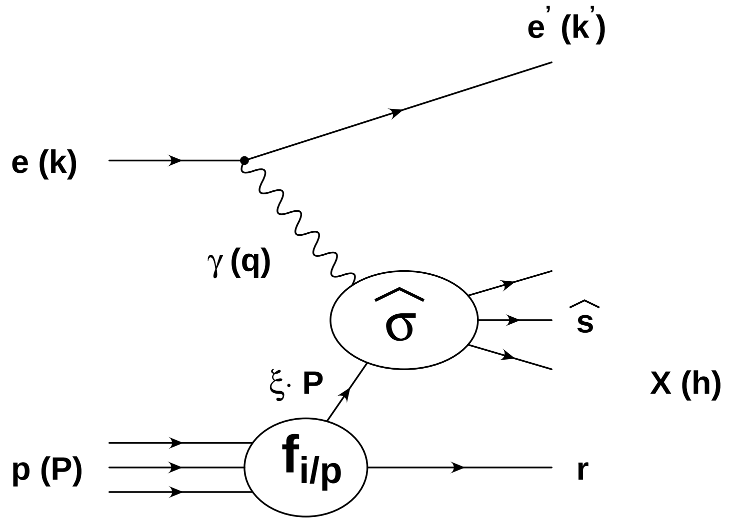

Figure 3.1: *The neutral current deep inelastic scattering process.*

At HERA the incoming lepton is an electron traveling in the -z direction in the laboratory system [1], with four momentum $k = (E, 0, 0, p_z) = (26.7, 0, 0, -26.7)\ GeV$. The nucleon is a proton of momentum $P = (E_p, 0, 0, p_{z\,p}) = (820, 0, 0, 820)\ GeV$. The following consideration is restricted to the NC case with single photon exchange.

3.1 Kinematic variables in DIS

The NC process (cf. figure 3.1) where the electron (e) scatters off a proton (p) producing an electron (e') and a hadronic final state (X) can be written as

[1]The +z or forward direction is the direction of motion of the incoming proton. The scattering angles are calculated with respect to this axis.
In this notation a four vector is given as $p = (E, p_x, p_y, p_z)$.

$$e(k)\ p(P) \rightarrow e^{'}(k^{'})X(h)$$

The symbols in brackets represent the four vectors of the particles, $k^{'} = (E_e, p_{x\,e}, p_{y\,e}, p_{z\,e})$ and $h = (E_h, p_{x\,h}, p_{y\,h}, p_{z\,h})$. In this process the ep center of mass energy is given by

$$s_{ep} = (P + k)^2 = 2Pk \tag{3.1}$$

In the last step particle masses have been neglected which will be done throughout. This is a good approximation as the momenta of the particles are much larger than their masses. With the four vectors of the incoming electron and proton it follows $s_{ep} = 4 \cdot E \cdot E_p \approx 295^2\ GeV^2$ for HERA.

The exchanged virtual boson has the invariant mass q which is derived from the electron variables as

$$q^2 = (k - k^{'})^2 \tag{3.2}$$

The momentum transfer $Q^2 > 0$ is defined as the negative mass squared of the boson.

$$Q^2 \equiv -q^2 \tag{3.3}$$

If one introduces the two Bjorken scaling variables x, y defined by

$$x \equiv \frac{Q^2}{2Pq} \tag{3.4}$$

$$y \equiv \frac{Pq}{Pk} \tag{3.5}$$

the four vector of the outgoing electron is fixed. The last three equations however are interrelated, as

$$Q^2 = x \cdot y \cdot s_{ep} \tag{3.6}$$

The global event kinematic can be described by two independent variables, the most commonly used are x and Q^2.

Other useful variables are the boson proton center of mass energy $s_{\gamma p}$ which is equivalent to the total hadronic mass squared W^2,

$$s_{\gamma p} = (P + q)^2 = 2Pq - Q^2 = y \cdot s_{ep} - Q^2 = Q^2\frac{1-x}{x} \equiv W^2 \tag{3.7}$$

and the mass squared $\hat{s}$ of the hard subsystem.

$$\hat{s} = (\xi P + q)^2 = 2\xi Pq - Q^2 \tag{3.8}$$

Here ξ denotes the momentum fraction of the proton carried by the incoming parton entering the hard interaction. Insertion of x in equation 3.8 leads to the relation between the Bjorken x value and ξ.

$$\xi = x(1 + \frac{\hat{s}}{Q^2}) \tag{3.9}$$

This shows that only for a massless hard subsystem $\hat{s} = 0$ the momentum fraction ξ equals the Bjorken x value, otherwise $\xi > x$.

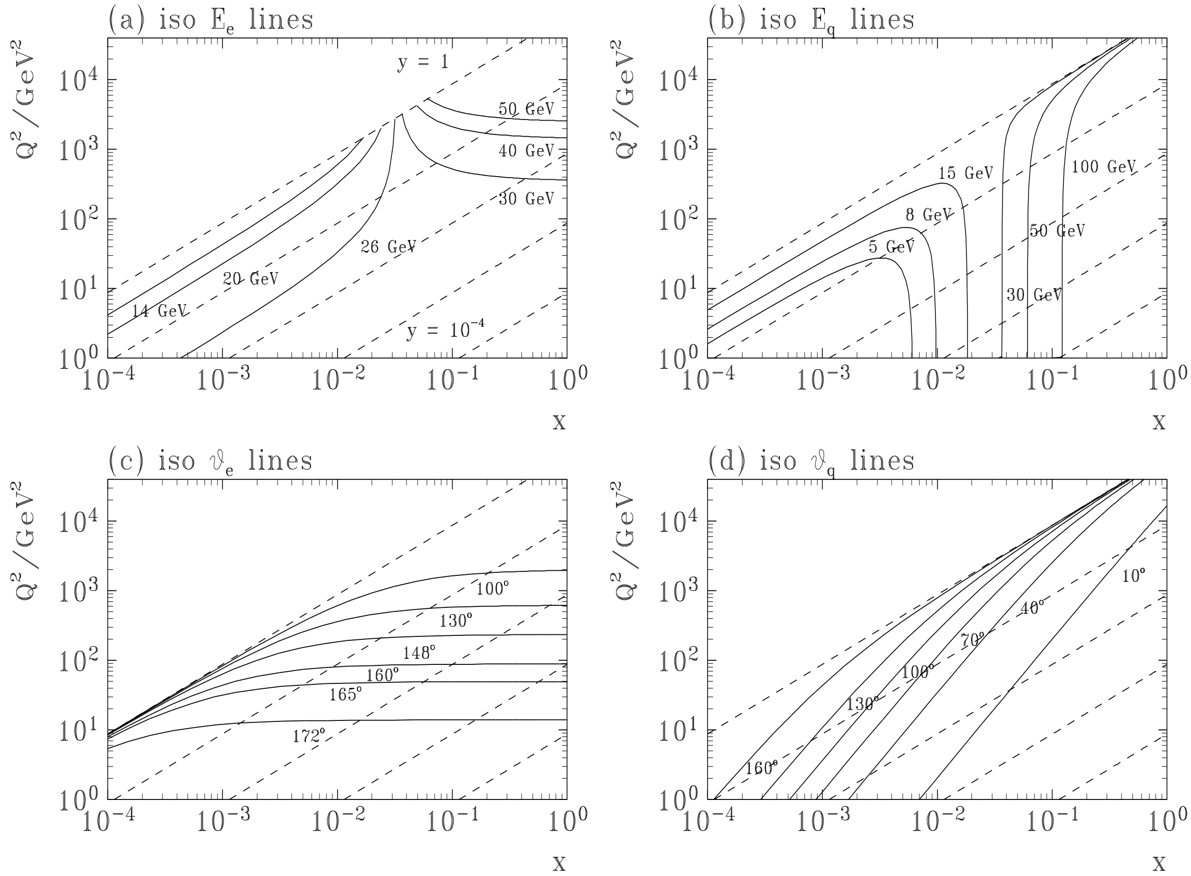

Figure 3.2: *Basic kinematic quantities in DIS. All figures show the (x, Q^2) plane with lines for fixed values of y, one per decade. The leftmost line corresponds to $y = 1$ and the rightmost to $y = 10^{-4}$. The four different figures each show lines of constant values for one particular quantity. Two concern the scattered electron and two the scattered quark in the simple case $\hat{s} = 0$.*

(a) The energy of the scattered electron.
(b) The energy of the scattered quark.
(c) The polar angle of the scattered electron.
(d) The polar angle of the scattered quark.

Altogether the kinematic situation is very complex in this highly asymmetric situation. Figure 3.2 shows kinematic quantities of the electron and a massless hard subsystem in terms of isolines in energy and polar angles. To guide the eye iso y lines are drawn as well.

If one measures both the hadronic final state and the scattered electron the event is over-constrained. One can either use the electron energy (E_e) and angle (ϑ_e), or the hadronic final state alone to measure the basic kinematic quantities.

The electron measurement is obtained via,

$$\begin{aligned}
y_e &= \frac{Pq}{Pk} = \frac{P(k-k')}{Pk} = 1 - \frac{E_e - p_{ze}}{2E} \\
Q_e^2 &= -q^2 = -(k-k')^2 = 2kk' = 2(EE_e - \vec{k}\vec{k'}) = 2EE_e(1 + cos\vartheta_e) \\
Q_e^2 &= \frac{p_{Te}^2}{1 - y_e} \\
x_e &= \frac{Q_e^2}{s_{ep} y_e}
\end{aligned} \tag{3.10}$$

and the hadron measurement via

$$\begin{aligned}
y_h &= \frac{Pq}{Pk} = \frac{P(P_h - P)}{Pk} = \frac{E_P(E_h - p_{zh})}{2EE_P} = \frac{E_h - p_{zh}}{2E} \\
Q_h^2 &= \frac{p_{Th}^2}{1 - y_h} \\
x_h &= \frac{Q_h^2}{s_{ep} y_h}
\end{aligned} \tag{3.11}$$

There exist various other methods to calculate the kinematic variables [14] which are combinations of hadronic and leptonic measurements. Which method to use in which kinematic regions should be decided in terms of resolution and systematic shifts of the mean values.

3.2 DIS in terms of parton- scattering

Now a closer look to the electron proton scattering in the DIS regime will be done. This is the region where α_s is small and perturbation theory is applicable. Due to the Heisenberg relation

$$\Delta r \Delta p \geq \hbar \tag{3.12}$$

high momentum transfer is equivalent to short distances. Then the partonic content of the proton is resolved by the photon. It interacts directly with the quarks in the proton with a certain probability. The probabilities for this elementary processes can be calculated with the help of the Feynman rules which allows the cross section of the NC process to be expressed as a power series in α_s.

$$\sigma_{tot} = \sum_{N=0}^{\infty} \sigma_N = a_0 \alpha_s^o + a_1 \alpha_s^1 + a_2 \alpha_s^2 + \ldots \tag{3.13}$$

The contribution to the σ_N can be illustrated by Feynman diagrams to a given order in α_s^N. In this picture the electron delivers the photon and the proton the partons which enter the hard scattering process.

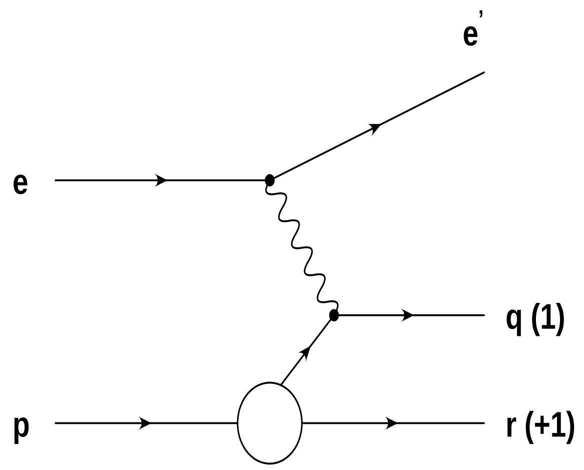

Figure 3.3: *The lowest order $\mathcal{O}(\alpha_s^o)$ Feynman diagram of ep scattering.*

To be more specific, the lowest order in this perturbative expansion describes the purely electromagnetic $\gamma q \rightarrow q'$ scattering. The probe of the quark with the photon splits the process into two parts. The time before the photon hits the quark is called the initial state (IS), everything afterwards the final state (FS), where both parts will interfere.

This scattering (cf. figure 3.3) leads to two outgoing partons, the struck quark q (1) and the leftover part from the proton the remnant, which in this simplest case is a diquark dq [2] To account for more complex situations for the proton remnant it will be denoted with r and counted separately as (+1) in this counting scheme. This scattering leads to a (1+1) parton final state, described in the naive QPM, where the proton is modeled as consisting of three valence quarks ($p = u\ u\ d$) which share the momentum of the proton while having no intrinsic transverse momentum. Formally this reaction is to order $\mathcal{O}(\alpha_s^o)$.

More complex scattering is described in the framework of QCD. Each coupling to a gluon gives rise to a factor α_s in the cross section. Two graphs containing one gluon each exist to $\mathcal{O}(\alpha_s)$.

- Similar to photon radiation of charged particles the quarks can radiate gluons as long as the uncertainty relation is fulfilled. A virtual gluon in turn can decay into a $q\bar{q}$ pair. If during this fluctuation one of the resulting quarks is probed by the photon this leads to a boson gluon fusion (BGF) event sketched in figure 3.4 (a).

- Analogous to the Compton scattering in QED the radiation of a gluon off a quark is called QCD Compton (QCDC) process, figure 3.4 (b). The gluon can be emitted before or after the quark interacts with the photon. These two possibilities result in the same final state, which means according to the Feynman rules their contributions have to be added on the amplitude level.

Now there are (2+1) partons in the final state, (q, $\bar{q}$) or (q, g) and the remnant r (+1) as before. From this one finds the general rule that the leading order (LO) contribution [3] to a (N+1) parton final state is of $\mathcal{O}(\alpha_s^{N-1})$.

[2] To use the term parton for a structured object like the diquark is not correct, however it is treated as one single object in the whole consideration and therefore it is denoted as parton as if it were fundamental.

[3] The contribution proportional to the lowest occuring power in α_s.

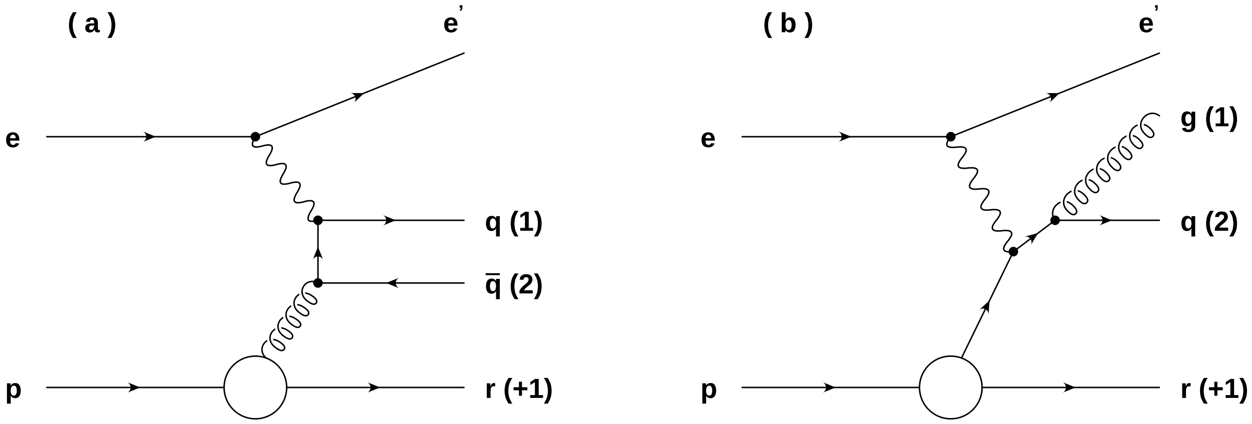

Figure 3.4: *First order $\mathcal{O}(\alpha_s)$ Feynman diagrams of ep scattering.*
(a) The boson gluon fusion graph.
(b) The QCD Compton graph.

Each extra gluon gives rise to an extra power of α_s. Also a virtual gluon at the γ q vertex generates a process to $\mathcal{O}(\alpha_s)$ but leads only to a (1+1) parton state, figure 3.5 (a). These types of graphs are in an obvious notation called next to leading order (NLO) contributions.

To $\mathcal{O}(\alpha_s^2)$ one gets a series of new Feynman diagrams (cf. figure 3.6) giving (3+1) partons in the final state. For the first time this includes the triple gluon vertex. [4]

To $\mathcal{O}(\alpha_s^2)$ one gets also next to leading order contributions to the (2+1) parton final state figure 3.7 and even next to next to leading order (NNLO) contribution, figure 3.5 (b), to the (1+1) parton final state.

In principle the series can be extended to all orders in α_s. As can be seen already from $\mathcal{O}(\alpha_s^2)$, the number of graphs which have to be calculated increases rapidly from order to order and in practice one can not expect calculations to all orders to become available. A partial solution to that problem is the method of resummed calculations which accounts for the leading logarithmic terms to all orders. The basis of this technique as well as the status of calculations will be addressed in section 5.2.

Available at the moment is a fixed order calculation to $\mathcal{O}(\alpha_s^2)$ with some limitations (cf. section 5.1).

These partons only 'exist' in the ideal world of theoretical calculations, they are not accessible in an experiment, however after hadronization they will manifest as jets in the detector, which is the subject of chapter 4.

3.3 The parton density functions

The basic concept for introducing parton density functions (PDF's) is the theorem of factorization [16], which says that cross sections (σ) can be written as convolutions of matrix elements or partonic hard scattering cross sections ($\hat{\sigma}$) based on basic Feynman diagrams (as discussed

[4] Because the field quanta interact among each other, the existence of this vertex is the manifestation of the non abelian character of QCD. Isolating this process is of major interest, but needs the possibility of telling quarks from gluons, which is not easy after hadronization [15].

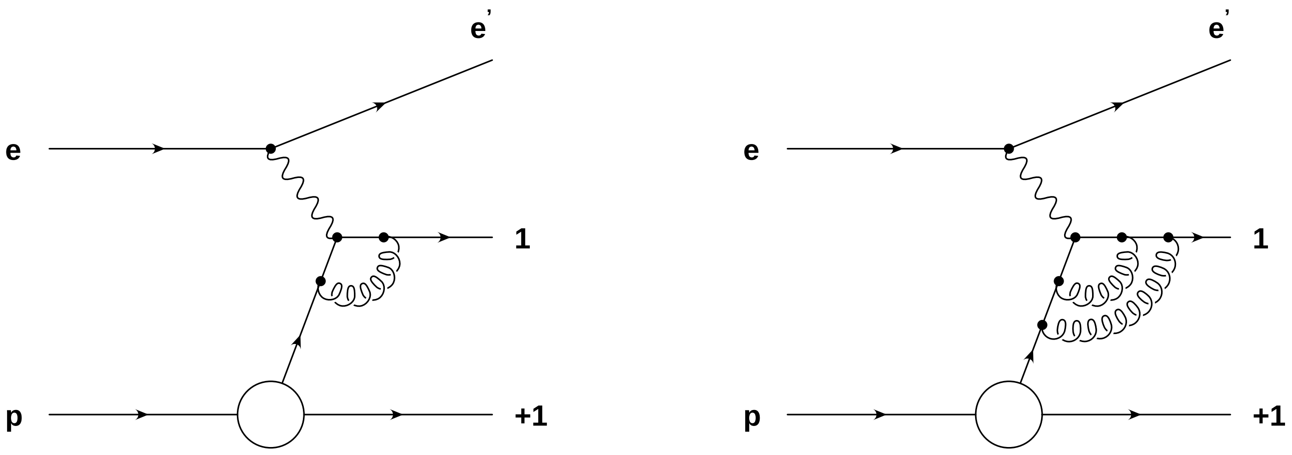

Figure 3.5: *Virtual corrections to the (1+1) parton final state in ep scattering.*
(a) The NLO virtual correction to $\mathcal{O}(\alpha_s)$.
(b) A NNLO virtual correction to $\mathcal{O}(\alpha_s^2)$.

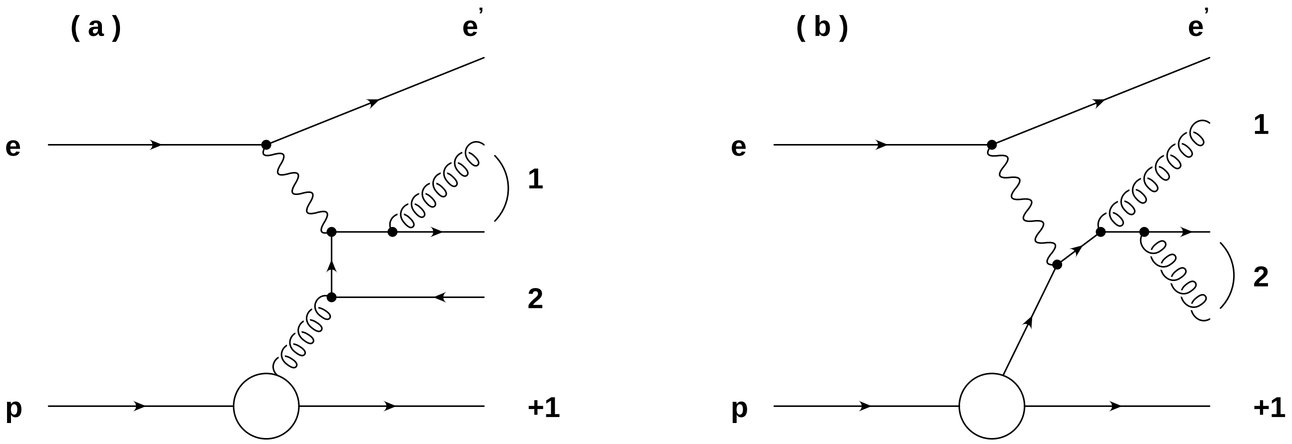

Figure 3.6: *Some generic second order Feynman diagrams of ep scattering. These are (3+1) parton final states. If due to resolution two partons are not resolved as indicated by the small bend this will lead to a (2+1) jet event (cf. section 5.1).*

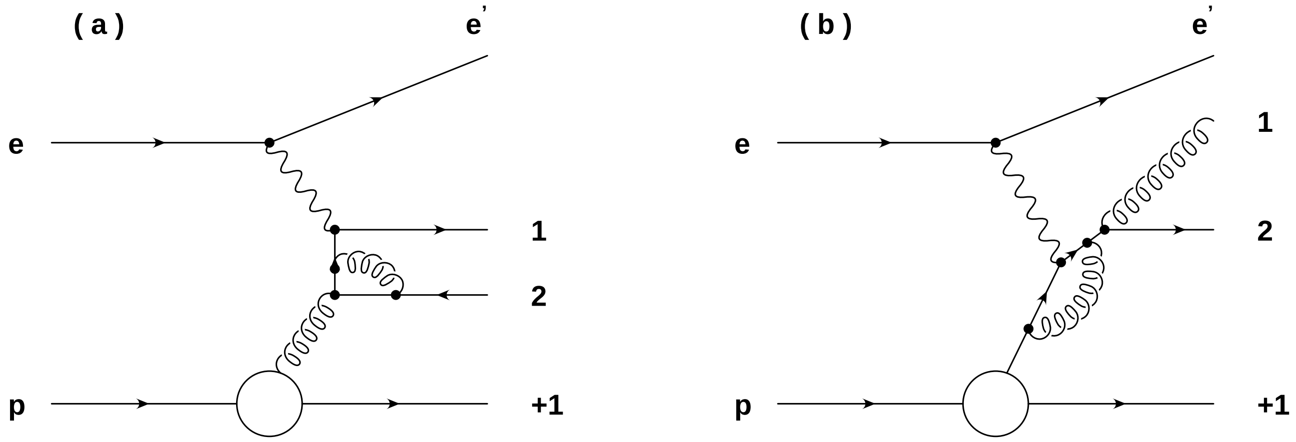

Figure 3.7: *Virtual corrections to the (2+1) parton final state in ep scattering.*
(a) A NLO correction $\mathcal{O}(\alpha_s^3)$ to the BGF graph.
(b) A NLO correction $\mathcal{O}(\alpha_s^3)$ to the QCDC graph.

above), with probability functions, the PDF's, for finding the incoming partons in a given particle, schematically

$$\sigma = \sum \int d\xi \cdot PDF \cdot \hat{\sigma} \tag{3.14}$$

In the QPM for purely electromagnetic electron proton scattering this can be written as

$$\sigma_{ep} = \sum_i \int d\xi \cdot \Phi_{i/p}(\xi) \cdot \hat{\sigma}_{eq \to e'q'} \tag{3.15}$$

$\hat{\sigma}_{eq \to e'q'}$ is the matrix element and $\Phi_{i/p}(\xi)$, where i denotes the quark flavour ($i = u,\ d$), gives the probability to find a quark of type i in the proton which carries a momentum fraction ξ of the proton namely $p_{q_i} = \xi P$.

The important fact of this concept is that the PDF's are universal, in the sense that they do not depend on the process under consideration. The PDF's of the proton are the same for example for $p\bar{p}$ scattering and ep scattering.

Now the changes introduced by QCD are inspected. The major change is that the PDF's no longer are only functions of ξ but also depend on the renormalization scale μ^2 (cf. section 2.1) and the factorization scale μ_f^2.

$$\Phi_{i/p}(\xi) \to \Phi_{i/p}(\xi, \mu^2, \mu_f^2) \tag{3.16}$$

The factorization scale is the typical scale to divide between the partonic cross section and the PDF. In other words this scale serves to define the separation between the short range hard interaction (μ_f^2 large) and the long range soft interaction (μ_f^2 small) in terms of a definite description, the factorization scheme (cf. chapter 3 in [16]). This makes both the partonic cross sections and the PDF's scheme dependent.

The first term introduced by QCD is to $\mathcal{O}(\alpha_s)$ meaning that one can also pick up gluons radiated by quarks in the proton, or sea quarks produced by $g \to q\bar{q}$. Consequently PDF's for valence quarks, sea quarks and gluons $i = (u,\ \bar{u},\ d,\ \bar{d},\ s,\ \bar{s},\ c,\ \bar{c},\ b,\ \bar{b},\ t,\ \bar{t}\,, g)$ are needed.

QCD predicts the probabilities for the branchings $g \to q\bar{q}$, $q \to qg$ and $g \to gg$ in terms of the Altarelli Parisi splitting functions. The leading order expressions are the following.

$$\begin{aligned} P_{g\to q\bar{q}}(z) &= \frac{1}{2}\cdot\left(z^2+(1-z)^2\right) \\ P_{q\to qg}(z) &= \frac{4}{3}\cdot\frac{1+(1-z)^2}{z} \\ P_{g\to gg}(z) &= 6\cdot\left(\frac{1-z}{z}+\frac{z}{1-z}+z(1-z)\right) \end{aligned} \tag{3.17}$$

For example $g \to q\bar{q}$ means a gluon of momentum ξ' splits in a quark of momentum ξ with $\xi = z\xi'$ and an antiquark of momentum $(1-z)\xi'$. Thus the evolution of the PDF's, with respect to μ_f, are known in the framework of the Altarelli Parisi evolution equation.

$$\mu_f \frac{d\Phi_{i/p}(\xi,\mu^2,\mu_f^2)}{d\mu_f} = \sum_{j=q,\bar{q},g} \frac{\alpha_s(\mu^2)}{2\pi}\int_\xi^1 \frac{d\xi'}{\xi'} P_{ij}(\frac{\xi}{\xi'})\cdot\Phi_{j/p}(\xi',\mu^2,\mu_f^2) \tag{3.18}$$

An interesting fact is that the lower bound of the integral is ξ. To evaluate PDF's at a scale μ_f^2 one only needs to know the PDF's for $\xi' > \xi$ at some scale $\mu_{0,f}^2$. The only unknown left is the set of PDF's at a given starting point $\mu_{0,f}^2$. Everything else is predicted by this integro differential equation.

On the other hand QCD does not contain a prediction of the evolution of PDF's with ξ. The ξ dependence has to be parametrized and fitted to data [5].

At this point one has to choose the factorization scheme in which the calculation is performed. Commonly used are the modified minimal subtraction scheme and the deep inelastic scheme, abbreviated by $\overline{MS}$ and DIS scheme. They differ in the way the structure function F_2 of deep inelastic scattering is defined, but they are related (cf. chapter 5 in [16]). A given PDF in the $\overline{MS}$ scheme can be unambiguously converted to a PDF in the DIS scheme and vice versa. In the DIS scheme the coefficient functions, which have to be convoluted with the PDF's to evaluate the structure functions F_i, are defined to be proportional to delta functions to all orders in perturbation theory. Correspondingly all corrections are put into the quark and antiquark distributions.

There exist various sets of PDF's collected in libraries. The most popular libraries are the PDFLIB [17] and the PAKPDF [18]. The PDF's were obtained by fits to the existing data. To fit the data a program is needed which contains the integro differential equations, the cross sections for the measured processes to a given order in α_s and a formula to calculate α_s, everything consistent in one scheme (cf. chapter 8 in [16]). A parametrization as a function of ξ is chosen and by iteration the PDF's together with α_s are determined. Depending on the choices taken one gets a leading order (LO) or next to leading order (NLO) PDF in the DIS or $\overline{MS}$ scheme. Schematically the PDF's in NLO have the general form.

$$\Phi_{i/p}(\xi,\mu^2,\mu_f^2) = \Phi_{i/p}^{\circ}(\xi,\mu^2,\mu_f^2) + \alpha_s\Phi_{i/p}^1(\xi,\mu^2,\mu_f^2) \tag{3.19}$$

Figure 3.8 shows the quark distribution (the valence quark and sea quark contributions are added) and the gluon distribution for two values of μ_f^2 for the PDF sets $MRSD^{\circ}$ and $MRSD^{-}$ as function of ξ. In addition the ratio of both is shown in the range where $\xi\cdot\Phi_{i/p}(\xi) > 1\%$. For $\xi > 10^{-2}$ where data exist, they agree, but the extrapolation in the low ξ region is based on

[5] For example the CTEQ collaboration uses as input parametrization $\Phi_{i/p}(\xi,\mu_{0,f}^2) = A_{0,i}\cdot\xi^{A_{1,i}}\cdot(1-\xi)^{A_{2,i}}\cdot(1+A_{3,i}\xi^{A_{4,i}})$ at $\mu_{0,f}^2 = 4\ GeV^2$, i=(u, d, g, $\bar{u}$, $\bar{d}$, s).

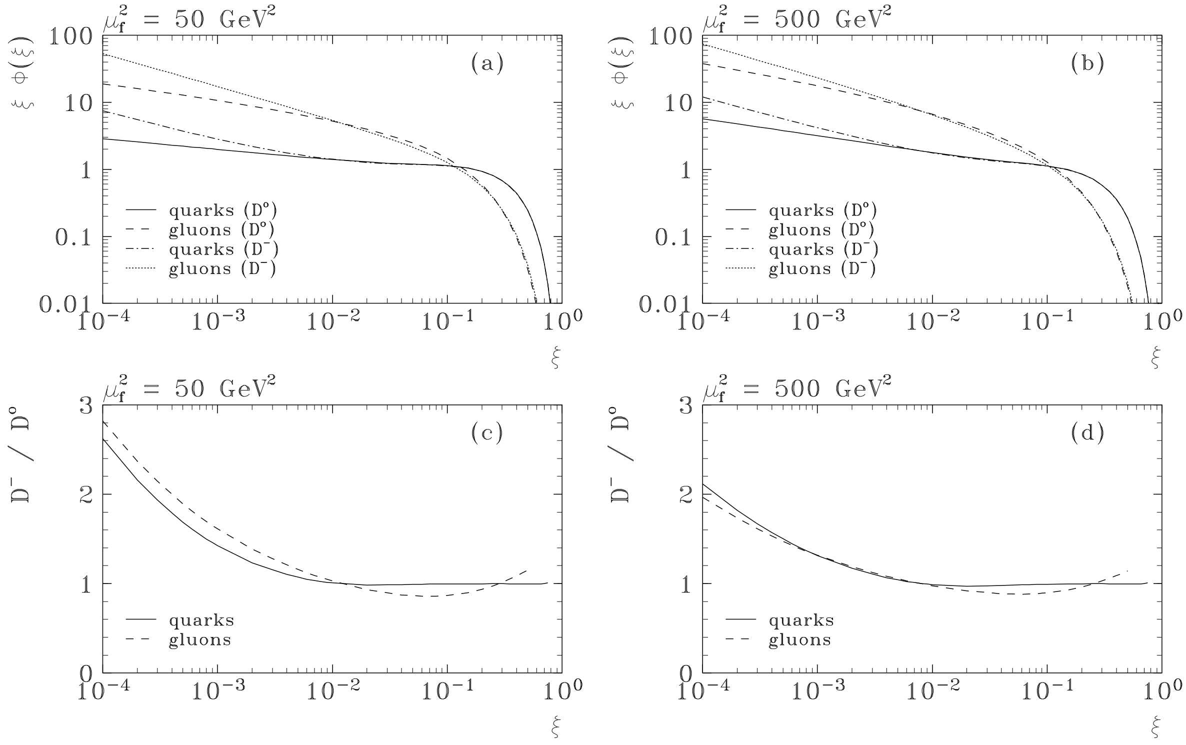

Figure 3.8: *The PDF's MRSD° and MRSD$^-$ for two values of μ_f^2, $\mu_f^2 = 50\ GeV^2$ (a) and $\mu_f^2 = 500\ GeV^2$ (b). Shown are the quark and gluon distributions in the upper plots, the ratios can be found in the lower ones (c, d). For discussion see text.*

assumptions and is chosen to be different for the two sets. This region will be covered by HERA for the first time, and the measurement of the structure function F_2 [19] will constrain the PDF's further. At the moment this difference shows the magnitude of the expected uncertainty one has to deal with. For low μ_f^2 and low ξ ($\xi < 10^{-3}$) the difference is biggest and reaches factors of 2-3 as seen from figure 3.8 (c). In this work both PDF's, *MRSD°* and *MRSD$^-$* will be used in parallel depending on the availability of fully simulated and reconstructed Monte Carlo events.

In order to use the PDF's properly some clarification of terminology is necessary.

- LO cross sections are calculated to the lowest occuring power of α_s
  e.g. $\sigma_{LO}(ep \rightarrow e'X) = \mathcal{O}(\alpha_s^o)$, $\sigma_{LO}(ep \rightarrow (2+1) - jets) = \mathcal{O}(\alpha_s)$

- NLO means terms in the next to leading power of α_s are taken into account as well
  e.g. $\sigma_{NLO}(ep \rightarrow e'X) = \mathcal{O}(\alpha_s)$, $\sigma_{NLO}(ep \rightarrow (2+1) - jets) = \mathcal{O}(\alpha_s^2)$

- The 1-loop and 2-loop formula, equations 2.4 and 2.5 are the LO and NLO expressions for α_s

Consequently a LO PDF is evaluated by using LO cross sections, the LO Altarelli Parisi evolution equation and the LO expression for α_s. The given Λ value of that fit is defined with respect to the 1-loop expression. To evaluate a NLO PDF, NLO cross sections, the NLO Altarelli Parisi evolution equation and the 2-loop formula for α_s are used, giving the corresponding Λ value.

In turn to convolute a PDF with cross sections calculated in a given scheme in LO/NLO one is forced to use the LO/NLO PDF's in the same scheme, otherwise the results are of limited use (cf. chapter 8 in [16]). In these calculations usually a simplification is made by taking $\mu^2 = \mu_f^2 = Q^2$ which leads to:

$$\Phi_{i/p}(\xi, \mu^2, \mu_f^2) = \Phi_{i/p}(\xi, Q^2) \tag{3.20}$$

The impact of the simplification for this analysis will be studied in section 11.5.3. Consistent calculations of jet cross sections in DIS can be found in section 5.1

Chapter 4

Jets and jet Algorithms

What is a jet? Naively speaking a jet is a bunch of collimated particles. A more elaborate answer would be that a jet is a concept which addresses two problems:

1. The relation between observed hadrons and primary partons
2. The singularities in cross section calculations

In order to make this more clear the evolution of an ep scattering event is given in figure 4.1.

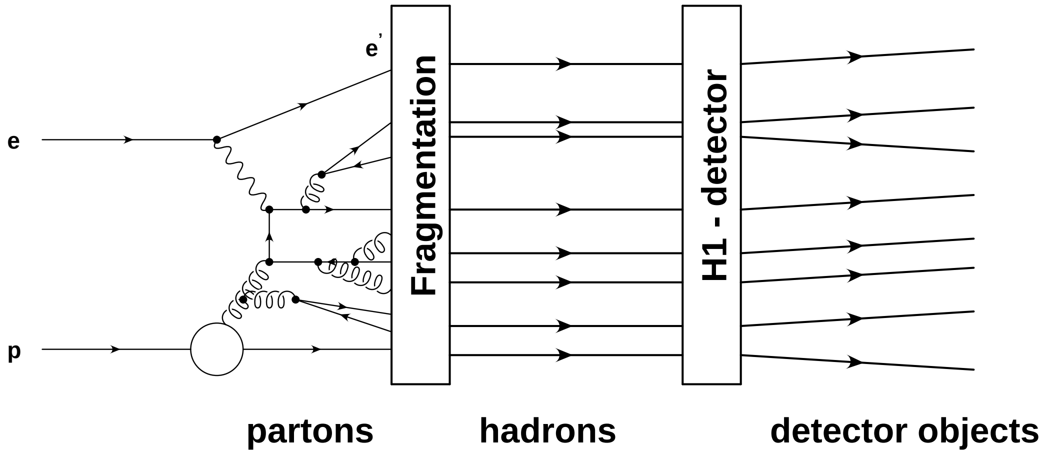

Figure 4.1: *Event evolution sketch. For explanations see text.*

Consider, for example, a BGF event, the two outgoing quarks are offshell, $p_q^2 \neq 0$, and radiate gluons, which in turn can create $q\bar{q}$ pairs, thereby loosing part of their offshellness/virtuality. In addition there exists a parton cascade in the initial state. If $p_q^2 \approx \Lambda^2$, the partonic state will recombine into hadrons, this is called hadronization or fragmentation. The outgoing hadrons will manifest themselves as energy deposits in a detector.

The problem is how to recombine the hadrons, or the detector objects, in order to get the best estimate of the four vectors of the original quarks. This is needed to test QCD predictions, which are available only on the parton level. It is done by a jet definition, implemented in a jet algorithm, which needs prescriptions to take the following decisions.

1. Which hadrons to combine next

2. How to combine the hadron 4-vectors
3. When to stop the procedure

Stopping the procedure at a chosen cutoff value means defining the resolution power of the algorithm, so defining how 'close' the quarks may be, to be still resolved at a particular cutoff. This means a 2+1 parton state (cf. figure 3.4) may result in a (N+1) jet state ($N = 0, 1, ..., N_{hadrons} - 1$), depending on the chosen cutoff value. If the cutoff approaches zero one enters the phase space region where the cross section diverges (cf. section 5.1). Choosing a minimum cutoff value avoids the divergencies in the cross section.

There exist various algorithms, the most popular and frequently used are described below.

4.1 Cone Algorithm

The cone algorithm was developed for the analysis of $p\bar{p}$ collider data. This method is based on the summation of energy in a $(\delta\eta, \delta\varphi)$ grid of pseudorapidity (η), defined as $\eta \equiv -\log(\tan(\vartheta/2))$, and azimuthal angle ($\varphi$), starting from a prominent energy deposit and summing up to a distance of $R = \sqrt{\delta\eta^2 + \delta\varphi^2}$ around it.

One has to make four choices, the definition of objects to be clustered, the minimum energy or transverse energy which is required for a prominent energy deposit, the value of the radius R and the minimum transverse energy for an summed object to be considered as a jet.

An effort was made to standardize this choices which lead to the snow mass accord [20]. The proposed value for R is $R = 0.7$. The values of the used energy scales are not standardized, they are chosen differently depending on the reaction under study.

4.2 Cluster Algorithms

4.2.1 The JADE Algorithm and the pseudo particle concept

The JADE-algorithm was introduced by the JADE Collaboration [21] to measure jets in e^+e^- annihilations. The measure y_{ij} is the invariant mass squared between two objects m_{ij}^2 scaled with a typical energy scale of the process.

$$y_{ij} = \frac{m_{ij}^2}{scale^2} \tag{4.1}$$

In e^+e^- collisions where only one scale is involved, the center of mass energy $E_{CM}^2 = Q^2$ is the natural choice and this is experimentally approximated by the visible energy E_{vis}^2. The appropriate choice for ep scattering will be discussed in section 5.1.

There exist various possibilities to define m_{ij}^2 and how to combine the two objects (i, j) into a new one k. The various possibilities, called recombination schemes, are listed in table 4.1 and the impact of the various choices on a jet analysis is discussed in section 10.4.2. In principle the algorithm works as follows (cf. figure 4.2). First one has to define a number of objects which should be clustered, then the following algorithm is performed.

1. All pairs of m_{ij}^2 are calculated.
2. If the smallest m_{ij}^2 value is smaller than $y_c \cdot scale^2$ the pair (i, j) is combined to form an object k, according to the chosen recombination scheme. Here, y_c is the free parameter which can be chosen to get a desired separation in m_{ij}^2.

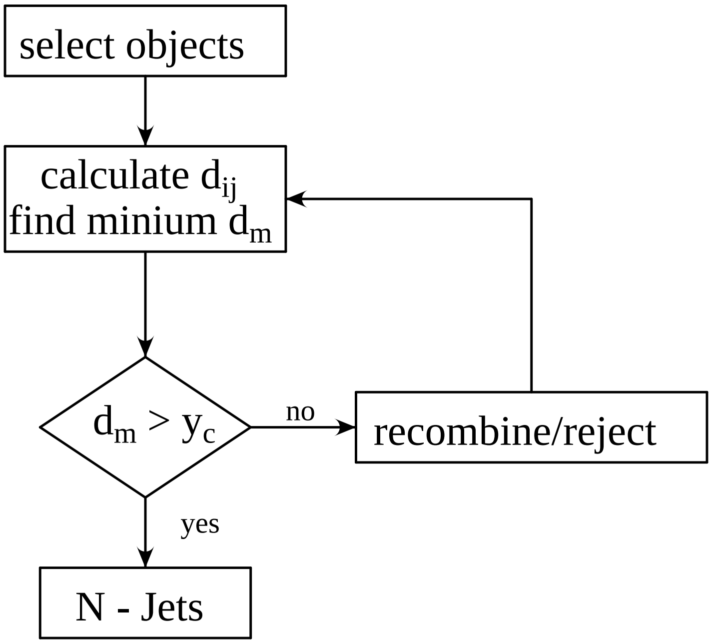

Figure 4.2: *The flow diagram of jet algorithms, sketching the common strategy of a clustering algorithm to derive the number of jets observed in a reaction.*

3. The objects i and j are removed, k is included and one starts over from step 1.

This procedure is continued until all the possible pairs of m_{ij}^2 are greater than $y_c \cdot scale^2$. The number of remaining objects is the number of jets defined by this algorithm at y_c. The JADE algorithm has been used with great success in e^+e^- annihilations.

There are several complications in *ep* scattering compared to the situation at e^+e^- colliders where the center of mass system and the laboratory system coincide.

- The hadrons are strongly boosted to the direction of the incoming proton. Therefore most of the fragmentation products of the proton remnant will not be observed in the acceptance region of a detector.

- Because the struck parton carries colour charge the remnant is coloured and via charge forces it is connected to the partons of the hard subprocess. This results in gluon radiation between the remnant and the connected partons giving an additional energy flow between the hard subsystem and the remnant which at least partly belongs to the remnant.

- In the jet cross section calculation (cf. section 5.1) it is also checked whether an outgoing parton can be resolved from the proton remnant and this influences the jet classification in the classes (2+1)-jet or (1+1)-jet. Consequently the remnant has to be taken into account in the jet algorithm.

A jet algorithm for *ep* scattering has to correctly deal with all these effects. This leads to the concept of introducing a so called pseudo-particle which accounts for the proton remnant. The pseudo particle represents the best estimate of the unseen proton remnant one can get from the observed part of the event. This concept was suggested by D. Graudenz and first experimentally used in a jet analysis on photoproduction events in H1 at HERA [22].

The effect of this concept for DIS events was first studied in [23], the details can be found in section 10.3.1.

scheme	m_{ij}^2	recombination	remarks
JADE	$2E_iE_j(1-\cos\theta_{ij})$	$p_k = p_i + p_j$	m_{ij}^2 neglects individual masses
E	$(p_i+p_j)^2$	$p_k = p_i + p_j$	Lorentz invariant
E0	$(p_i+p_j)^2$	$E_k = (E_i + E_j)$ $\vec{p_k} = \frac{E_k}{\lvert\vec{p_i}+\vec{p_j}\rvert}\cdot(\vec{p_i}+\vec{p_j})$	$\vec{p}$ not conserved
P	$(p_i+p_j)^2$	$\vec{p_k} = \vec{p_i}+\vec{p_j}, E_k = \lvert\vec{p_k}\rvert$	E not conserved
P0	$(p_i+p_j)^2$	$\vec{p_k} = \vec{p_i}+\vec{p_j}, E_k = \lvert\vec{p_k}\rvert$	same as P but scale updated after each recombination

Table 4.1: *Recombination schemes of the JADE algorithm.*

4.2.2 The k_t Algorithm

Another type of cluster algorithm, the k_t algorithm, is based on a relative p_t measure. It was introduced during a QCD workshop in Durham and is therefore often called Durham algorithm as well.

Recently there was an attempt to standardize jet counting in the framework of the k_t algorithm for e^+e^- , $p\bar{p}$, ep , γp reactions [24], which led to a modification of the k_t algorithm by introducing a concept to account for the various remnants involved [1]. The algorithm is now essentially a two step procedure. The first step tries to separate the hard process from the remnant and the second tries to resolve the jet structure of the hard interaction. In this procedure the Breit frame is the prefered Lorentz frame by theoretical arguments [25].

For DIS the procedure is as follows. Two distance measures are introduced, y_{kp} and y_{kl}, which are scaled by a parameter called E_t, fulfilling the requirement $Q^2 \leq E_t^2 \leq \Lambda^2$. Here E_t is an arbitrary scale, note, it is not the total transverse energy of the event with respect to the beam direction. The indices k, l denote the objects to be clustered and p stands for the incoming proton vector.

$$
\begin{aligned}
y_{kp} &= \frac{2(1-\cos\theta_{kp})}{E_t^2}\cdot E_k^2 \\
y_{kl} &= \frac{2(1-\cos\theta_{kl})}{E_t^2}\cdot min(E_k^2, E_l^2)
\end{aligned}
\tag{4.2}
$$

[1]In photoproduction (γp scattering at $Q^2 \approx 0$), also a photon remnant exists, if the photon is resolved and if a hadronic content of the photon, either a quark or a gluon, enters the hard interaction.

The choice of the minimum value of E_k^2 and E_l^2 in y_{kl} ensures that the algorithm 'factorizes' in the sense described in 5.2. After choosing the objects to be clustered the following procedure is performed.

1. Calculate all y_{kl} and y_{kp}.

2. If the minimum of all y_{kl} and y_{kp} is smaller than unity, clustering takes place. In the case where one of the y_{kl} is the smallest, k and l are combined to form m using $p_m = p_k + p_l$. Then k, l are removed and m is included instead. If one of the y_{kp} is the smallest, one simply removes k.

3. Now one starts over from step 1. until all y_{kl} and y_{kp} exceed unity.

The result after this first step is a 'beam jet' and a number of objects called 'macro jets'. The name k_t algorithm originates from the fact that if two objects are close in angle to each other, one can perform a Taylor expansion of the cos term [2] getting $y_{kp} = \frac{k_{tk}^2}{E_t^2}$ and $y_{kl} = \frac{min(k_{tk}^2, k_{tl}^2)}{E_t^2}$. Then the distance measure is simply the minimum scaled transverse momentum squared of two objects. In principle, what the algorithm does, is absorbing everything which has a k_t^2 smaller then E_t^2 in the remnant, unless it is closer to another object. Given this, one chooses $y_{\rm c} = \frac{Q_o^2}{E_t^2} \leq 1$ and tries to resolve the macro jets using the following procedure.

1. Calculate all y_{kl}.

2. If the minimum of all y_{kl} is smaller than $y_{\rm c}$, combine k, l to form m as before, remove k, l and include m.

3. Start over from step 1 until all y_{kl} are bigger than $y_{\rm c}$.

The final objects have the property that the relative transverse momentum between any two objects is bounded by $y_{\rm c}$, $\Delta k_t \geq \sqrt{y_{\rm c}} \cdot E_t$. They are the jets defined by this algorithm at a fixed but free $y_{\rm c}$. In contrast to the JADE algorithm the remnant is not clustered and consequently jet counting is done by suppressing the (+1) in the number of jets.

Varying E_t^2 means steering the required k_t resolution from the remnant and influencing the number of jets at a fixed $y_{\rm c}$ value. If E_t^2 is bigger than the total transverse energy squared of the event one ends up with zero jets.

The theoretical motivations of this concept can be found in section 5.2 and the application for the H1 experiment is discussed in section 10.5

[2] $2(1 - \cos\theta) = \sin^2\theta$ and the transverse momentum is $k_{tk} = E_k \sin\theta_k$.

Chapter 5

Status of jet-cross section calculations in DIS

5.1 Second Order calculations

The jet cross section are calculated for (1+1)-jets to $\mathcal{O}(\alpha_s)$ [26, 27, 28], and for (2+1)-jets to $\mathcal{O}(\alpha_s^2)$ [29, 30]. In this analysis the calculations of D. Graudenz [29] are used. The cross sections can be written in terms of the cross sections to a definite helicity state of the virtual photon. There exist different ways to decompose these contributions, which result in some confusion [1]. One limitation in the calculation of [29] is given by the fact that in the (2+1)-jet cross section to $\mathcal{O}(\alpha_s^2)$ only σ_g is calculated [2], which means that the longitudinal part of the term proportional to α_s^2 is only partly taken into account, however, the numerical importance of this is expected to be small (cf. figure 5.1). Further details of the calculation are treated in [29]. In the following only the major ingredients required for comparing to experimental data are discussed.

In order to derive jet cross sections one has to calculate the Feynman diagrams discussed in section 3.2 and map them to (N+1)-jet final states by carefully treating the divergencies. To be more specific, for the (N+1)-jet cross section to $\mathcal{O}(\alpha_s^N)$ one has to calculate the leading contribution, or the Born term $\mathcal{O}(\alpha_s^{N-1})$ and the next to leading contributions. These are the virtual corrections, which means graphs of type figure 3.5 (a) to $\mathcal{O}(\alpha_s^N)$ and the Born term $\mathcal{O}(\alpha_s^N)$ in that physical region where it appears as an (N+1)-jet event (cf. figure 3.6).

In this calculation two types of singularities occur if an internal line is onshell (the parton is massless). For example, if a quark q radiates a gluon $q \to q'g$, it is onshell if either the gluon is soft $E_g \approx 0$ (infrared divergence), or collinear $\cos\theta_{q'g} \approx 1$ (collinear divergence) as can be seen from $m_q^2 = m_{q'g}^2 = 2E_g E_{q'}(1-\cos\theta_{q'g})$. The same argument holds for gluon splitting $g \to q\bar{q}$ and gluon loops $q \to q'g \to q$ because only four vector arithmetics is used.

The divergencies of the virtual and real corrections cancel, for the initial state divergencies collinear to the incoming proton, this does not hold and the solution to this is to renormalize the parton density functions. This procedure makes the calculation renormalization scheme dependent (cf. section 3.3). The calculations in [29] are done in the minimal subtraction scheme $\overline{MS}$, using the technique of dimensional regularization in $d = 4 - 2\epsilon$ dimensions. This

[1] The terminology concerning the terminus 'transversal' in [29] differ from that used for instance in [30]. The relations are $\sigma_g = 2(1-\epsilon)\sigma_U - \sigma_L$ which is denoted as 'transversal' in [29] and $\sigma_0 = \sigma_L$. Here U stands for unpolarized or transversal polarized photons and L for longitudinal polarized in the convention of [30].

[2] σ_g is the result of the trace of the hadron tensor, defined as the contraction of the hadron tensor $H^{\mu\nu}$ with the metric tensor $g_{\mu\nu}$, $TR(H^{\mu\nu}) = g_{\mu\nu} \cdot H^{\mu\nu}$.

introduces the scales μ^2 and μ_f^2 in the calculation and gives rise to terms of the form $\log \frac{\mu^2}{Q^2}$ and $\log \frac{\mu_f^2}{Q^2}$ in the cross section.

The outcome of matrix element calculations are (N'+ 1) partonic final states which have to be mapped to a (N + 1) jet final state with $N' \geq N$. To get a classification in (1+1)-jet and (2+1)-jet events one has to define a borderline in phase space between both, which is equivalent to introducing a jet resolution parameter. To account for both singularities (see above) m_{ij}^2 is chosen and scaled by W^2 in order to get a dimensionless parameter, the well known y_c, defined as

$$y_{\mathrm{c}} = \frac{m_{ij}^2}{W^2} \tag{5.1}$$

where W^2 is the invariant mass of all partons squared and the indices $(i,\ j)$ run over all partons including the remnant.

If one includes the remnant in the clustering W^2 is the appropriate scale, which is equivalent to the choice of E_{vis}^2 for jet reconstruction in $\mathrm{e}^+\mathrm{e}^-$ reactions. The (1+1)-jet cross section is a five fold differential and the (2+1)-jet cross section an eightfold. This and the fact that integration over ξ requires integration over the PDF's, which are only available in a tabularized form (cf. section 3.2), makes it necessary to use numerical integration methods to evaluate cross sections. The corresponding Monte Carlo program PROJET will be discussed next.

5.1.1 The cross section Monte Carlo PROJET

PROJET [31] is a program which calculates jet cross sections in deep inelastic scattering with the help of the numerical integration procedure VEGAS. It is based on perturbative QCD predictions to $\mathcal{O}(\alpha_s^2)$ by D. Graudenz and describes jet final states with up to four partons. [3] The four vectors of the incoming and outgoing partons including the electron and the virtual photon can be accessed via an event record.

The program integrates the (N+1)-jet cross sections (N = 1, 2, 3) in LO and the (N+1)-jet cross section (N = 1, 2) in NLO, each for different helicity states of the virtual photon. The running of α_s is implemented in LO and NLO. The running of α_{em} is simulated also. In order to compare different PDF's PROJET can be linked to the PAKPDF library. The explicit dependence on μ_f^2 and μ^2 is kept in the formulas and changes in the cross sections, due to changes in the scales, can be inspected (cf. section 11.5.3).

The event selection of an experiment is simply a restriction in phase space. In this analysis this will be done in terms of Lorentz invariant variables (Q_e^2, y_e, W^2) and quantities measured in the H1 laboratory system (ϑ_e, E_e, ϑ_{jet}), or in the center of mass system $p_{t,jet}^\star$ [4]. In order to have full flexibility the same phase space restrictions can be chosen while integrating cross sections with PROJET. The adaptation of PROJET to the needs of an experiment was done together with the author as part of this work. With this feature the jet rates measured in an experiment and corrected for detector effects, can be compared directly to integrated cross sections.

As an example of the flexibility in cross section calculations with PROJET figure 5.1 shows the various contributions to the jet cross sections for two phase space regions. The terms LO, NLO in this figure refer to the parts of the matrix elements taken into account, always using the NLO PDF *MRSD°* and the 2-loop α_s formula for $\Lambda_{4,\overline{MS}} = 0.215\ MeV$. This shows how the

[3] Especially no fragmentation is done and PROJET cannot be used as an event generator (cf. section 7).

[4] All quantities measured in the center of mass system will be denoted by a ($\star$).

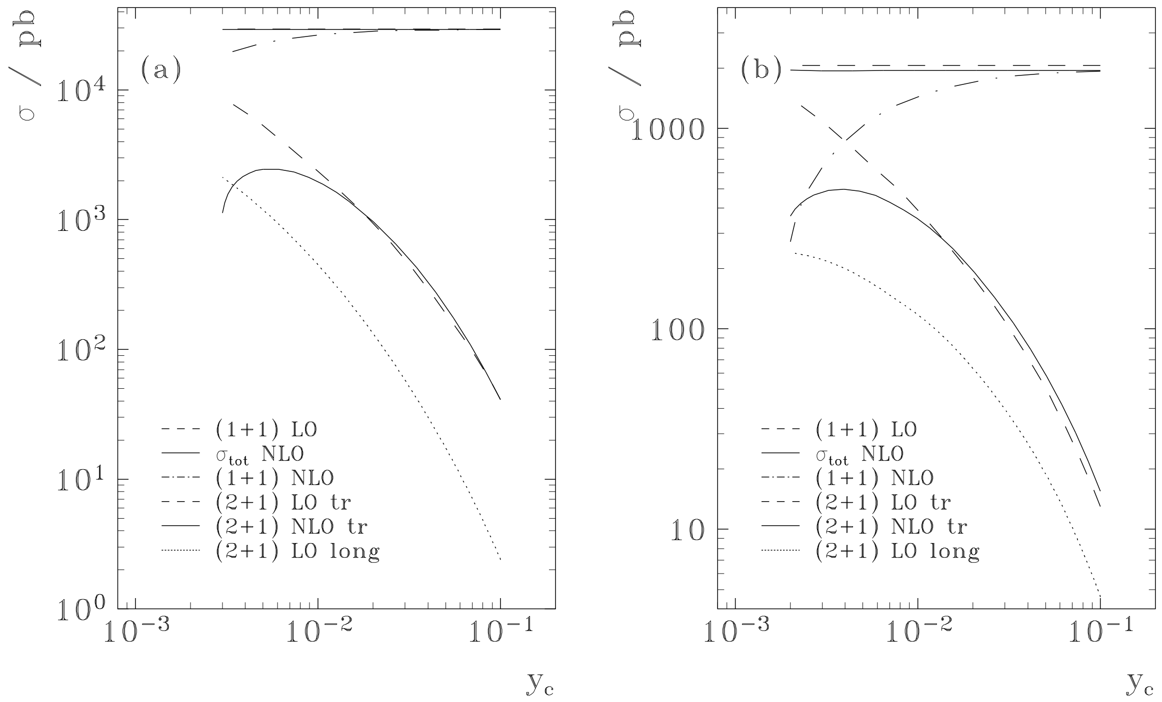

Figure 5.1: *Different contributions to the jet cross sections for $W^2 > 5000$ GeV^2. The legend denotes the curves from top to bottom, (tr) stands for transversal and (long) for longitudinal. To take into account acceptance restrictions of the H1 detector (cf. section 9.1) the electron kinematic variables are constrained further.*

(a) $10 < Q^2 < 100$ *GeV*^{2}, $160° < \vartheta_e < 172.5°$ *and* $E_e > 14$ *GeV.*
(1+1) LO and σ_{tot} NLO are indistinguishable due to the logarithmic scale.

(b) $100 < Q^2 < 4000$ *GeV*^{2}, $10° < \vartheta_e < 148°$ *and* $y_e < 0.7$.

different matrix elements are composed in a NLO cross section, it does not show the difference of consistent jet cross section calculations in ep scattering, this question will be addressed in section 5.1.2. Several observations can be made.

- The NLO coefficient to the total cross section is negative and the relative change is different for the two phase space regions. It is almost invisible in (a) due to the logarithmic scale and it depends on W^2.

- The lower the y_c value is the higher is the resolution power and more events are classified as (2+1)-jet events. At $y_c \approx 0.004$ the (1+1)-jet and (2+1)-jet cross section to $\mathcal{O}(\alpha_s)$ are of equal size in region (b), whereas in (a) this occurs at a lower y_c value outside the shown range.

- The NLO correction to the transversal part of the (2+1)-jet cross section changes sign at $y_c \approx 0.015$. Above it is positive, whereas below it is negative and approaches $-\infty$ for

$y_c \to 0$. The cross over point, as well as the numerical value of this correction, is different in both phase space regions showing that there exists no simple 'k-factor' to account for the NLO terms.

- In LO the longitudinal part of the (2+1)-jet cross section ranges from $6-18\,\%$ in region (a) and from $17-26\,\%$ in region (b). The longitudinal part to the NLO coefficient of the (2+1)-jet cross section is missing (cf. section 5.1). If one assumes that the relative amount in NLO is as large as in the LO terms and restricts the analysis to the y_c range around 0.02 where the NLO correction to the transversal part is in the order of $20\,\%$, then the missing part is expected to account for $2-4\,\%$ of the total (2+1)-jet cross section.

- As indicated by the fast drop of the NLO part of the (2+1)-jet cross section at low y_c integration will become instable and the results unreliable if one chooses y_c in the low y_c range.

5.1.2 The importance of NLO cross sections

In section 3.3 the consistent prescription of LO and NLO jet cross sections is outlined. Now the numerical importance in ep scattering is evaluated.

In comparing LO to NLO in various processes often two effects cancel each other. The NLO coefficient of α_s is negative, α_s decreases from LO to NLO, this may be compensated by taking into account the NLO term in the perturbative series of the observable. Due to this cancellation often the numerical difference between LO and NLO is small. In DIS, because of the structure of the proton, the PDF's enter as a third component.

PDF		Bin 1	Bin 2	Bin 3	Bin 4	Bin 5
GRV(LO)	σ_{tot} [pb]	15138	9813.9	8608.6	1445.0	584.2
	σ_{2+1} [pb]	204.9	173.3	243.4	92.8	70.1
	R [%]	1.4	1.8	2.8	6.4	12.0
GRV(NLO)	σ_{tot} [pb]	17847	11007	9220.6	1444.7	590.4
	σ_{2+1} [pb]	152.8	140.2	202.7	84.0	66.2
	R [%]	0.9	1.3	2.2	5.8	11.2

Table 5.1: *PROJET comparison of LO versus NLO cross sections. Used are the GRV parton densities in LO/NLO, the corresponding matrix elements in LO/NLO and the LO/NLO formula of α_s for the $\Lambda^2_{4,\overline{MS}}$ values quoted together with the PDF's. The jet cut is $y_c = 0.02$. The Bins in Q^2 are defined in table 9.2.*

This is studied with the GRV parton density, which is available in LO and NLO, by using the corresponding Matrix elements of PROJET and the $\Lambda_{4,\overline{MS}}$ values which are quoted by the authors together with the PDF. Table 5.1 contains the cross sections in the five Bins in Q^2 and for $y_c = 0.02$, within the phase space cuts of the analysis which will be discussed in section 9.1. For the (2+1)-jet events the ϑ_{jet} and $p^\star_{t,jet}$ cut (cf. section 10.2) are applied. The numerical importance concerning the jet rate measurement is demonstrated in figure 5.2 obtained from table 5.1. The total cross section and the (2+1)-jets cross section change in different directions at this particular y_c value (b). The total cross section increases from LO to NLO whereas the (2+1)-jets cross section decreases, leading to a $6 - 37\,\%$ change on the rate (c), while being more important at lower Q^2 values. Besides the fact that α_s is only well defined in NLO, the difference of LO and NLO cross sections shows that the NLO correction is numerically important and has to be included in the QCD prediction to get a meaningful QCD prediction for the jet rates.

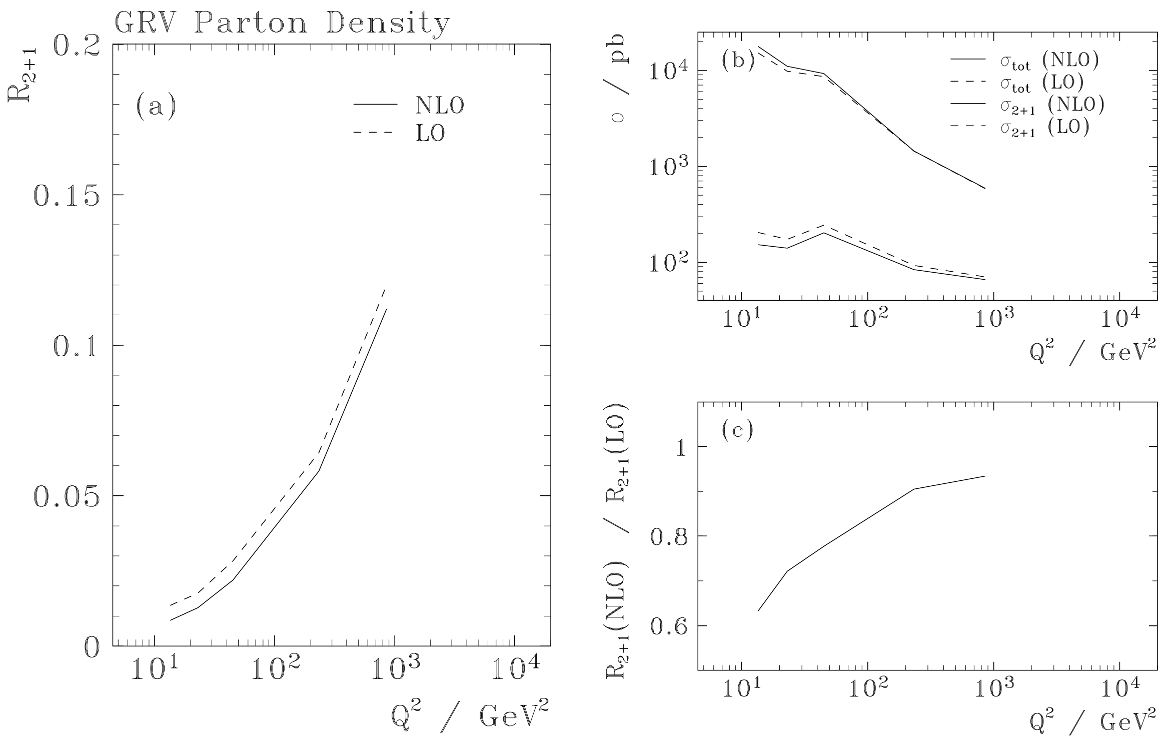

Figure 5.2: *The importance of NLO calculations. This plot is derived from the numbers given in table 5.1. The lines connect the values of the integrated cross sections which are plotted at the mean values of the bins. The cross section curves are not smooth due to the chosen binning.*
(a) The R_{2+1} jet rate as a function of $Q^2 = \mu^2$ at $y_c = 0.02$.
(b) The individual contributions in LO and NLO.
(c) The ratio R_{2+1} in NLO divided by the one in LO as function of $Q^2 = \mu^2$.

5.1.3 Contribution of quark and gluon initiated processes

Measuring the gluon PDF of the proton is of major interest because it is of great importance for cross section predictions for $p\bar{p}$ colliders, where gluon gluon scattering is an important process giving a considerable contribution to the event rate e.g. at the planned Large Hadron Collider (LHC). The information so far on the gluon density in the proton mainly comes from the Altarelli Parisi splitting function, while fitting the PDF.

The (2+1)-jet cross section is composed of q and g initiated processes. One can choose two approaches to evaluate the PDF for the gluons in the proton, either one needs to disentangle the two processes and measure the gluon initiated part separately, or one takes the whole (2+1)-jet cross section and subtracts the quark initiated part, with the knowledge of the measured quark PDF's. The latter approach has the advantage that no quark/gluon jet separation is needed. With this in mind the expected contribution of quark and gluon initiated processes for the same event selection and jet requirements as in table 5.1 are shown in table 5.2, assuming two different parton densities.

PDF	process	Bin 1	Bin 2	Bin 3	Bin 4	Bin 5
MRSD°	σ_{2+1} [pb]	145.8	138.7	204.4	89.7	69.7
	q initiated [pb]	28.6	28.9	50.2	33.0	40.5
	g initiated [pb]	117.2	109.8	154.2	56.7	29.2
MRSD⁻	σ_{2+1} [pb]	135.7	124.1	189.7	82.2	66.4
	q initiated [pb]	28.4	28.3	50.1	32.1	40.1
	g initiated [pb]	107.3	95.8	139.6	50.1	26.3
GRV	σ_{2+1} [pb]	152.8	140.2	202.7	84.0	66.2
	q initiated [pb]	27.0	27.0	48.6	30.9	38.8
	g initiated [pb]	125.8	113.2	154.1	53.1	27.4

Table 5.2: *Composition of of quark and gluon initiated processes in the five bins in Q^2 defined in table 9.2, for $y_c = 0.02$. The $p^{\star}_{t,jet}$ and the ϑ_{jet} cut (cf. section 10.2) are applied.*

At low Q^2 the gluon initiated processes are dominant, indicating that it would be preferable to carry out a measurement in this region. At a somewhat higher Q^2 the quark initiated processes are more important. The prediction of quark initiated processes however agree on a two percent level throughout, allowing to subtract this contribution from the total measured (2+1)-jet cross section. One expects around 50 events at the present Luminosity of $\mathcal{L}_{int} = 0.4\,pb^{-1}$ for Bins 1,2 and 3, suggesting that a measurement with 14 % statistical precision per bin can be reached in this domain. With this method for $y_c = 0.02$ one can measure the gluon parton density in the proton for $\xi > 10^{-2}$ as can be seen from equation 6.8. In this work the gluon density will not be derived, the analysis concentrates on the measurement of α_s, but it can certainly be done in this framework.

5.2 Factorization and resummed calculations

Factorization of cross sections in terms of matrix elements and PDF's is already discussed in section 3.3, now the 'factorization' of jet algorithms is addressed. Factorization in this context means that the jet algorithm separates between the remnant fragmentation and the hard subprocess.

As seen in e^+e^- annihilations one needs small x_μ values to fit α_s in NLO, indicating important higher order terms. However, it is a major task to compute the NNLO matrix elements. A partly solution to this is the resummation of leading logarithmic contributions to all orders in α_s and to match the resummed result to a NLO calculation. This adds the most important terms of all orders to the QCD prediction and thereby reduces the renormalization scale dependence.

In order to apply this technique a basic feature of the observable is required, the possibility of exponentiation. The exponentiation in turn needs the 'factorization'. For resummed calculations of jet cross section one needs 'factorization' for the matrix elements and for the used jet definition. In DIS this is achieved if both are only functions of $z = \xi/x$ and not of x alone. The conventionally JADE algorithm depends on W^2 and therefore on x alone, thereby violating this requirement. If one introduces Q^2 instead of W^2 as scale, as suggested in [25], one achieves the 'factorization' property for the JADE algorithm. The k_t algorithm also has this property, it was constructed inspired by this property and therefore allows for resummed calculations to be performed using this algorithm.

This type of 'factorization' is a basic ingredient of resummed calculations, not of QCD as such. An algorithm, like the JADE algorithm, which properly absorbs the initial state divergencies in the renormalized parton densities is well suited to derive perturbative QCD predictions.

Chapter 6

Strategies to measure α_s at HERA

The basic idea is to measure a quantity $Y(Q^2)$ experimentally which can be predicted by QCD as implemented in PROJET with only one free parameter $\alpha_s(Q^2, \Lambda^2)$. From the measured quantity and the PROJET expectation one derives α_s in bins of Q^2 namely $\alpha_s(Q_k^2)$ with k=1,...,n. This gives n measurements of α_s in one single experiment. By using the RGE of QCD, Λ can be fitted to these α_s measurements. Three different quantities of this type will be discussed below, followed by a short outline of the measurement which can be done via scaling violations in the structure functions.

6.1 The jet rate ratio $R_{2+1}(Q^2, y_c)$

$R_{2+1}(Q^2, y_c)$ is defined as the (2+1) jet cross section $\sigma_{2+1}(Q^2, \alpha_s, y_c)$ to $\mathcal{O}(\alpha_s^2)$ divided by the total cross section $\sigma_{tot}(Q^2, \alpha_s)$ to $\mathcal{O}(\alpha_s)$, which is independent of y_c. For simplicity, in this consideration, it is assumed that $\mu^2 = \mu_f^2 = Q^2$.

The first step is the selection of the region of phase space in terms of global event quantities. Then the jet criteria are defined [1], and the cross sections for (1+1)-jets and (2+1)-jets can be calculated, by integrating with PROJET, in the given Q^2 bins.

$$\begin{aligned}
d\sigma_{tot}(Q^2, \alpha_s) &= d\sigma_{1+1}(Q^2, \alpha_s, y_c) + d\sigma_{2+1}(Q^2, \alpha_s, y_c) + ... \\
d\sigma_{1+1}(Q^2, \alpha_s, y_c) &= d\sigma_{20}(Q^2, \alpha_s) + d\sigma_{21}(Q^2, \alpha_s, y_c) \\
d\sigma_{2+1}(Q^2, \alpha_s, y_c) &= d\sigma_{31}(Q^2, \alpha_s, y_c) + d\sigma_{32}(Q^2, \alpha_s, y_c)
\end{aligned}$$

Here $d\sigma_{ij}(Q^2, \alpha_s, y_c)$ is the (*(i-1) + 1*) jet cross section to $\mathcal{O}(\alpha_s^j)$ in a given bin in Q^2, for example, $d\sigma_{32}(Q^2, \alpha_s, y_c)$ is the (2+1) jet cross section to $\mathcal{O}(\alpha_s^2)$. If the bins are small so that the variation of $\alpha_s(Q^2)$ in the bin is small, it can be approximated by the mean value in the bin and the equations can be rewritten as.

$$\begin{aligned}
d\sigma_{1+1}(Q^2, \alpha_s, y_c) &= A_{20}(Q^2) + \alpha_s(Q^2, \Lambda^2) \cdot A_{21}(Q^2, y_c) \\
d\sigma_{2+1}(Q^2, \alpha_s, y_c) &= \alpha_s(Q^2, \Lambda^2) \cdot A_{31}(Q^2, y_c) + \alpha_s^2(Q^2, \Lambda^2) \cdot A_{32}(Q^2, y_c)
\end{aligned}$$

The $A_{ij}(Q^2, y_c)$ are defined analog to the $\sigma_{ij}(Q^2, \alpha_s, y_c)$ above. Dividing $d\sigma_{2+1}(Q^2, \alpha_s, y_c)$ by $d\sigma_{tot}(Q^2, \alpha_s)$ one gets the quantity R.

$$R_{2+1}(Q^2, y_c) = \frac{d\sigma_{2+1}(Q^2, \alpha_s, y_c)}{d\sigma_{tot}(Q^2, \alpha_s)}$$

[1] This may be, for example, acceptance regions in the laboratory system $\vartheta_{min} \leq \vartheta_{jet} \leq \vartheta_{max}$, or a minimum transverse momentum $p^\star_{t,jet}$ for the two hard jets in (2+1) jet events in the center of mass system. The actual cuts will be described in section 10.1.

$$= \frac{\alpha_s(Q^2,\Lambda^2)\cdot A_{31}(Q^2,y_c) + \alpha_s^2(Q^2,\Lambda^2)\cdot A_{32}(Q^2,y_c)}{A_{20}(Q^2) + \alpha_s(Q^2,\Lambda^2)\cdot\left[A_{21}(Q^2,y_c) + \tilde{A}_{31}(Q^2,y_c)\right]} \tag{6.1}$$

By introducing $\tilde{A}_{31}(Q^2,y_c)$ one accounts for the possibility to have additional jet requirements in $d\sigma_{2+1}(Q^2,\alpha_s,y_c)$ compared to $d\sigma_{tot}(Q^2,\alpha_s)$. For example, if one asks for a minimum $p^\star_{t,jet}$ in the (2+1)-jet events the event counts in $d\sigma_{tot}(Q^2,\alpha_s)$, even if it fails this cut for $d\sigma_{2+1}(Q^2,\alpha_s,y_c)$.

The total cross section is calculated only to $\mathcal{O}(\alpha_s)$, however $R_{2+1}(Q^2,y_c)$ is correct to $\mathcal{O}(\alpha_s^2)$ as can be seen by a Taylor expansion. Skipping the arguments one gets

$$\begin{aligned} R_{2+1}(Q^2,y_c) &= \frac{\alpha_s A_{31} + \alpha_s^2 A_{32}}{A_{20} + \alpha_s(A_{21} + \tilde{A}_{31})} \\ &= \alpha_s \frac{A_{31}}{A_{20}}\left[1 + \left(\frac{A_{32}}{A_{31}} - \frac{A_{21}+\tilde{A}_{31}}{A_{20}}\right)\alpha_s + \mathcal{O}(\alpha_s^2)\right] \end{aligned} \tag{6.2}$$

Inverting equation 6.1 one gets a formula for α_s as function of the coefficients and the ratio $R_{2+1}(Q^2,y_c)$.

$$\alpha_s(Q^2) = \mathcal{F}\left[A_{ij}(Q^2,y_c), R_{2+1}(Q^2,y_c)\right] \tag{6.3}$$

$$\begin{aligned} &= -\frac{g - h\cdot R_{2+1}(Q^2,y_c)}{2} \pm \sqrt{\frac{(g-h\cdot R_{2+1}(Q^2,y_c))^2}{4} + f\cdot R_{2+1}(Q^2,y_c)} \\ &\mathit{with:} \\ f &= \frac{A_{20}}{A_{32}}, \qquad g = \frac{A_{31}}{A_{32}}, \qquad h = \frac{A_{21}+\tilde{A}_{31}}{A_{32}} \end{aligned} \tag{6.4}$$

A measured $R_{2+1}(Q^2,y_c)$ in the experiment can be translated via equation 6.4 into a measurement of $\alpha_s(Q^2)$.

The strategy is to measure $R_{2+1}(Q^2_{k,e},y_c)$ at different Q^2_k, translate it to $\alpha_s(Q^2_k)$, and minimize the χ^2 of the measurement and the expectation as a function of the only free parameter $\Lambda^2_{n_f,\overline{MS}}$.

$$\chi^2(\Lambda^2_{n_f,\overline{MS}}) = min\sum_{k=1}^{N}\frac{\left[\alpha_s(Q^2_k) - \alpha_s(Q^2_k,\Lambda^2_{n_f,\overline{MS}})\right]^2}{\left[\sigma\left[\alpha_s(Q^2_k)\right]\right]^2} \tag{6.5}$$

Where $\alpha_s(Q^2_k,\Lambda^2_{n_f,\overline{MS}})$ is the 2-loop formula (cf. equation 2.5) and $\sigma\left[\alpha_s(Q^2_k)\right]$ the experimental error. The error propagation is as follows.

$$\begin{aligned} \sigma\left[\alpha_s(Q^2_k)\right] &= \frac{\partial\alpha_s(Q^2_k)}{\partial R_{2+1}(Q^2,y_c)}\cdot dR_{2+1}(Q^2,y_c) \\ &= \left(\frac{h}{2} \pm \frac{2f - h(g - h\cdot R_{2+1}(Q^2,y_c))}{4\cdot\sqrt{\frac{(g-h\cdot R_{2+1}(Q^2,y_c))^2}{4} + f\cdot R_{2+1}(Q^2,y_c)}}\right)\cdot dR_{2+1}(Q^2,y_c) \end{aligned} \tag{6.6}$$

In this scheme $\alpha_s(Q^2)$ is measured at k different scales in one experiment and one does not have the problem of combining experiments with different systematic uncertainties.

6.2 The differential jet rate $D_2(y_c)$

Another useful variable to measure α_s is the differential jet rate $D_2(y_c)$ [32] which is defined as

$$D_2(y_c) \quad = \quad R_{2+1}(y_c) - R_{2+1}(y_c + \Delta y_c) \tag{6.7}$$

$D_2(y_c)$ is essentially the number of events which flip from a (2+1)-jet configuration to a (1+1)-jet configuration in a given interval Δy_c of the jet resolution parameter y_c. Here, in contrast to [32] it is scaled by the total number of events. The differential jet rates of the higher jet multiplicities $D_3(y_c)$ and $D_4(y_c)$ are defined analogously.

$$\begin{aligned} D_3(y_c) &= R_{3+1}(y_c) - R_{3+1}(y_c + \Delta y_c) + D_2(y_c) \\ D_4(y_c) &= R_{4+1}(y_c) - R_{4+1}(y_c + \Delta y_c) + D_3(y_c) \end{aligned}$$

This quantity has the desired feature that the points in the $D_2(y_c)$ distribution are not correlated, and therefore it allows to fit the shape and not only the value at a particular y_c point as one does if one uses the $R_{2+1}(Q^2, y_c)$ distribution (cf. section 6.1). This quantity is frequently used at LEP to measure α_s. It was seen at LEP that in the low y_c region this distribution is not well described by fixed order calculations to $\mathcal{O}(\alpha_s^2)$. This improves by adding higher order terms in the framework of resummed calculations (cf. section 5.2), allowing α_s to be derived with a smaller theoretical error [33] and with x_μ values close to unity. Unfortunately the low y_c region is the one with the highest statistics. With increasing y_c the statistics is reduced rapidly. With the present statistics this measure will not be considered, only the feasibility of such a measurement will be shown in section 11.3.

6.3 $R_{2+1}(Q^2, y_c)$ versus the (2+1)-jet cross section

The next measure discussed here is the (2+1)-jet cross section. Inserting equations 3.7 and 5.1 in equation 3.9 one derives a relation between y_c and ξ.

$$\xi = x \cdot (1 + \frac{\hat{s}}{Q^2}) = x \cdot (1 + \frac{y_c W^2}{Q^2}) = x + y_c \cdot (1 - x) = y_c + x \cdot (1 - y_c) \tag{6.8}$$

From this it can be seen that for the (2+1)-jet events the PDF is evaluated at $\xi > y_c$. For $y_c \geq 0.02$ this is a region where the PDF's are constrained by measurements (cf. figure 3.8) whereas for the (1+1)-jet events $\hat{s} \to 0$ and $\xi \to x$, which can be much smaller than 10^{-2} (cf. figure 9.1). This means normalizing the (2+1)-jet fraction to the total number of events introduces a systematic uncertainty due to the unknown PDF function at low ξ values. This uncertainty can be circumvented by only considering the (2+1)-jet cross section. The drawback here is that one needs to know precisely all efficiencies, which in the case of using $R_{2+1}(Q^2, y_c)$ mostly cancel. The event selection relies mainly on the electron, consequently quantities like electron trigger efficiency and detection efficiency cancel out. There is also no uncertainty on the luminosity in $R_{2+1}(Q^2, y_c)$ which at present is around 7% for the 1993 data sample. The way to overcome this is to restrict ξ to the region where the PDF's are well constrained and to use $R_{2+1}(Q^2, y_c)$ (cf. section 11.5).

In this study, for the reasons mentioned above, the (2+1)-jet jet cross section will not be considered as a measure for α_s, although it may be the prefered one at a later stage, when the efficiencies and the luminosity are understood more accurately. To illustrate the method the (2+1)-jet cross section is shown in section 11.4, using a simple model of unit efficiencies (cf. table 11.2).

6.4 Scaling violations in structure functions

The last method described is the evaluation of α_s from scaling violations in structure functions. This is a different type of method which does not rely on jet cross sections.

QCD predicts the evolution of structure functions analogous to the discussed prediction of the PDF's (cf. equation 3.18). The measurement of the slope of the structure function evolution with μ^2 is a measurement of α_s.

$$\frac{dF}{d\log(\mu^2)} \sim \alpha_s(\mu^2) \tag{6.9}$$

The α_s measurements (DIS [ν],DIS [μ] in tab 2.1) are of this type. An example of a recent measurement from the NMC Collaboration can be found in [34].

At HERA there exists the possibility the measure α_s from jet final states and from scaling violations of structure functions. The advantage of HERA compared to the earlier experiments, for example NMC, is the much higher momentum transfer Q^2, and consequently μ^2, probed at HERA, leading to smaller uncertainties due to non perturbative effects (cf. section 2.2). This gives a unique possibility to solve the outstanding puzzle mentioned in section 2.2 that α_s values derived from scaling violations are somewhat smaller than those obtained from hadronic final states. This is a future task and is not covered in this work.

Chapter 7

The machinery to generate DIS events

This section deals with the properties of event generators as they are used in the H1 collaboration [46]. Only the main features are considered, the details can be found in the corresponding manuals.

The general procedure is as follows. The starting point are the matrix elements to a given order, either $\mathcal{O}(\alpha_s^o)$ or $\mathcal{O}(\alpha_s)$. An alternative approach to simulate QCD Compton events is the colour dipol model (CDM). In this model the gluon is radiated from a dipol built up of the quark and the proton rest, a diquark. After this, softer emissions of gluons may be simulated by leading logarithmic (LL) approximations to all orders in α_s called parton showers (PS or LLPS), or by subsequent emissions in the framework of the CDM. The partonic final state of quarks and gluons will be fragmented, either by cluster fragmentation or lund string fragmentation, resulting in the hadronic final state. The various event generators differ in the choices made for the steps described above, and if they include radiative corrections on the electron arm or not.

The radiative corrections are photon emissions from the electron, either in the initial state or in the final state, and virtual corrections at the $e \to e'\gamma$ vertex. All these corrections are simulated in HERACLES [35], which calculates cross sections but does not simulate the hadronic final state. To overcome this HERACLES can be combined with LEPTO52 [36]. This combination results in a generator called DJANGO10 [37]. Due to technical reasons, in this configuration LEPTO52 can only be operated with matrix elements to $\mathcal{O}(\alpha_s^o)$, followed by parton showers. For this analysis of main interest are the matrix elements in order to derive a basic physical quantity α_s, therefore DJANGO10 will not be considered in detail. Another generator which is operated in H1 with $\mathcal{O}(\alpha_s^o)$ matrix elements followed by parton showers is HERWIG55 [38]. The parton shower evolution is treated differently in HERWIG55 and LEPTO61 [39] (see below). A second conceptual difference is that HERWIG55 uses cluster fragmentation and LEPTO61 the lund string fragmentation, which is simulated using JETSET73 [40]. This opens the possibility to study the subtleties of PS and fragmentation, but it will not be discussed here in details.

The CDM model implemented in ARIADNE [41] can be used together with LEPTO61. In this combination LEPTO61 matrix elements account for the BGF process while ARIADNE is used to simulate the QCDC events.

All these generators, or combinations of generators, are of limited use for the purpose of this investigation. An event generator is needed only to evaluate correction factors to allow the measured jet rates to be related to the jet rates on parton level, which then will be compared to the 'real' QCD predictions of PROJET. The ideal thing to use would be an event generator with matrix element to $\mathcal{O}(\alpha_s^2)$ followed by parton showers. The model which comes closest to this at the moment is LEPTO61 used in the option where it simulates the matrix elements $\mathcal{O}(\alpha_s)$ followed by parton showers to account for softer radiations. It will be used for this task. This model will be called MEPS from now on, LEPTO61 with matrix elements $\mathcal{O}(\alpha_s)$ alone is abbreviated to ME. Because LEPTO61 is the favourite generator it will be discussed in more details in the next section.

7.1 LEPTO61

LEPTO61 is an event generator based on the LO electroweak cross section for γ and Z° exchange. It includes QCD corrections using the matrix elements to $\mathcal{O}(\alpha_s)$ and higher orders in a LLPS approach. No QED corrections at the electron arm are included. Fragmentation is done in the framework of the lund string model.

7.1.1 Hard matrix elements

LEPTO61 simulates the leading order process and the BGF and QCDC process to $\mathcal{O}(\alpha_s)$. In the terminology of the LEPTO program these processes are called q, $q\bar{q}$ and qg events refering to the outgoing partons. In order to save computing time, during the initialization phase of the program it evaluates a probability table for the different event types on a grid in (x, W^2) in the following way. The three additional degrees of freedom [1] for the BGF and QCDC process are integrated out, to derive the differential cross sections $d^2\sigma/dx \cdot dQ^2$ for $q\bar{q}$ and qg events. To get the probabilities $P_{q\bar{q}}$ and P_{qg} these differential cross sections are scaled by the overall differential cross section $(d^2\sigma/dx \cdot dQ^2)_{tot}$, which is available to $\mathcal{O}(\alpha_s^o)$ and to $\mathcal{O}(\alpha_s)$ in the DIS scheme. The probability for q-events is obtained by probability conservation.

$$P_q = 1 - P_{q\bar{q}} - P_{qg} \tag{7.1}$$

The BGF and QCDC cross sections depend strongly on the minimum y_c up to which the integration is performed. y_c can be steered, as well as the minimal absolute invariant mass of any parton pair m_{ij}^2 [2]. One wants to generate as many events as possible according to the $\mathcal{O}(\alpha_s)$ matrix elements in order to get the appropriate final state, however, the problem is that the matrix element diverges for low y_c values, resulting in a negative probability for the LO process. The program solves this by increasing internally y_c if needed in order to keep P_q above 10%. As a consequence of this the actual y_c values may change from point to point in phase space, indicating that one has to be careful while comparing LEPTO to an analytical calculation. This grid is stored and used during event generation.

The event generation is usually done according to $(d^2\sigma/dx \cdot dQ^2)_{tot}$ in (x, Q^2) space. At any (x, Q^2) point the type of event is chosen by linear interpolation in the (x, W^2) probability grid. If an $\mathcal{O}(\alpha_s)$ event is generated the three degrees of freedom are chosen according to the five fold differential cross sections.

[1] Because there are two outgoing partons from the hard subprocess instead of one in the LO process three additional degrees of freedom are present in the BGF and QCDC process. They can be chosen as two angles and the energy of one parton, the other parton is then fixed by momentum conservation.

[2] Parameters PARL(8), PARL(9) in LEPTO61 with the default values 0.015, 2.0 GeV.

7.1.2 Leading logarithmic parton showers LLPS

The matrix elements, calculated for massless quarks, govern the jet cross sections, on top of this the event topology is changed by the parton showers which treat the partons as offshell.

The PS approach has been developed to simulate arbitrarily high orders in α_s because the multijet rate in e^+e^- annihilations was not properly described by the second order matrix element approach, which accounts for at most four partons in the final state (FS). This multiparton approach also gives a better description of jet properties, such as hardness or width of jets for e^+e^- interactions. In e^+e^- scattering quarks and gluons only occur in the final state, with timelike virtualities $m^2 > 0$. A strategy to perform the FSPS was developed and implemented in the subroutine LUSHOW of JETSET73, which has been well tuned to e^+e^- data.

In DIS the incoming parton from the proton side is a quark or gluon and consequently there exist an initial state parton shower (ISPS) with space like virtualities $m^2 < 0$. In the pure PS approach one starts from the QPM process and on top of this both the ISPS and FSPS are evolved by subsequent branchings controlled by the Altarelli Parisi splitting kernels. To explain the features of PS a 'chronological' picture (cf. figure 7.1) of the PS evolution is helpful.

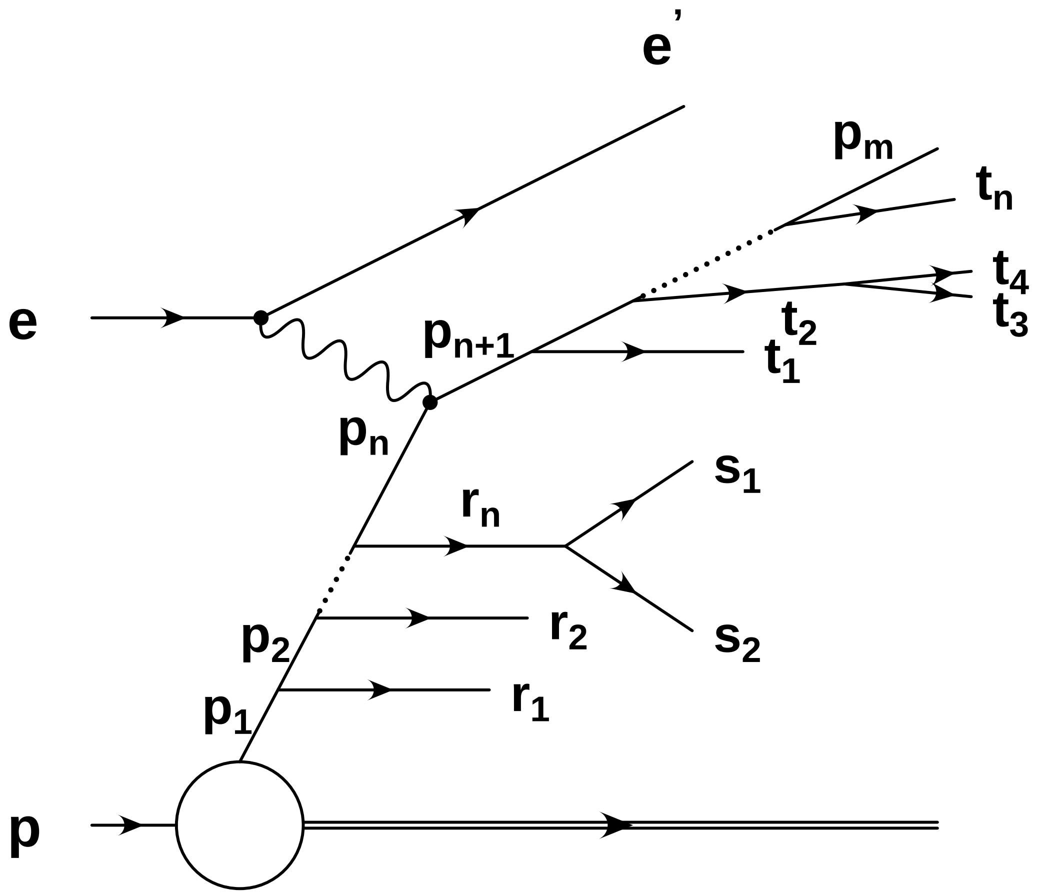

Figure 7.1: *Parton shower evolution in an ep scattering event.*

Starting from a quark in the proton which is close to onshell, branchings take place which decrease the virtuality of the quark ($0 > m^2_{p_1} > \ldots > m^2_{p_n}$), it becomes more and more spacelike. The radiated daughters ($r_1 \ldots r_n$) are either onshell or have timelike virtualities which in turn will result in a timelike shower ($s_1 \ldots s_n$). When the quark (p_n) is hit by the photon it will be turned to onshell or to a timelike virtuality $m^2_{p_{n+1}} \geq 0$. It radiates partons $(t_1 \ldots t_n)$ thereby decreasing it's virtuality until $m^2_{p_m} \leq p_0^2 \approx 1\ GeV^2$, at which point it enters the fragmentation region, and the PS is stopped. In the FSPS branchings angular ordering is taken into account which leads to decreasing opening angles for $(t_1 \ldots t_n)$. The probability for each branching is ruled by the Sudakov form factor derived from the Altarelli Parisi equation by integrating the no branching probability over the changes in virtuality. Technically the ISPS is done in a backward evolution scheme, one starts from the photon vertex and constructs the ISPS down to the proton. The cross section is governed by the x value as seen by the electron and the ISPS is constructed with unit probability. It can be looked at as a 'snapshot' of a specific fluctuation state of the proton which is in agreement with the Altarelli Parisi evolution equation. ISPS must be included in an event generator to simulate properly the partons generated by the ISPS, which may be seen in a detector. When combining ISPS and FSPS special precautions are taken to preserve the kinematic variables at the photon vertex, especially the x value as seen from the electron arm. One shortcoming of the separate evolution is the fact that no interference terms between ISPS and FSPS are taken into account, thereby violating the gauge invarianz.

To complete the procedure two choices have to be made. First one has to define the argument in $\alpha_s(\mu^2)$ which is set to $\mu^2 = p_t^2 \approx (1-z)Q^2$ for ISPS and to $\mu^2 = p_t^2 \approx z(1-z)m^2_{max}$ in FSPS.

The second choice is the value of the maximum allowed virtuality m^2_{max}, which is the crucial parameter in PS. It can not be fixed by first principles in QCD, only recipes exist how to fix this ambiguity. Those have to be checked against data. It has been argued [42] that the mean transverse momentum $\langle p_t^2 \rangle$ is proportional to W^2 for $x > 0.01$ and therefore W^2 is the preferred scale, on the other hand the fundamental parameter in matrix elements is Q^2. For small x it follows $W^2 \gg Q^2$ and the proton remnant P_r with $P_r = (1-\xi)P$ takes a lot of the available W^2, but it does not radiate because according to the spectator model it is treated onshell. Due to this, taking W^2 as the scale of maximum virtuality will overestimate the amount of radiation.

A way round this problem is the choice of $m^2_{max} = Q^2(1-x)max(1, \log\frac{1}{x})$. This takes into account the limites of $\langle p_t^2 \rangle$ for $(x \to 1, x \to 0)$ and is the actual default choice in LEPTO61.

Because the PS is a leading logarithmic approximation it is expected to simulate properly the soft and collinear emissions. However, the emissions of high energetic partons or emissions at large angles are wrongly treated because the approximation runs out of it's validity range, in particular hard jets generated by LLPS should be treated with special precaution.

A natural improvement is to use the matrix elements $\mathcal{O}(\alpha_s)$ for the hard emissions and use LLPS on top of that to account only for the softer part. This needs a matching procedure of the matrix elements to the LLPS to get a smooth transition, which is the subject of the next section.

7.1.3 Matching first order matrix element to LLPS

The main task in matching matrix elements to parton showers is to get a smooth transition between ME and PS. If there is an overlap in phase space this will lead to double counting. Double counting denotes the fact that an emission which was rejected on the ME level by the P_{ij} (cf. equation 7.1) is generated through PS afterwards. In order to avoid this, m^2_{max} must be determined event by event from the matrix element.

The FSPS is performed by LUSHOW. The procedure for the ISPS performed in LEPTO61 is the following. If an $\mathcal{O}(\alpha_s^o)$ event is chosen according to equation 7.1, then no radiation, leading to an invariant mass squared of any two partons larger than $y_c \cdot W^2$, is generated by ME and PS is not allowed to do so either, $y_c \cdot W^2$ is the choice for m^2_{max}. For $\mathcal{O}(\alpha_s)$ events the situation is more complex. The m^2_{max} is chosen as the virtuality of the parton which is hit by the photon before this interaction, however, for instance, in a BGF event it is not clear whether the q or $\bar{q}$ was hit by the photon. The two possibilities lead to the same final state they are indistinguishable and according to the Feynman rules they are added on amplitude level to get the matrix element. If one works out the values of the invariant masses for the two cases using four vector arithmetics one sees that often they are numerically very different. This ambiguity is solved in LEPTO using the maximum of the two choices, unless the result is bigger than $(m^2_{ij} + Q^2/2)$. This is a possible solution to the problem, however it must not be the ultimate one. To choose the minimum of the two invariant masses as the scale of maximum virtuality is a valid choice as well. The cross section even diverges if this internal line is onshell, so it should happen frequently that it's invariant mass is small.

The importance of that will be addressed later, when the jet requirements of this analysis are defined (cf. section 10.2).

7.2 Comparison of PROJET with LEPTO

PROJET and LEPTO61 are used in parallel, so it is natural to compare those parts of PROJET which are included in LEPTO61 as well. For comparison shown are the LO contribution to σ_{tot} and the (2+1)-jet cross section using the ME option in LEPTO61 with *MRSD°* as PDF. For LEPTO61 200.000 events per bin are generated, the total cross section is taken as the value obtained from the numerical integration of the initialization step of the program, the (2+1)-jet cross section in turn is derived from the relative number of generated events [3]. The PROJET cross sections are integrated with an accuracy better than 1%. These are not consistent jet cross sections, in terms of LO or NLO jet cross sections as discussed in section 3.3, but they only serve as a technical consistency investigation in order to see whether the parts of the matrix elements included in both programs agree. To avoid the heavy flavour threshold factors in LEPTO61 integration is done for four flavours only. Special precaution is necessary because all relevant parameters have to be steered properly [4], especially the chosen formula to evaluate α_s is the crucial point here. Table 7.1 shows the comparison for the five bins in Q^2 discussed in section 9.2. An agreement in the order of 1 % in different kinematic regions is achieved. The phase space restriction is based on electron variables and variables concerning the hadronic final state. The jet rates are evaluated for two y_c values, $y_c = 0.02$ and 0.03. This valuable cross check shows that the restrictions in phase space made while integrating in PROJET and LEPTO61 are the same, giving the confidence that phase space integration is correctly implemented in both programs. In addition the common parts of the matrix elements are found to give the same y_c dependence of the (2+1)-jet cross sections. This agreement is the justification to use LEPTO61 to perform the correction from the detector level to the parton level.

[3] In LEPTO61 the cross section is stored in PARL(23) and the event type can be accessed by LST(24).

[4] The following parameters are chosen different from their default values. LST(7)=0, LST(13)=4, LST(18)=1, PARL(3)=0, PARL(9)=0.001, PARL(15)=0.005, MSTU(112)=4, MSTU(114)=4, PARU(112)=0.2

PDF	process		Bin 1	Bin 2	Bin 3	Bin 4	Bin 5
LEPTO61	σ_{tot}	[pb]	13059	7954.6	7003.8	1316.0	582.0
$y_c = 0.02$	σ_{2+1}	[pb]	364.6	323.8	470.3	142.0	109.7
	QCDC	[pb]	102.6	93.1	152.7	65.9	72.6
	BGF	[pb]	262.0	230.7	317.7	76.1	37.2
$y_c = 0.03$	σ_{2+1}	[pb]	185.4	165.0	244.1	82.3	68.9
	QCDC	[pb]	54.5	51.5	81.9	39.5	45.7
	BGF	[pb]	130.9	113.5	162.1	42.8	23.2
PROJET	σ_{tot}	[pb]	12956	7906.1	6980.5	1299.2	574.6
$y_c = 0.02$	σ_{2+1}	[pb]	363.8	326.3	460.9	140.2	109.6
	QCDC	[pb]	98.5	92.1	146.4	64.5	72.6
	BGF	[pb]	265.3	234.2	314.5	75.7	37.0
$y_c = 0.03$	σ_{2+1}	[pb]	185.0	166.9	243.9	81.1	68.9
	QCDC	[pb]	55.7	51.8	82.8	38.1	45.9
	BGF	[pb]	129.3	115.1	161.1	43.0	23.0

Table 7.1: *Comparison of LO contributions to cross sections for LEPTO61 and PROJET for different y_c values. The bins are defined in table 9.2. For more explanations see text.*

Chapter 8

HERA and the H1 Detector

HERA, the 'Hadron Elektron Ring Anlage' shown in figure 8.1, is situated at DESY in Hamburg, Germany. It has a circumference of 6.3 km. In HERA electrons of momentum 26.7 GeV collide with 820 GeV protons. To cope with the high momentum of the proton and to operate the electron and proton accelerators at the same radius, meaning in the same tunnel, one needs strong magnetic fields. The proton accelerator is built with superconducting magnets (B = 4.68 T). The particles are grouped in bunches separated by 96 ns. In the 1993 operation period

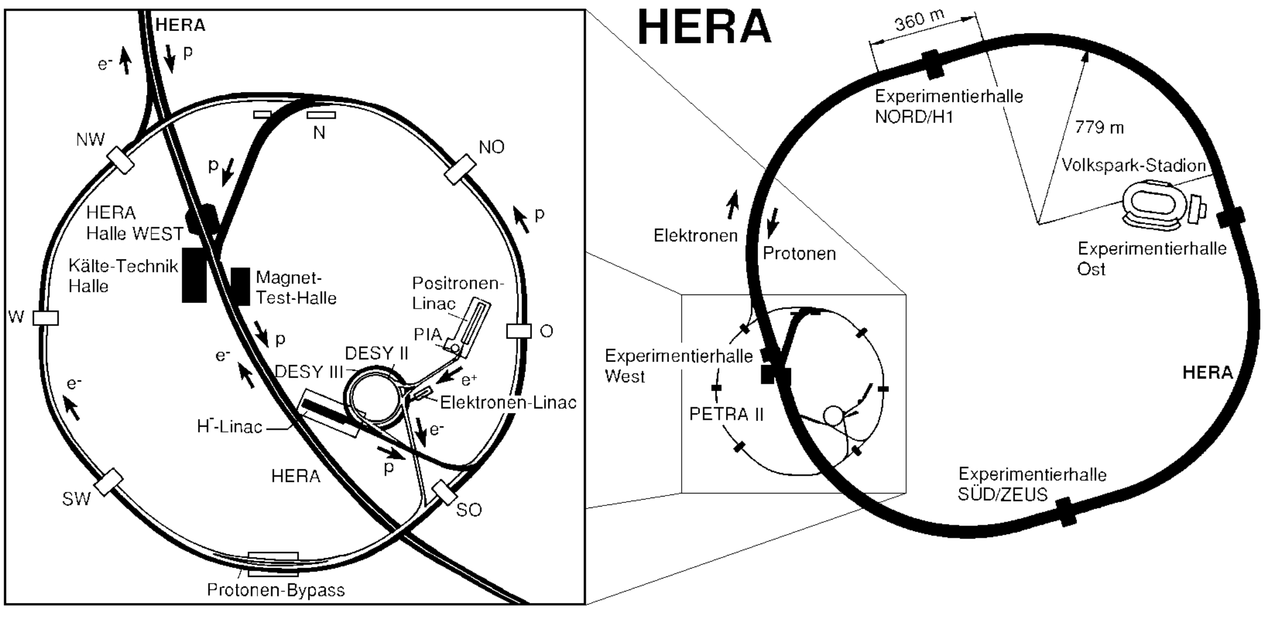

Figure 8.1: *The HERA accelerator.*

84 bunches of each type were made to collide [1]. Typical currents of 14 mA for the proton beam and 12 mA for the electrons have been achieved leading to a typical specific luminosity of 500 $mb^{-1}\, s^{-1}\, mA^{-2}$. In 1993 HERA delivered $\approx 1\, pb^{-1}$ integrated luminosity, and the H1

[1] The design values for the bunch lengths of the electron and proton beams are 11 cm and 0.8 cm respectively.

experiment collected $\approx 0.4\,pb^{-1}$ of data with all relevant detector components operated under normal conditions.

A detailed discussion of the H1 apparatus can be found elsewhere [43]. Here emphasis is put on describing the main features of the components of the detector relevant to this analysis, which mainly makes use of the calorimeters, and to a lesser extent the central and backward tracking systems. The description proceeds from the interaction point outward, always refering to the abbreviations in figure 8.2 which shows a sketch of the main components of the H1 detector. The inner part of the detector is filled with the central tracking chamber (CT)

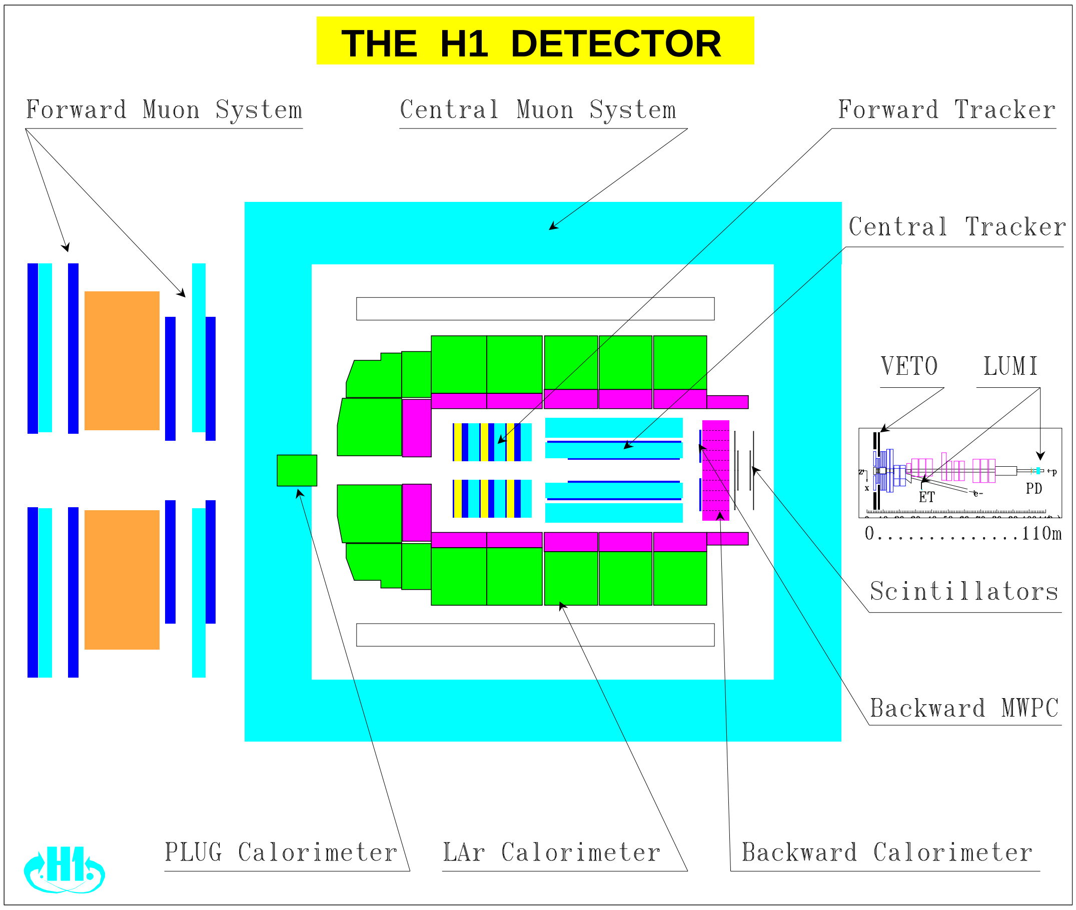

Figure 8.2: *The H1 detector.*

supplemented by a forward tracking detector (FT) and a backward multiwire proportional chamber (BPC or MWPC), covering the polar angle ranges $25° < \vartheta < 155°$, $7° < \vartheta < 25°$ and $155° < \vartheta < 175°$, respectively. These sub-detector devices are used to determine the vertex position, which is within the range of ± 50 cm around the nominal interaction point, due to the bunch lengths mentioned earlier. The BPC, together with the vertex, is used to measure the electron scattering angle in the backward region. The achieved angular resolution is about 6 mrad.

The scattered electrons and the hadronic energy flow are measured in a liquid argon (LAr) calorimeter and the backward electromagnetic lead-scintillator calorimeter (BEMC). Leaking hadronic showers are measured in a surrounding instrumented iron system housed in the return yoke of the superconducting solenoid. The solenoid is outside the LAr calorimeter and provides a uniform magnetic field of 1.15 T parallel to the beam axis in the tracking region.

The LAr calorimeter [44] extends over a polar angle range from $4^0 < \vartheta < 153^0$ with full azimuthal coverage. The calorimeter consists of an electromagnetic section (EMC) with lead absorbers, corresponding to a depth of between 20 and 30 radiation lengths and a hadronic section (HAC) with steel absorbers. The total depth of the LAr calorimeter varies between 4.5 and 8 hadronic interaction lengths. The calorimeter is highly segmented in both sections with a total of around 45000 geometric cells. The electronic noise per channel is typically in the range 10 to 30 MeV (1 σ equivalent energy). The energy reconstruction method is described in [43, 45]. Testbeam measurements of LAr calorimeter modules have shown energy resolutions of $\sigma(E)/E \approx 0.12/\sqrt{E\ /GeV} \oplus 0.01$ for electrons and $\sigma(E)/E \approx 0.5/\sqrt{E\ /GeV} \oplus 0.02$ for charged pions [43, 45]. The hadronic energy scale and resolution have been verified from the balance of transverse momentum between hadronic jets and the scattered electron in DIS events and are known to a precision of 5% and 20% respectively. The uncertainty of the absolute scale for electrons is at the level of 3%.

The BEMC, with a thickness of 22 radiation lengths, covers the backward region of the detector, $151° < \vartheta < 177°$. It is mainly used to trigger on and to measure electrons scattered from DIS processes at low Q^2. The acceptance region corresponds to Q^2 values in the approximate range $5 \leq Q^2 \leq 100\ GeV^2$. A resolution of $\sigma(E)/E \approx 0.10/\sqrt{E\ /GeV}$ with a constant term of 3% has been achieved. By adjusting the seen electron energy spectrum to the kinematic peak [2], the BEMC energy scale is known to an accuracy of 1.7%.

A scintillator hodoscope situated behind the BEMC is used to veto proton-induced background events based on their early time of arrival compared to that of the nominal electron-proton collision.

A luminosity detector measuring the reaction $e\,p \rightarrow e'\,\gamma\,p$ is placed in the backward direction with components at $z = -33$ m to tag electrons (ET) scattered through angles below 5 mrad with respect to the electron beam direction and at $z = -100$ m to measure photons (PD). Each component consists of a crystal calorimeter with an energy resolution of $\sigma(E)/E \approx 0.10/\sqrt{E\ /GeV}$

[2] As can be seen from figure 3.2 there exists a large region of phase space where the energy of the scattered electron is close to the energy of the incident electron, this is called the kinematic peak.

Chapter 9

Trigger and Event Selection

The analysis is split into two data samples depending on if the scattered electron is detected in the BEMC or the LAr calorimeter. The event selection is similar to the one discussed in [46], with some additional requirements.

Selecting DIS events is based as much as possible on quantities measured by the electron in order not to bias the hadronic final state to specific jet configurations. The electron should be well contained in the calorimeters. The matching of data samples is done via bins in Q^2 (cf. figure 9.1). The BEMC sample is restricted to the range $10 \leq Q^2 \leq 100\ GeV^2$, the LAr sample to $Q^2 > 100\ GeV^2$. The distribution of the events in the $(x_e,\ Q_e^2)$ plane is shown in figure 9.1. A typical event from both samples is shown in figure 9.2 for the BEMC sample and 9.3 for the LAr sample. These events are subject to the jet analysis.

9.1 Electron identification and data samples

This section first describes the common requirements, then the selection of the BEMC sample, and finally the LAr sample.

The common requirements are

- an event vertex within ± 50 cm in z from the nominal interaction point
- $W^2 > 5000\ GeV^2$ calculated using the double angle method [14]. The W^2 cut for low Q^2 is equivalent to a lower y cut (cf. equation 3.7), ensuring that the radiative corrections are strongly suppressed. In addition it ensures a large invariant mass of the hard subsystem $\hat{s} > 100\ GeV^2$ for (2+1)-jets at $y_c > 0.02$. This method relies on the angle of the scattered electron and the angle of the total hadronic system and not on the details of the jet final state.

The electron for the BEMC sample is selected as follows. The electron requires

- an electromagnetic cluster in the BEMC, matching with a space point in the BPC, in the range $160° < \vartheta_e < 172.5°$
- the center of gravity of the electron cluster to have $|x|$ or $|y| > 14$ cm to be well inside the BEMC, avoiding the inner triangular stacks of the BEMC
- a momentum transfer measured by the electron Q_e^2 between 10 and 100 GeV^2

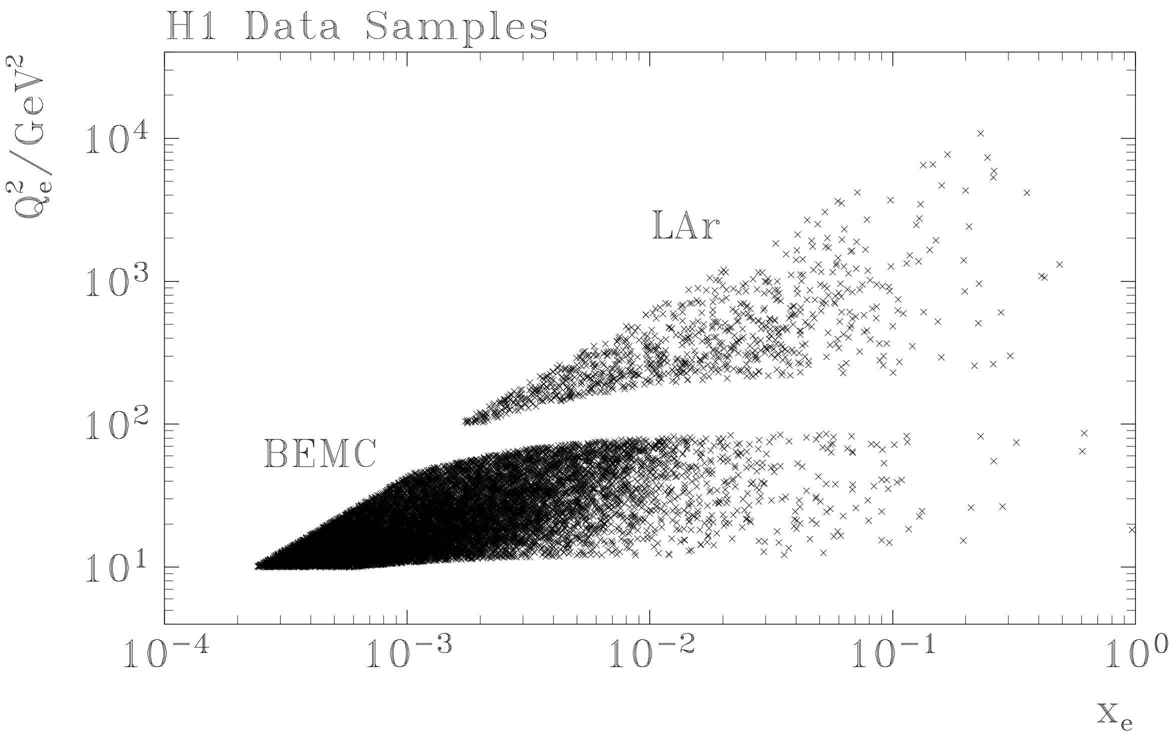

Figure 9.1: *H1 data event distribution in the (x_e, Q_e^2) plane. The impacts of the kinematic cuts described in chapter 9.1 can be seen by comparing to figure 3.2.*

- an energy $E_e > 14\ GeV$ corresponding to $y_e \lesssim 0.5$, to eliminate possible background from photoproduction.

With these requirements the trigger efficiency is $> 99\,\%$ [47].

In the LAr sample the scattered electron is mainly selected using the kinematic fact that the electron has to balance the hadronic system. The transverse momentum of the initial beam particles e and p vanishes. This leads to a balance of transverse momentum between the electron and the hadronic final state, and so the electromagnetic cluster with the highest transverse momentum is likely to be caused by the electron.

In order to reduce faked electrons caused by non DIS events some additional features for these clusters are required. These background events are mainly cosmic muons which shower in the LAr calorimeter or muons accompanied with the proton beam, called halo muons. Their showers mostly do not originate at the inner edge of the EMC and they do not point to the vertex. This means, these events have very different shower profiles compared to showers produced by electrons originating from the event vertex. This difference enables the isolation cuts, described below, to be obtained.

- $Q_e^2 > 100$
- $y_e < 0.7$ to reduce the photoproduction background

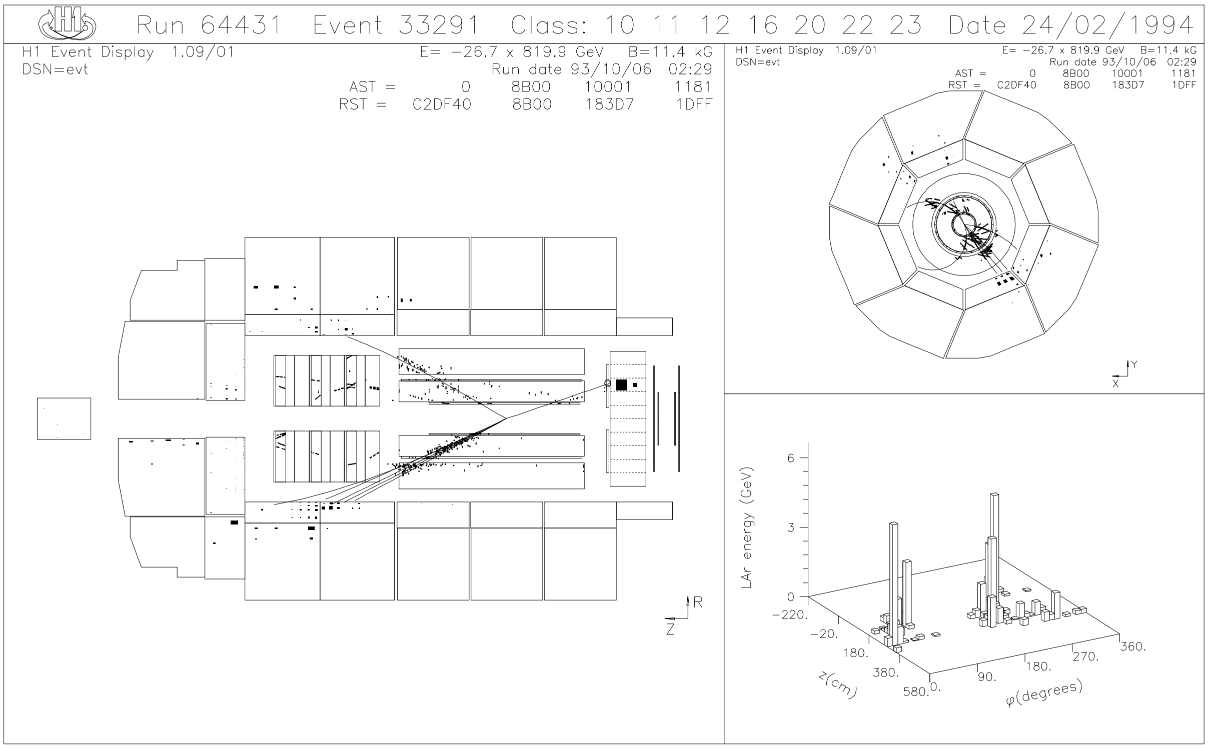

Figure 9.2: *A H1 data event with the electron scattered in the BEMC calorimeter.*

- $10° < \vartheta_e < 148°$ to contain the cluster in the LAr calorimeter and to avoid the transition region between LAr and BEMC
- in a cone of 5° half opening angle around the direction of the electron no muon track is allowed in the instrumented IRON system
- the electron must not be near to an acceptance hole in the azimuthal coverage of the LAr calorimeter
- the energy deposited in the EMC in a cylinder of radius $15 \leq r \leq 30$ cm around the electron direction must be below 1.2 GeV to ensure that the electron is isolated. The energy in the HAC within 30 cm around the electron direction must be less than 0.5 GeV.

In this sample the trigger efficiency is $> 97\,\%$.

To demonstrate the purity of the LAr sample figure 9.4 shows several control distributions, namely the energy found in the electron tagger (ET) (a), the value of the total $(E - P_z)_{tot}$ of the event (b), the energy of the most energetic cluster in the BEMC (c) and the distribution of the z coordinate of the vertex position (d). Compared are the H1-data to the prediction of MEPS for the LAr sample after the event selection described above. The events with energy in the ET are found to be overlay events, where in addition to a DIS event also a Bremsstrahlungs event from the electron beam occurs. The Bremsstrahlung events have a large cross section

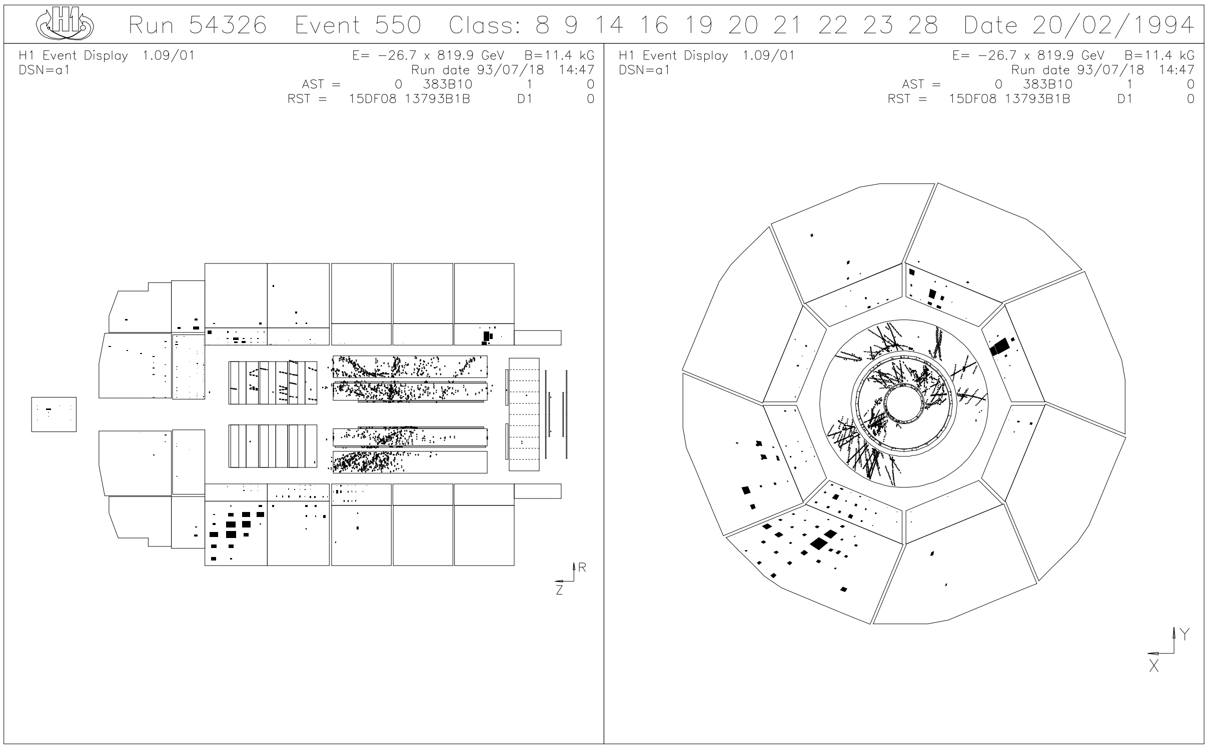

Figure 9.3: *A H1 data event with the electron scattered in the LAr calorimeter.*

and are usually used to measure the luminosity (cf. section 8). The number of overlay events of this type roughly agrees with that expected from the cross sections involved. Most of them have also the Bremsstrahlungs photon detected in the PD. These events are not simulated by MEPS. They do not disturb the measurement of the DIS events and remain in the sample.

The $(E - P_z)_{tot}$ expectation is twice the initial electron energy predicted by momentum conservation and the distribution (b) peaks around this value. The tail at high values of $(E - P_z)_{tot}$ is produced mainly due to resolution effects, while that at low $(E - P_z)_{tot}$ values is caused by not seen particles due to the imperfect coverage of the detector. This may occur in DIS events, however, it also indicates possible background from photoproduction, where the scattered electron escapes unseen in the incoming electron beam direction (- z). This results in a loss of the measured $(E - P_z)_{tot}$ with almost twice the electron energy. The distribution is reasonably well described by MEPS with a small additional tail in the data distribution, indicating a tiny background from photoproduction. This can happen if an electromagnetic cluster, from the hadronic final state, is misidentified as an electron.

Another type of dangerous background event is a DIS event with a wide angle Bremsstrahlung in the final state. This leads to two isolated clusters from the electron and the photon. These events may lead to an additional jet, caused by the isolated cluster. These radiative events are not simulated by MEPS (cf. section 7.1) and also not by PROJET. A typical signature of such an event is an additional high energy cluster in the BEMC. They

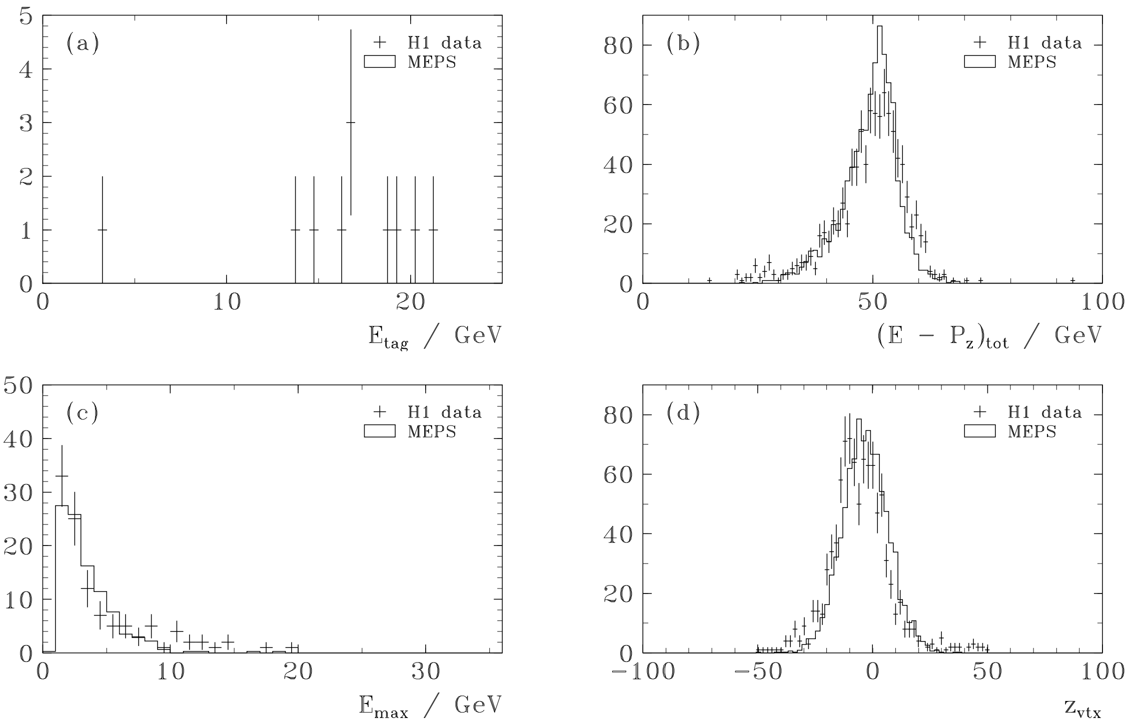

Figure 9.4: *Data quality distributions for the LAr sample, after the event selection of section 9.1. The H1 data are the points with error bars, the histogram is the MEPS prediction normalized to the same number of events.*

(a) Energy in the electron tagger E_{tag}. (no entry for MEPS, see text)

(b) The total $(E - P_z)_{tot}$ of the event.

(c) Energy of the most energetic cluster in the BEMC E_{max}.

(d) The z coordinate of the event vertex z_{vtx}.

are eliminated by rejecting those events where the energy of the most energetic BEMC cluster is above 10 GeV. This cut also eliminates background from low Q^2 DIS events, where the scattered electron is in the BEMC and an electromagnetic part of the hadronic final state is misidentified as electron in the liquid argon. Such events must be efficiently suppressed, as the cross section is much higher than the cross section for events with the electron scattered in the LAr calorimeter.

The distribution of the z vertex coordinate agrees for data and Monte Carlo, however there is a small shift in the peak position. This is more a consistency check of the Monte Carlo than of the data, because the input distribution for the z vertex coordinate used in the Monte Carlo was derived from H1 data.

For the LAr sample, in addition to the event selection, it is required.

- $30 < (E - P_z)_{tot} < 70\ GeV$

- $E_{max} < 10\ GeV$

This eliminates 46 events and after this the remaining background is smaller than 1 %. The background in the BEMC sample is negligible due to the $E_e > 14\ GeV$ cut [19].

In summary, after all the cuts described above 13641 events in the BEMC sample and 877 events in the LAr sample remain. From the events in the LAr sample 12 have a Q^2 value bigger than 4000 GeV^2.

9.2 Determination of kinematic quantities

To rely on the event selection detailed above, it has to be shown that the object found is indeed the electron, that the kinematic variables are derived with sufficient accuracy, and that the event generator used to evaluate these estimates describes the data reasonably well. This is done as follows, using MEPS with $MRSD^-$ as PDF.

Figure 9.5 shows the correlation of the scattering angle and of Q^2 for the generated and reconstructed electron in the BEMC sample, (a, b), and the LAr sample, (c, d), respectively, for the cuts described above. The electron is considered as misidentified if it is separated by more than two degrees in polar angle from the generated one. Given this, the efficiency for finding the correct electron is evaluated to be greater than 99 % for both samples.

After identifying the electron, the kinematic variables are derived. This mostly relies on the electron measurement (cf. chapter 9.1), only the evaluation of W^2 makes use of the hadronic measurement. W^2 is calculated with the double angle method [14]. The hadronic final state for this calculation is defined to be the sum of calorimetric cell energies, above the noise thresholds [1], in the LAr, IRON and BEMC calorimeters, after eliminating the energy due to the scattered electron.

With all these ingredients one achieves a data sample with high efficiency and purity, as can be seen from table 9.1. This is based on generated events, where N_{gen} is the number of

	N_{gen}	N_{rec}^{tot}	N_{rec}^{true}	efficiency	purity
BEMC	12961	12318	11598	0.90	0.94
LAr	3004	2895	2752	0.92	0.95

Table 9.1: *Data selection efficiency and purity based on the expectation of MEPS. Using efficiency errors the uncertainty of efficiency and purity are below 1 %. The generated events correspond to a luminosity of $\mathcal{L}_{int} = 0.32\,pb^{-1}$ and $\mathcal{L}_{int} = 1.47\,pb^{-1}$ for the BEMC and LAr sample respectively, both using $MRSD^-$ as PDF.*

generated DIS events fulfilling all kinematic requirements applied to the generated quantities. N_{rec}^{tot} is the number of events selected by the cuts described and N_{rec}^{true} are those events in N_{rec}^{tot}

[1] The noise suppression is described in [43]. In addition to the online noise suppression for the IRON and BEMC calorimeters, only cells above 0.2,0.5 GeV are considerd.

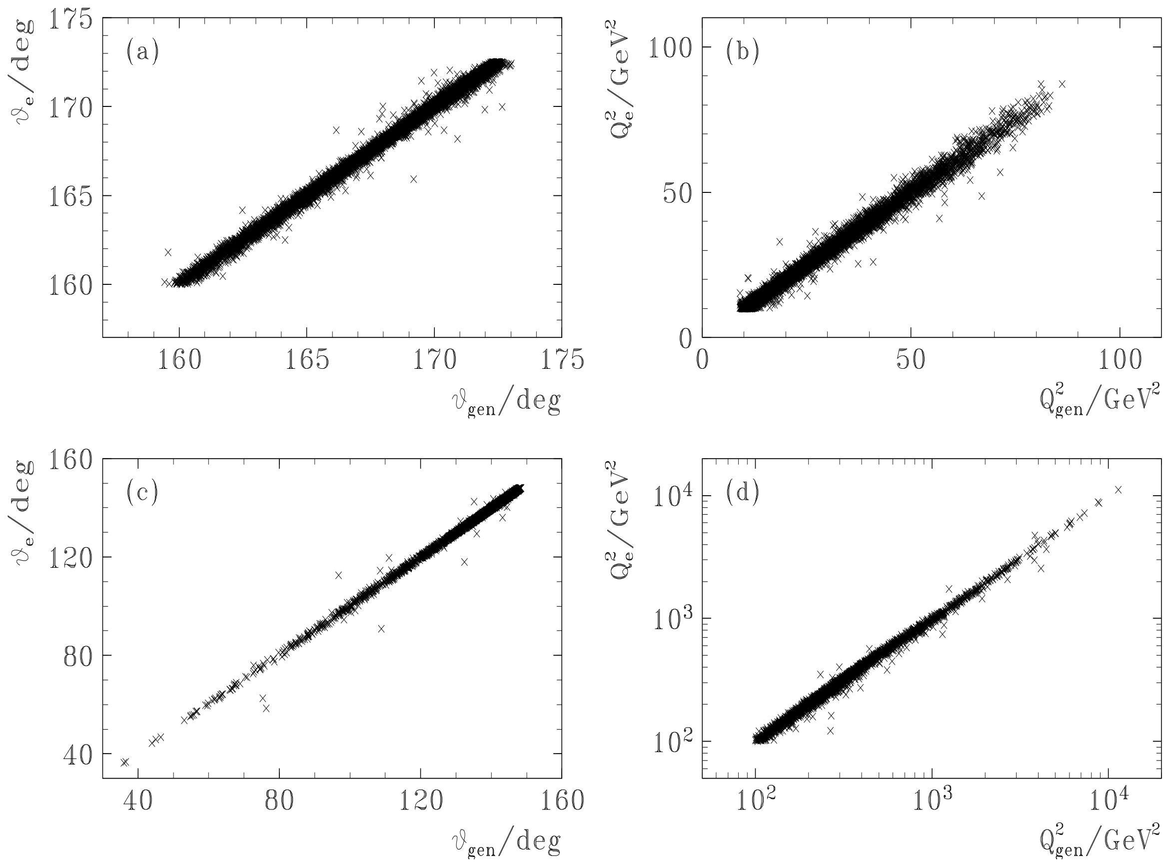

Figure 9.5: *Quality of the electron polar angle ϑ_e and Q^2_e measurement.*
(a,b) The BEMC sample.
(c,d) The LAr sample.

which are also element of N_{gen}. The efficiency is defined as N^{true}_{rec} divided by N_{gen} and the purity is N^{true}_{rec} divided by N^{tot}_{rec}. The errors are calculated as efficiency errors,

$$\sigma(\epsilon) = \sqrt{\frac{\epsilon(1-\epsilon)}{N}} \tag{9.1}$$

for example, for the efficiency calculation ϵ equals N^{true}_{rec} / N_{gen} and N is N_{gen}. The deviation of purity and efficiency from unity are due to detector inefficiencies and resolution effects at the kinematic boundaries.

In order to measure $\alpha_s(Q^2)$ one has to divide the data sample into Q^2_e bins. This needs a good resolution in Q^2_e which is defined here as the width of the $f(Q^2_e) = (Q^2_e - Q^2_{gen})/Q^2_{gen}$ distribution, where Q^2_{gen} is the generated value (cf. figure 9.6). The σ value is obtained by a fit to the $f(Q^2_e)$ distribution using a gaussian and a small constant term (cf. figure 9.6 (b)) to account for the tails. Figure 9.6 (a) shows the mean and σ of the gaussian for DIS MEPS events, selected by applying all cuts to the generated quantities. They are divided into five bins in Q^2_{gen}, with the bin boundaries given in table 9.2. Given this binning the (2+1)-jet cross section per bin (cf. table 7.1) is similar for the two samples, leading to comparable statistical accuracy. This binning will be used throughout. The points are plotted at the center of the Q^2_{gen} bins

	BIN 1	BIN 2	BIN 3	BIN 4	BIN 5
boundaries $[GeV^2]$	10-18	18-30	30-100	100-400	400-4000
mean $[GeV^2]$	13.5	23.0	45.1	234	857

Table 9.2: *The Q^2 binning of the event selection.*

calculated on a linear scale. Figure 9.6 (b) shows as an example the $f(Q^2_e)$ distribution of the second bin. The mean is distributed around zero, showing that there is no significant shift, and the resolution is below 5 % for the whole Q^2_e range.

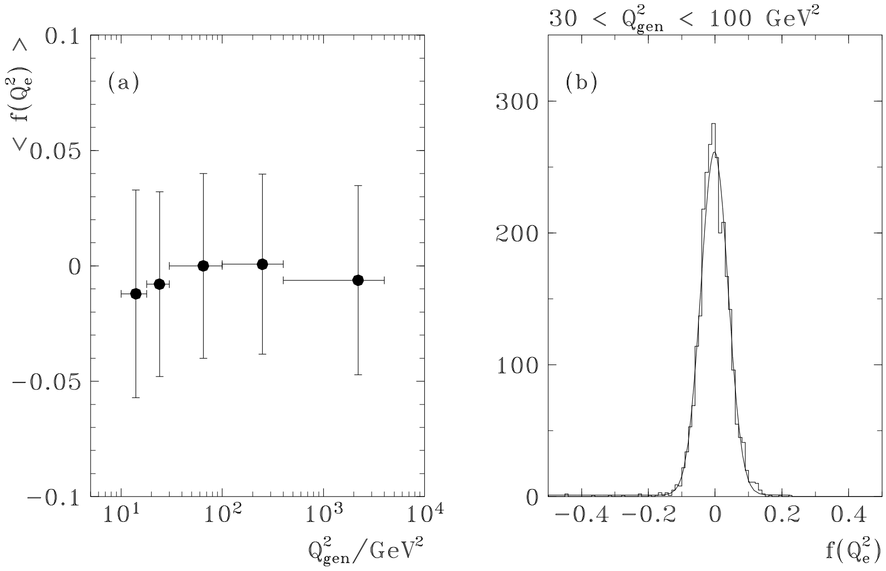

Figure 9.6: *The Q^2_e resolution, for definitions see text.*
(a) The mean value $< f(Q^2_e) >$ and σ (error bars) of the fit to $f(Q^2_e)$ as a function of Q^2_{gen}.
(b) The $f(Q^2_e)$ distribution for one of the bins of the BEMC sample together with the fit.

After having shown that the reconstruction of kinematic quantities works well, justification for the use of LEPTO61 for the resolution and efficiency study is given by showing the similarity of the distributions between LEPTO61 and the H1 data. Figures 9.7 and 9.8 show the electron spectra obtained from the H1 data compared to the prediction of the MEPS Monte Carlo. All these distributions are based on the reconstructed electron and are normalized to area unity, so enabling the shape of the distributions to be compared. The energy and angle are taken from the electron, y_e and Q_e^2 are derived from equation 3.10. The agreement between data and Monte Carlo is nice for both samples. The measurement will be compared to a parton level Monte Carlo PROJET, consequently also the distributions derived from the generated electron are shown (cf. figure 9.9 and 9.10) comparing to the H1 data. The Monte Carlo distributions are based on the event selection using only the generated quantities. The bad y_e resolution for low y_e values [2] means that the peak at low y_e is smeared out. This is more pronounced in the BEMC sample, where it corresponds to electron energies close to the initial electron energy.

However the lower cutoff in y is, in this analysis, given by W^2 which relies mainly on the hadronic final state and not on the electron energy measurement. Therefore no lower cut on y_e is applied and this analysis is not affected by the bad resolution. This poor resolution is described to some degree by Monte Carlo, as can be seen from the figures 9.7 (c) and 9.8 (c).

This gives confidence that the event selection, based on reconstructed objects, can be performed with enough accuracy to compare to a parton model prediction.

[2] The y_e resolution is $\delta y_e = (1/y_e) \cdot (\delta E_e/E_e)$

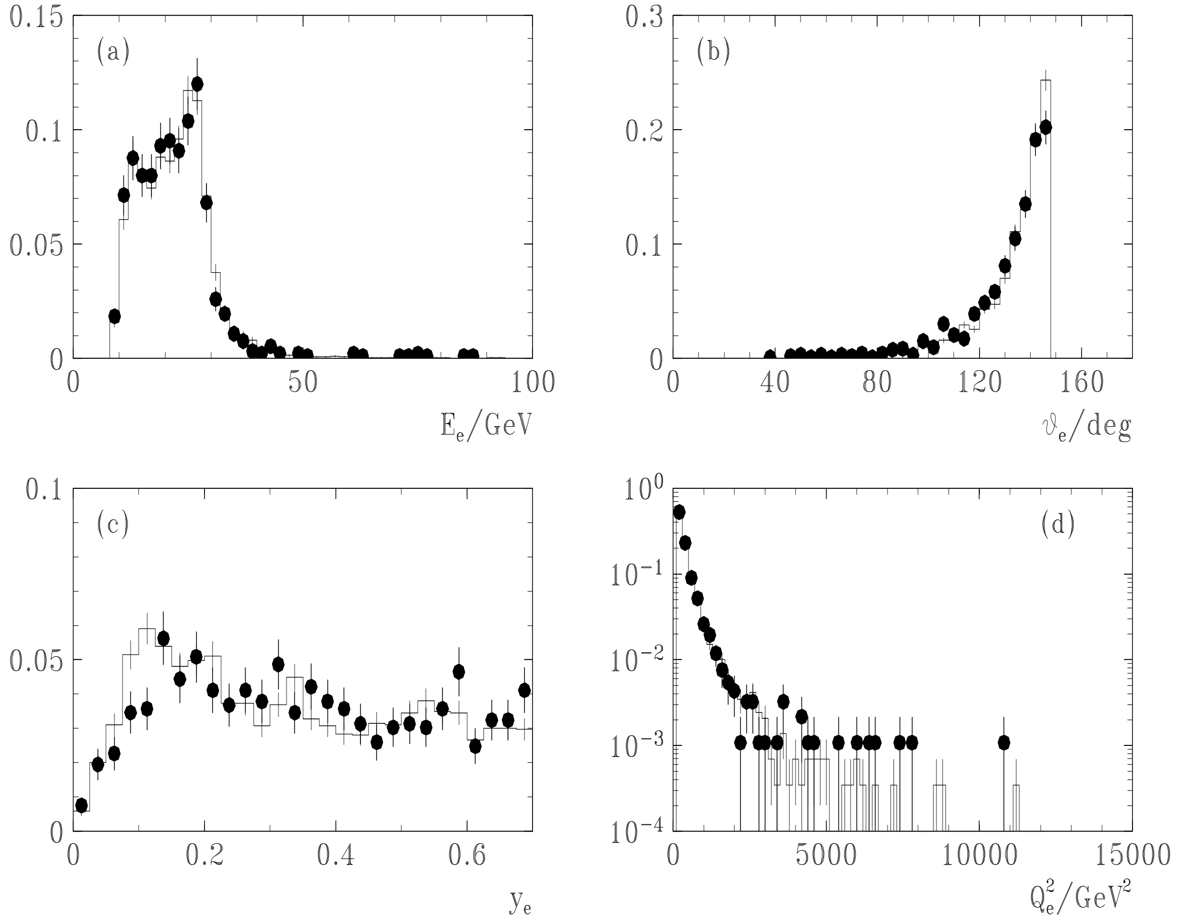

Figure 9.7: *LAr electron spectra compared to the MEPS model on the* **reconstructed** *level. The circles represent the H1 data and the histogram the MEPS prediction.*
(a,b) The measured electron energy and polar angle.
(c,d) y_e *and* Q_e^2.

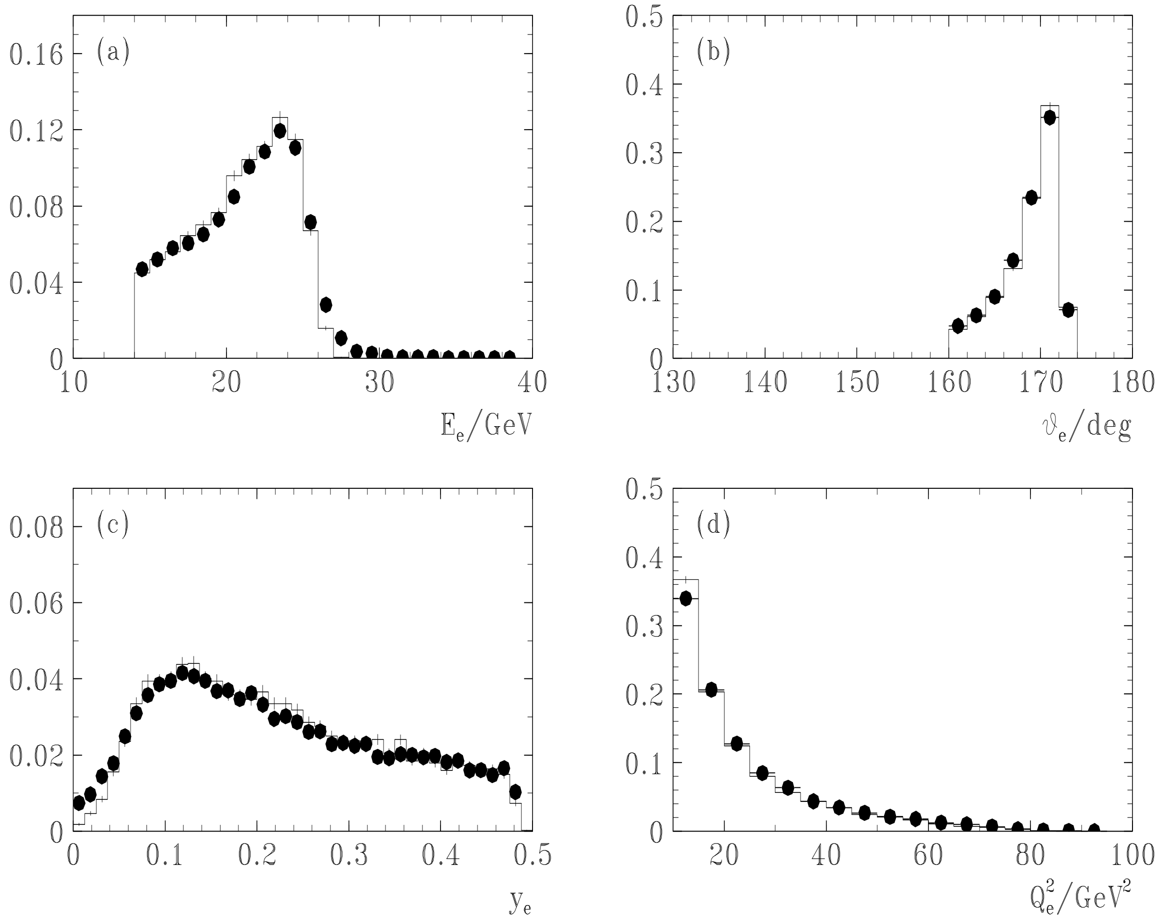

Figure 9.8: *BEMC electron spectra compared to the MEPS model on the* **reconstructed** *level. The circles represent the H1 data and the histogram the MEPS prediction.*
(a,b) The measured electron energy and polar angle.
(c,d) y_e and Q_e^2.

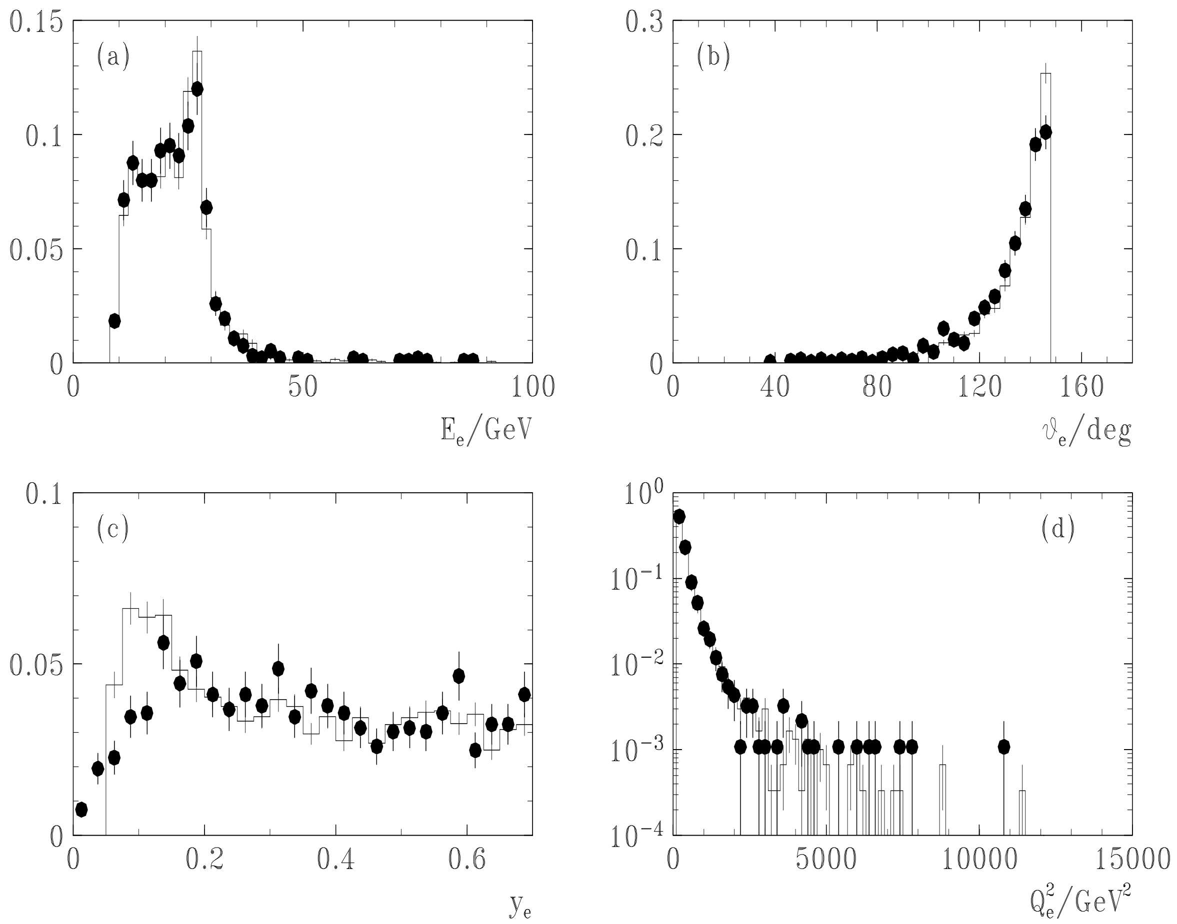

Figure 9.9: *LAr electron spectra compared to the MEPS model on the* **generated** *level. The circles represent the H1 data and the histogram the MEPS prediction.*
(a,b) The electron energy and polar angle.
(c,d) y_e *and* Q_e^2.

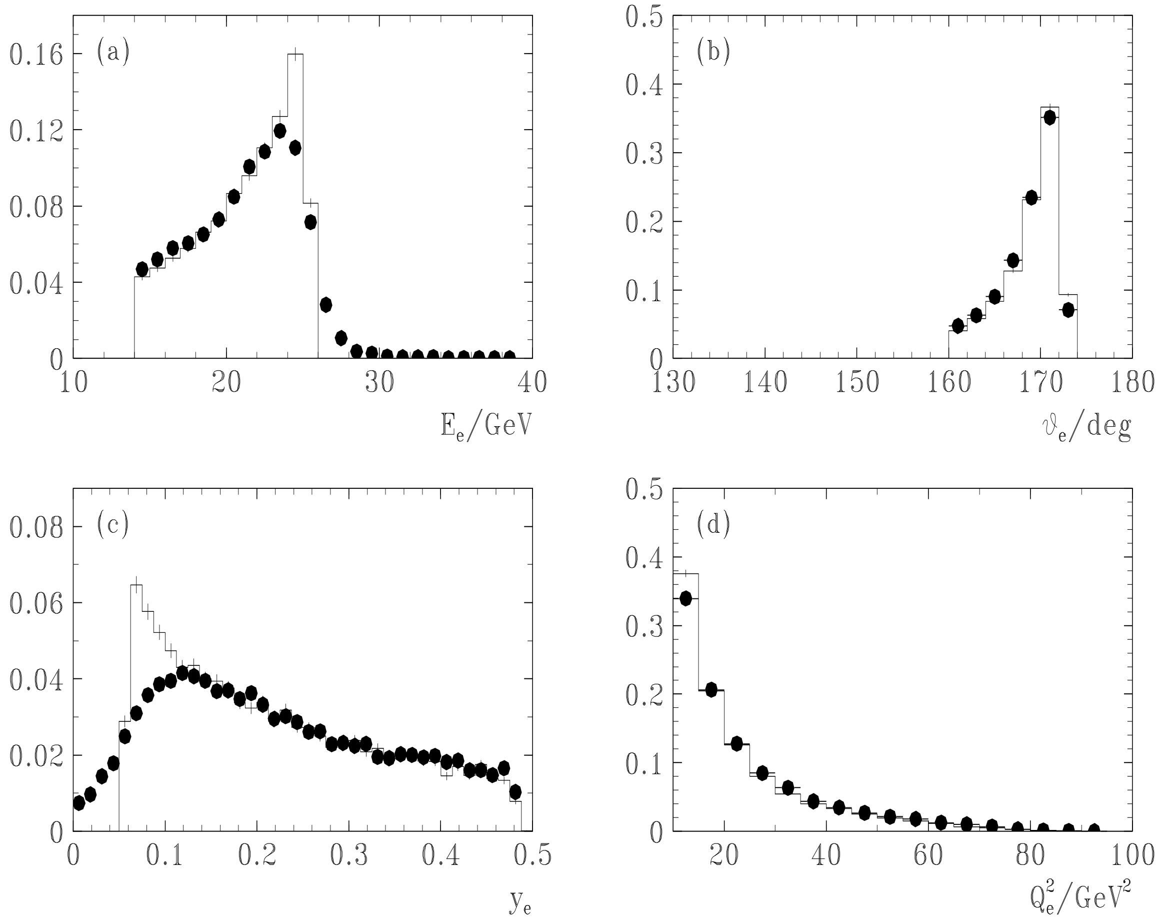

Figure 9.10: *BEMC electron spectra compared to the MEPS model on the* **generated** *level. The circles represent the H1 data and the histogram the MEPS prediction.*
(a,b) The electron energy and polar angle.
(c,d) y_e *and* Q_e^2*.*

Chapter 10

Jet rate determination and uncertainties

Here the jet definition chosen for this analysis, and also the tools to suppress the parton showers are discussed. Details of the pseudo particle approach are given, followed by a discussion of the y_c resolution and the jet reconstruction quality in terms of $p^{\star}_{t,jet}$ and ϑ_{jet} resolutions. The results of the above studies are used to demonstrate that the observed jet rates can be corrected to the parton level using LEPTO61. This is required to confront PROJET with the H1 data. Finally uncertainties and alternatives to the choices made are investigated.

Three different levels of the event evolution (cf. section 7) are considered. On all these levels the jet properties are studied, to be specific:

- The **parton level** denotes all outgoing partons after the evolution of ISPS and/or FSPS including the remnant. This is the QCD prediction, to the best knowledge of an event generator.
- The **hadron level** is defined as all final state stable particles [1] excluding neutrinos, that means a model of a full acceptance and infinite resolution detector.
- The **detector level** denotes reconstructed objects. Different to the first two levels, which only exist for Monte Carlo generated events, this can be either H1 data or fully simulated and reconstructed Monte Carlo events.

10.1 jet rate determination

To get meaningful results when comparing a theoretical calculation on the parton level to jets seen in the H1 experiment, one has to define the jets at the detector level as similar as possible to the ones defined by the cross section calculation. The calculation is done in the framework of the JADE algorithm (cf. section 5.1). This requires the same procedure to be used for the data analysis, namely using the JADE algorithm including the remnant and taking W^2 as scale in the clustering procedure. The only choices left are

- which objects to use for clustering on the detector level (cf. section 10.4.1), either charged tracks, calorimetric clusters, cells or combinations of these objects

[1] Particles with $\tau > 8 \cdot 10^{-9}s$ are considered to be stable

- the recombination scheme in which clustering is performed (cf. section 10.4.2)
- the Lorentz frame
- how to calculate W^2 from the data

The aim of this decisions is to get the best correlation between the partonic jets and the jets on detector level, based on investigations with an event generator.

The jet definition made here is based on calorimetric clusters and a pseudo particle (cf. sections 4.2.1 and 10.3.1), which is included in the clustering as well. Clustering is performed in the JADE scheme in the laboratory system and W^2 is calculated as the invariant mass squared of the sum of all objects entering the JADE algorithm. Due to measurement problems the Plug calorimeter is excluded from the analysis, and the BEMC energy is rescaled by 1.6 to weight from the electromagnetic to the hadronic scale.

The impacts of various other possible choices are discussed in section 10.4. In addition the k_t algorithm (cf. sections 4.2.2 and 10.5) is considered, as the corresponding calculations are expected to be available in future [25].

10.2 The suppression of parton showers

The interest is to isolate the matrix element structure of DIS, or, in other words, the hard interactions calculable in perturbation theory. To do this soft and collinear interactions, modeled as PS in event generators, need to be eliminated.

The numerical importance of PS can be seen from figure 10.1, which shows jet rates, comparing the ME with the MEPS approach for the BEMC sample and running the jet algorithm on the parton level. Because this is the first of several jet rate plots it will be discussed in more detail. Shown is the relative number of (N+1)-jets as a function of the jet algorithm parameter y_c. Starting from the left hand side the rates are shown for increasing values of y_c. Increasing y_c means decreasing the resolution power and thereby the number of observed jets. If $y_c \equiv 1$ one ends up with a (0+1)-jet event, everything is clustered in one object. The rate which vanishes at the lowest y_c value is the one with the highest multiplicity. In this way of plotting the jet rates the errors of the points at different y_c values are correlated. An event which is classified as a (2+1)-jet, e.g. at $y_c = 0.001$, stays in the (2+1)-jet class until it flips to a (1+1)-jet at $y_{c,2+1\to1+1} \equiv y_{21} > 0.001$, and contributes to all points between. Using only one point at a particular y_c value, which will be done in this analysis, this correlation does not matter. For future high statistic studies of the y_c dependence of the jet rates it will be preferable to study the differential distributions (cf. section 6.2) instead. The errors are calculated as efficiency errors (cf. equation 9.1), where ϵ equals R_{N+1}. In all these jet rate plots the (1+1)-jet, (2+1)-jet, (3+1)-jet rate and the rate for > (3+1)-jets are shown.

In LEPTO the ME calculation is to $\mathcal{O}(\alpha_s)$, meaning at most a (2+1)-jet configuration is generated while using the ME option. The PS generates more partons by radiation and in turn higher jet multiplicities occur in the low y_c region. At $y_c > 0.01$ only (2+1)-jet and (1+1)-jet events are left but the number of (2+1)-jet events at $y_c = 0.02$ is considerably increased due to parton showers. To determine whether this is due to IS or FS parton showers figure 10.2 shows the jet rates separately for IS and FS and compares them to ME. This is questionable because in principle IS and FS should interfere, but it is used only as a hint to decide which part of the PS is more important. As expected, the FSPS, which is well tested in e^+e^- annihilations, does not modify the ME distribution significantly, it is found to reduce the jet rate for high

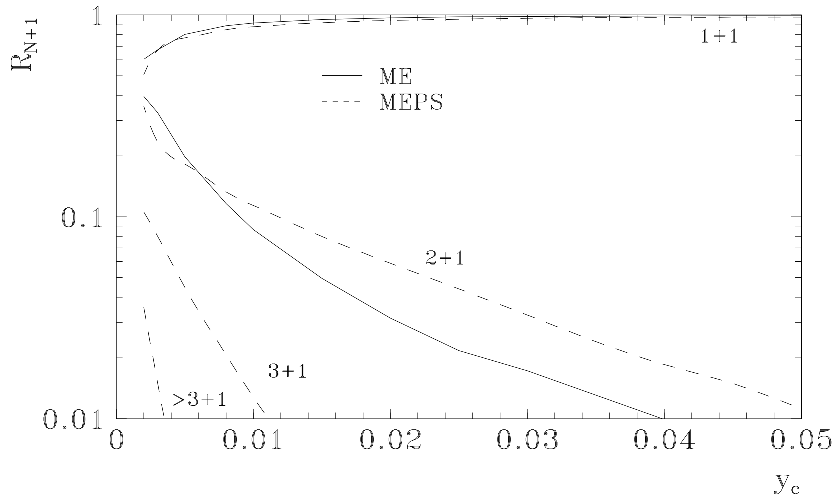

Figure 10.1: *Jet rates for the BEMC sample using ME and MEPS on the parton level for all jets. The used PDF is MRSD$^-$. For explanations see text.*

y_c. The big effect is mostly due to IS, where there is some freedom (cf. section 7.1.3) in the prescription because at HERA one has for the first time to face this problem. Comparing to the corresponding jet rates for the LAr sample (cf. figures 10.3 and 10.4) gives a handle to look for a x or Q^2 dependence of the PS. No dramatic change can be seen, the main features are the same. In the LAr sample and for higher Q^2 the (3+1)-jet events occur up to a somewhat higher y_c value and the additional (2+1)-jet rate at $y_c = 0.02$ due to IS is less pronounced, however, it is significantly above the ME prediction. Due to this it is necessary to reduce the events caused by PS in the whole kinematic range.

In the final state soft partons close to the hard outgoing partons occur. To avoid seeing them as separate jets a minimum jet cut ($y_c > 0.02$) is chosen, which assures together with the W^2 cut that the invariant mass squared of any 2-jet system is bigger than 100 GeV^2. At this y_c value all higher jet rates have vanished.

In the initial state these interactions are expected to generate partons parallel and/or with low p_t to the incoming proton. The resulting jets can be reduced by making angular cuts in the laboratory system, and a transverse momentum cut in the photon proton center of mass system. Another reason for making angular cuts in the laboratory system is to contain the entire jet in the sensitive detector volume to get a correct estimate of the jet four vector which is needed to impose further jet cuts (see below).

Figure 10.5 (a) and figure 10.6 (a) show the inclusive ϑ_{jet} and the $p^\star_{t,jet}$ distribution for the (2+1)-jet events on the parton level for ME and MEPS in the BEMC sample, at $y_c = 0.02$, without applying any additional cut. One observes jets with rather high $p^\star_{t,jet}$ which have small polar angles. The corresponding figures 10.7 (a) and 10.8 (a) for the LAr sample look similar. Inspecting these distributions lead to the following cuts.

- $10° \leq \vartheta_{jet} \leq 160°$ in the laboratory system for each jet.

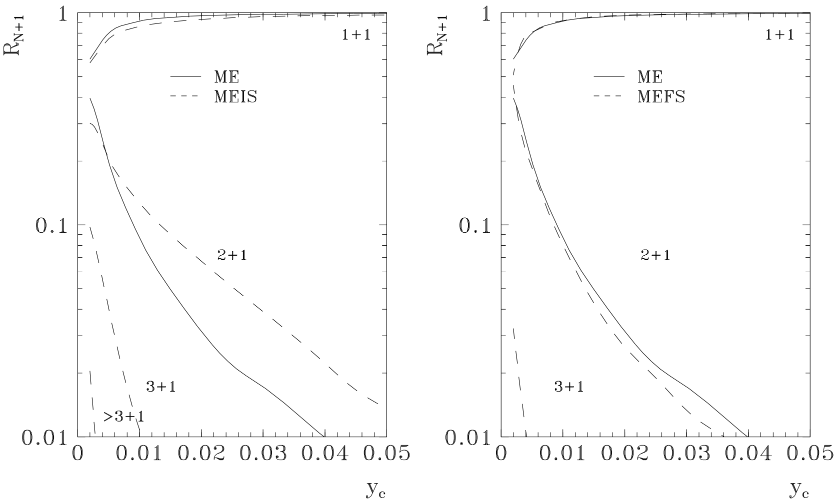

Figure 10.2: *Comparison of the jet rates for ME to the ones with ISPS and FSPS for all jets using the BEMC sample. The used PDF is MRSD$^-$. For explanations see text.*

- $p^{\star}_{t,jet} > 5.0\ GeV$ in the photon proton center of mass system for the hard jets events with (2+1)-jets .

The success of these cuts is demonstrated in the figure 10.6 (b-d) which shows the same comparison when applying the cuts, separately (b, c) and together (d). It is seen that the PS is reduced to a large extend, with the ϑ_{jet} cut being the more effective one. For low momentum transfer $Q^2 \approx 10\ GeV^2$, and thereby $Q \approx 3\ GeV$, the $p^{\star}_{t,jet} > 5.0\ GeV$ cut introduces at least one hard scale which is needed to apply perturbation theory. This is a reasonable choice, in the limit of photoproduction the ${p^{\star}_{t,jet}}^2$ scale even replaces the Q^2 scale.

One can not expect to suppress all the PS because in the LEPTO61 framework PS are used also for hard emissions in a region where the application is questionable (cf. section 7.1.2) and the emissions can be described already in the matrix element approach of PROJET. Because PROJET is a NLO Monte Carlo it contains the $\mathcal{O}(\alpha_s^2)$ terms which in the LEPTO approach are partly taken into account in the first term of the leading log approximation of PS. From this it follows that there is no need to get rid of all the PS. Therefore, this investigation does not give a quantitative result of how far the higher order effects are reduced, because the PS description of LEPTO61 needs not to be totally correct (see below) and the borderline between ME and PS is not sharp. But choosing these cuts gives certainly more weight to the matrix element contribution.

In section 11.2 it will be demonstrated that using these cuts the jet rates in the framework of LEPTO give a fair description of the H1 data.

As discussed in section 7.1.2 the scale of maximum virtuality in the initial state parton shower, which governs the amount of radiation, is somewhat arbitrary. Figure 10.9 demonstrates the numerical effect by showing the jet rates on the parton level while varying the scale within reasonable limits. Using the lower scale gives results close to the pure ME approach whereas

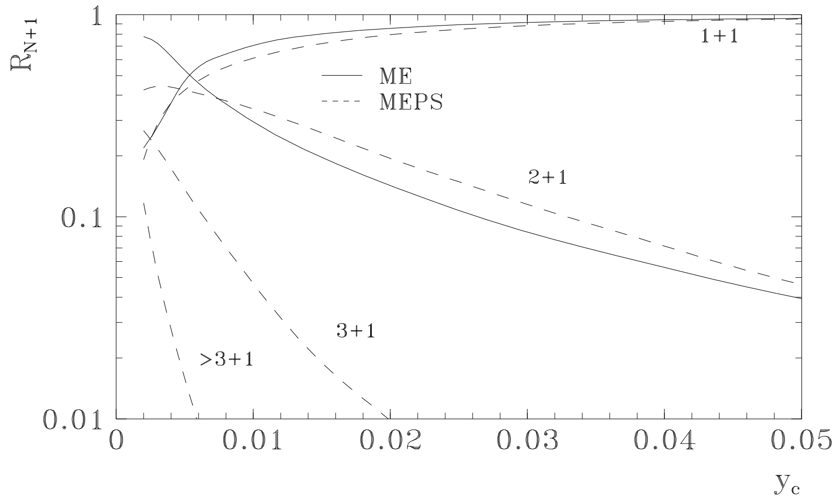

Figure 10.3: *Jet rates for the LAr sample using ME and MEPS on the parton level for all jets. The used PDF is MRSD$^-$. For explanations see text.*

choosing the upper scale (cf. section 7.1.3) gives a large number of additional jets. The jet rate changes from 5.5 % to 9%, at $y_c = 0.02$, by using the extreme choices. This gives another hint that the reduction of PS derived within the LEPTO61 PS description by applying the jet restrictions discussed above have not to be taken literally. The way one has to proceed is to restrict the freedom in this scale by comparing MEPS to HERA data, for example, by using the observed energy flow spectra. The actual default value used in LEPTO61 is the maximum scale.

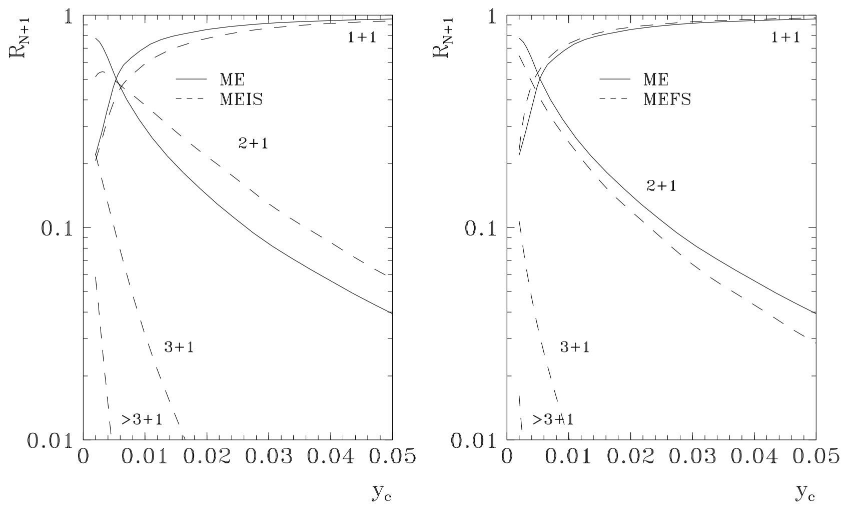

Figure 10.4: *Comparison of the jet rates for ME to the ones with ISPS and FSPS for all jets using the LAr sample. The used PDF is MRSD$^-$. For explanations see text.*

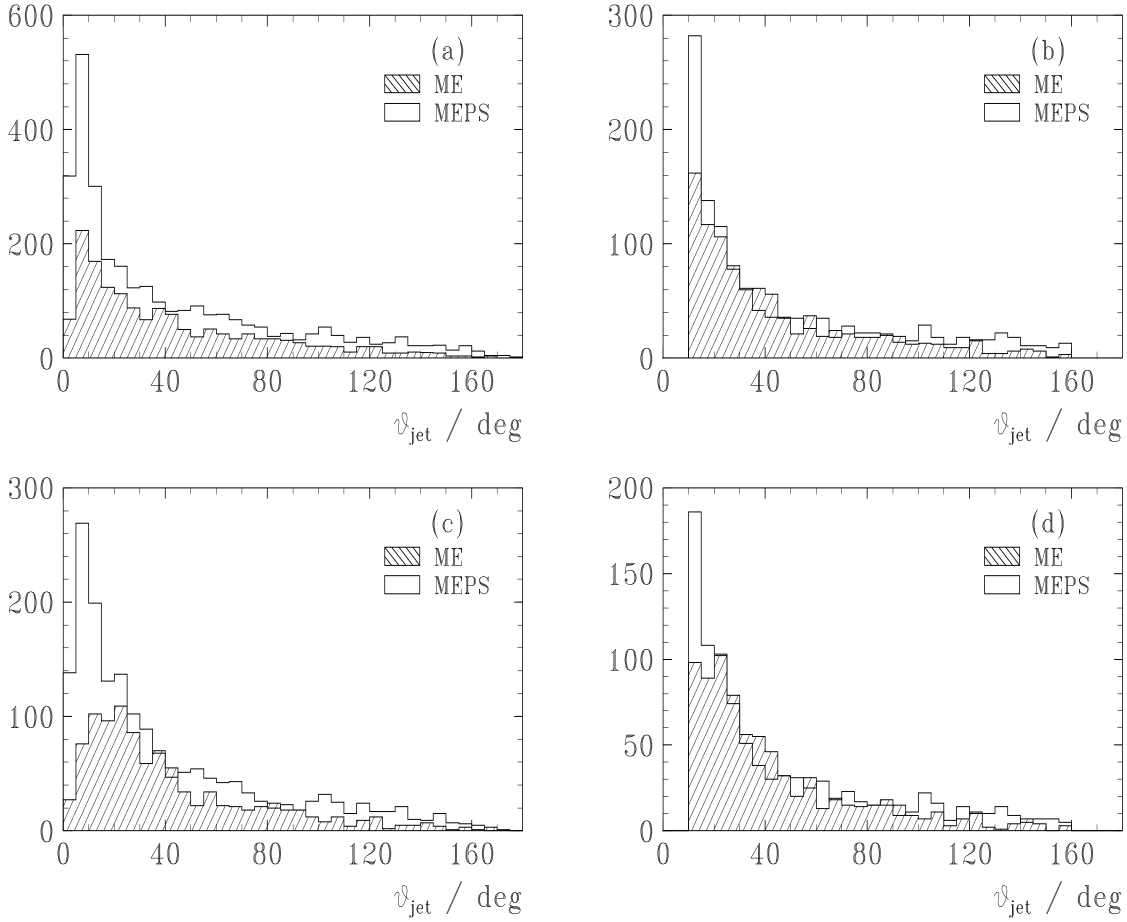

Figure 10.5: *Reduction of PS for the BEMC sample. Shown are the ϑ_{jet} spectra on parton level for MEPS (open histogram) and ME (hatched histogram) for various cut scenarios.*
(a) Without any cut. *(b) Applying only the ϑ_{jet} cut.*
(c) Applying only the $p^{\star}_{t,jet}$ cut. *(d) Applying both cuts.*

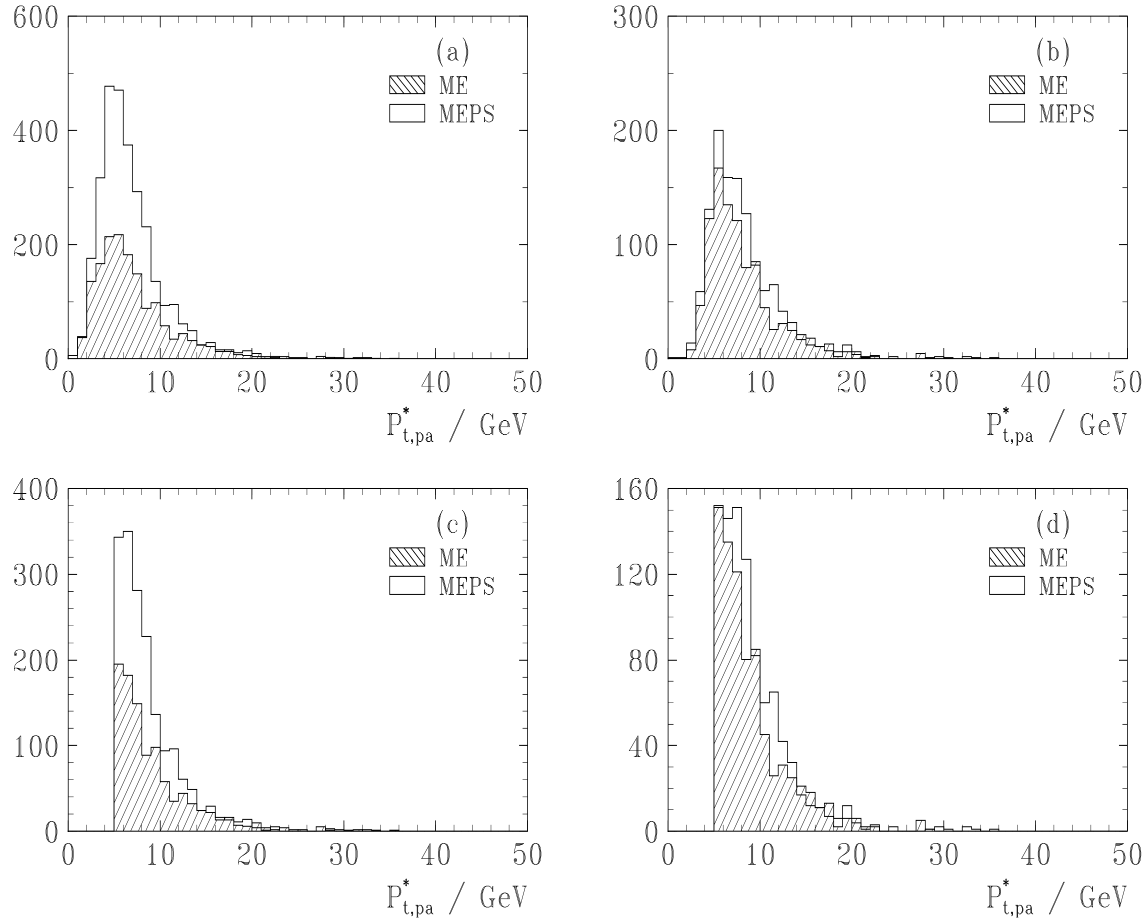

Figure 10.6: *Reduction of PS for the BEMC sample. Shown are the* $p^{\star}_{t,jet}$ *spectra. The definitions and ordering of a-d are as in figure 10.5.*

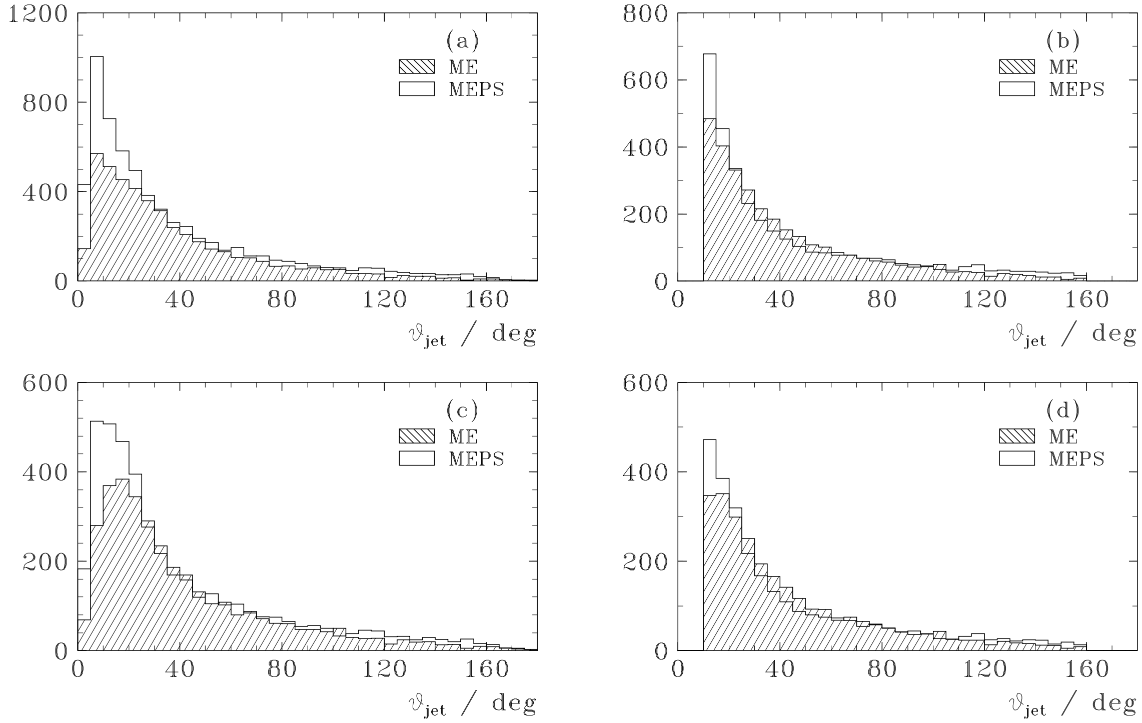

Figure 10.7: *Reduction of PS for the LAr sample. Shown are the ϑ_{jet} spectra. The definitions and ordering of a-d are as in figure 10.5.*

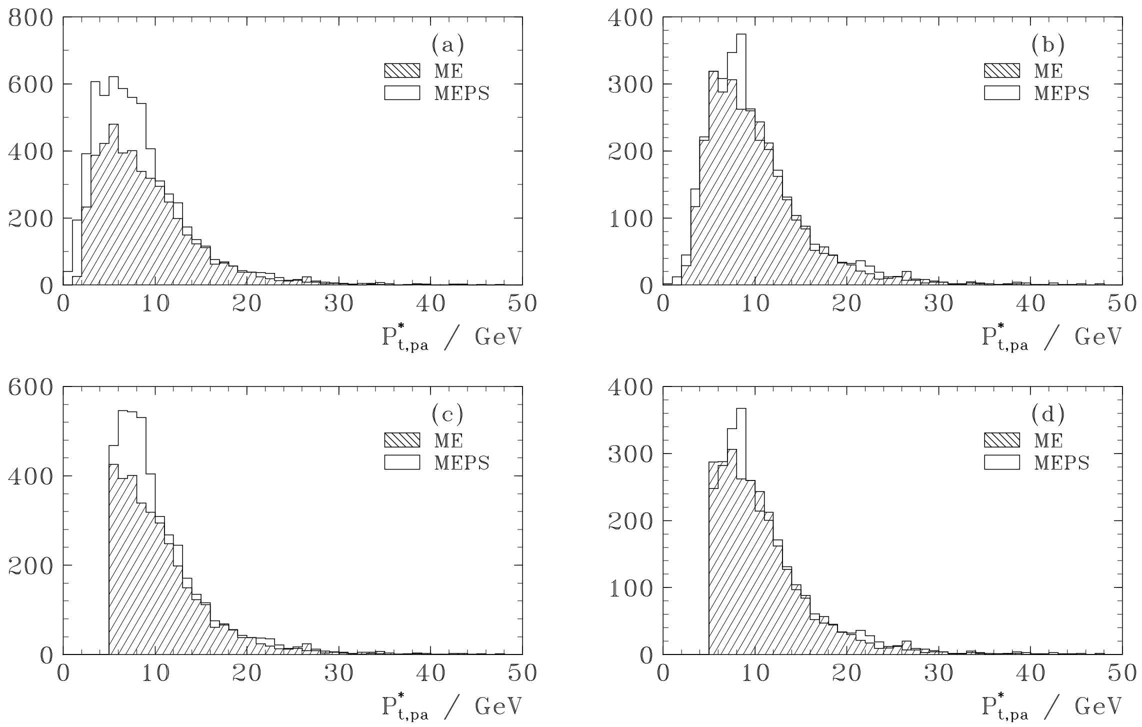

Figure 10.8: *Reduction of PS for the LAr sample. Shown are the $p^\star_{t,jet}$ spectra. The definitions and ordering of a-d are as in figure 10.5.*

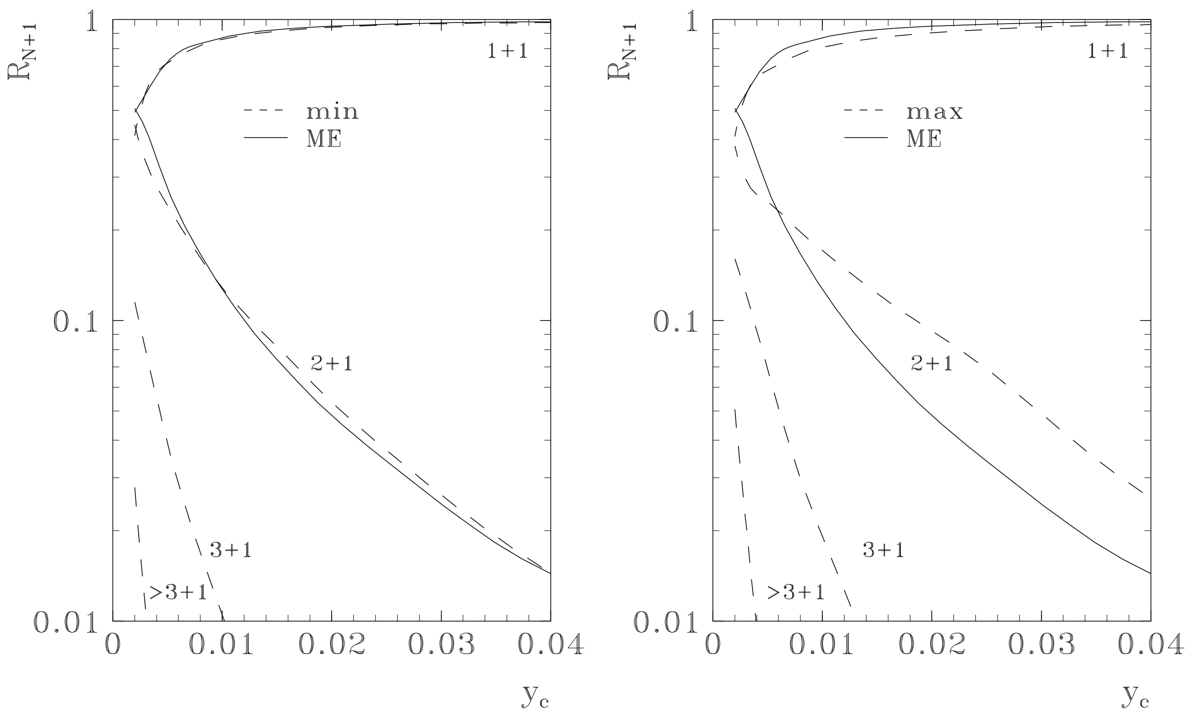

Figure 10.9: *The influence of the maximum virtuality scale in ISPS.*
Compared are the use of the minimum scale (a, left) and the maximum scale (b, right) to the pure ME case for the BEMC sample, using MRSD° as PDF without additional jet requirements.

10.3 jet reconstruction quality

10.3.1 The pseudo particle approach

As already discussed, the pseudo particle, which accounts for the unseen proton remnant, is included in the jet algorithm. The best estimate of the remnant four vector is given by the missing longitudinal momentum in the event. The missing momentum is calculated as

$$P_z^{miss} = p_{z\,p} + p_z - P_z^{vis} \tag{10.1}$$

where P_z^{vis} is the summed visible longitudinal momentum and $p_{z\,p}$ and p_z are the longitudinal momenta of the incoming proton and electron. Then, in addition to the measured objects, the pseudo-particle with the four momentum $(P_z^{miss}, 0, 0, P_z^{miss})$ is fed into the jet algorithm.

This is essential because on the matrix element level in PROJET it is checked whether any outgoing parton can be resolved from the remnant at y_c and the renormalization of the parton densities for IS partons parallel to the proton also uses this separation.

From four vector arithmetics it is seen that for calculating the pseudo particle vector no electron identification is needed, only the conservation of the longitudinal momentum is used. Giving also the missing transverse momentum to the pseudo particle makes it sensitive to the missing momentum of neutrinos induced by decays of for instance pions and kaons which should be avoided. A remnant carrying a significant transverse momentum is also in contradiction to the spectator model role of the proton remnant. According to this model, besides the intrinsic transverse momentum of the constituents, the proton remnant should not have any significant transverse momentum.

Including the pseudo particle has several advantages in the jet reconstruction.

- The particles produced between the remnant and the hard partons use energy of both and consequently partly 'belong' to the remnant. If they are closer in m_{ij}^2 to the remnant they will be clustered to it.

- The separation of the hard partons with respect to the remnant will be treated correctly that means equal to the theoretical prescription. Here one does not aim for the highest possible resolution power in the hard subsystems, but for a description as close as possible to the theoretical jet definition.

- Including the remnant gives the correct W^2 value, up to reconstruction errors, and it improves dramatically the correlation between the jets on parton level and on reconstructed level.

The success of this approach can be seen from figure 10.10 which shows the jet rates on the parton level and the detector level with and without using the pseudo particle, for the BEMC sample and without additional jet requirements. Using the pseudo particle approach, the correspondence of the jet rates on detector level and parton level is good for $y_c > 0.02$, which is not the case for the attempts without using the pseudo particle. For the jet reconstruction without using the pseudo particle, two approaches concerning the scale in m_{ij}^2 are investigated. In (a) the scale is taken as the invariant mass of the measured objects. This scale is much lower than W^2, which rules the jet rates on parton level, because the partons level is defined as all partons including the remnant. In figure 10.10 (b) W^2 is calculated from the double angle method. This scale is too large compared to the mass of the measured part of the hadronic final state leading to a shift in the jet rates and a large (0+1)-jet rate even for $y_c \ll 1$.

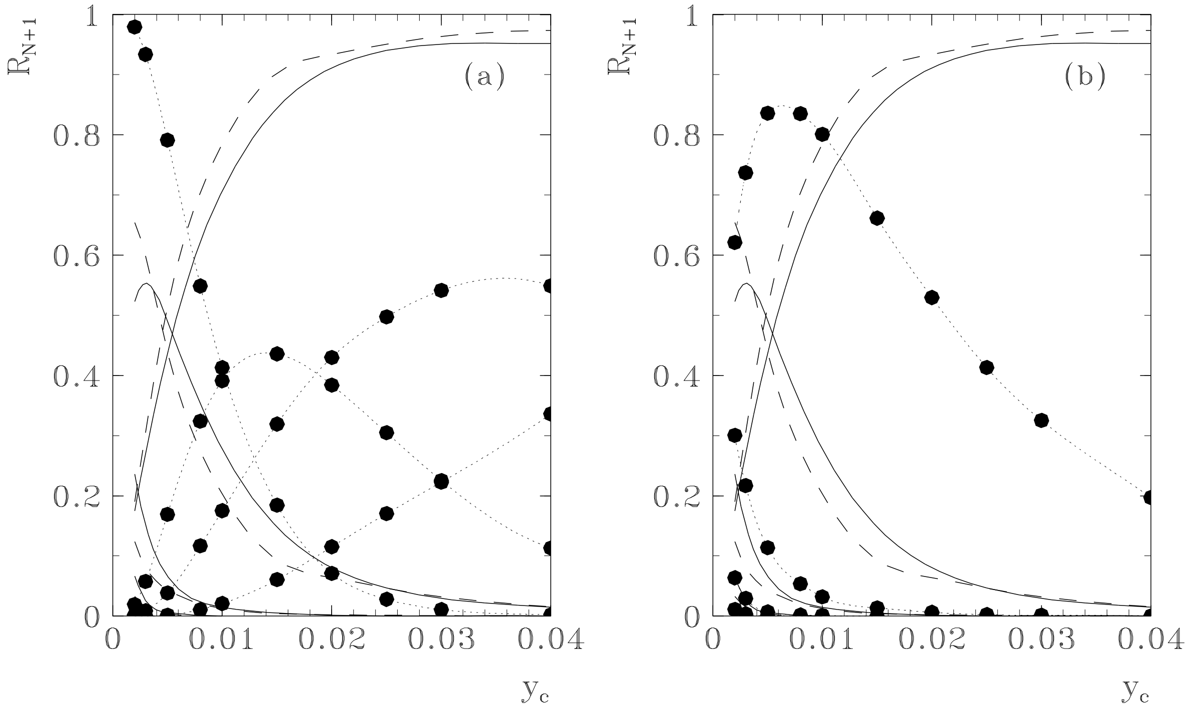

Figure 10.10: *The impact of the pseudo particle approach using the BEMC sample. Shown are the jet rates on detector level (full lines) and on parton level (dashed lines) using the standard procedure (cf. section 10.1). As usual the (1+1)-jet, (2+1)-jet, (3+1)-jet rate and the fraction of events with more than (3+1)-jets are displayed. Two different approaches* **without** *using the pseudo particle shown as dotted lines with the symbols on top are compared to that. The errors are smaller than the symbol size. Due to the bad performance of the jet algorithm without the pseudo particle there is a significant (0+1)-jet rate which accounts for the remaining fraction of events up to unity, however is not shown. It is easy to relate the various lines to the corresponding jet rates if one looks at the high y_c end, here the highest line has the lowest jet multiplicity.*

(a) m_{ij}^2 *is scaled by the invariant mass of the seen objects* $m_{ij}^2 = y_c \cdot W_{vis}^2$.
The (1+1)-jet rate increases up to 55 % at $y_c = 0.04$ *where the (2+1)-jet rate is about 33 %, the (3+1)-jet rate 11 % and the contribution from higher jet rates is small.*

(b) m_{ij}^2 *is scaled by* W^2 *calculated from the double angle method* $m_{ij}^2 = y_c \cdot W^2$.
The (1+1)-jet rate decreases rapidly to 20 % at $y_c = 0.04$. *All higher jet rates are negligible.*

Due to W^2 being so large compared to the seen part everything is clustered in one object. As usual this rate is not shown, it accounts for the rest up to unity. This plot demonstrates that the jet rates on detector level, without using the pseudo particle, do not at all coincide with the jet rates of the underlying parton level, showing that the pseudo particle is necessary.

10.3.2 Jet migrations and y_c resolution

By using the pseudo particle not only does the inclusive rate coincide to a much better degree, because the off-diagonal elements of the correlation matrix are similar, but also the event by event correlation of observed jets on both levels increases dramatically.

For the BEMC sample without special jet requirements, the correlation matrix at $y_c = 0.02$ is

$$\begin{pmatrix} (1+1)-jet \\ (2+1)-jet \\ (3+1)-jet \end{pmatrix}_{det} = \frac{1}{100}\begin{pmatrix} 88.0 & 2.8 & 0.0 \\ 4.6 & 3.6 & 0.1 \\ 0.0 & 0.0 & 0.1 \end{pmatrix}\begin{pmatrix} (1+1)-jet \\ (2+1)-jet \\ (3+1)-jet \end{pmatrix}_{pa}$$

0.7 % are (0+1)-jet events on both levels. For the LAr sample one gets

$$\begin{pmatrix} (1+1)-jet \\ (2+1)-jet \\ (3+1)-jet \end{pmatrix}_{det} = \frac{1}{100}\begin{pmatrix} 76.0 & 6.6 & 0.2 \\ 5.7 & 10.4 & 0.3 \\ 0.1 & 0.3 & 0.2 \end{pmatrix}\begin{pmatrix} (1+1)-jet \\ (2+1)-jet \\ (3+1)-jet \end{pmatrix}_{pa}$$

In this approach the percentage of (2+1)-jet events on parton level, which remain (2+1)-jet on detector level, is 56% for the BEMC sample and 60% for the LAr sample, at $y_c = 0.02$. This is somewhat smaller than the values quoted by the LEP [48] experiments, but in the same order of magnitude. Events which are classified as (2+1)-jet at one level and as (1+1)-jet at the other and vice versa are expected because of resolution effects.

A (2+1)-parton state, for instance a BGF event, will show up as a (2+1)-jet event on the parton level if y_c is chosen sufficiently small. By increasing y_c it reaches y_{21} where it flips to a (1+1)-jet event. This means either one parton is clustered to the remnant or the hard subsystem is not resolved anymore. Looking at the same event on the detector level it will not flip at exactly the same y_c value due to several smearing effects, e.g. hadronization, detector acceptance, energy resolution, angular resolution and 'wrongly' assigned objects to the jets. One may regard y_{21} as a quantity which is measured with a certain resolution and shift, the jet migrations can be looked at as a simple consequence of this. Not having the same jet classification on both levels is the manifestation of the fact that there exist no (2+1)-jet or (1+1)-jet event as such, a jet configuration is simply a question of resolution in y_c. What one must aim for is a measurement of y_{21} with good resolution and no shift. In this quantity all detector effects are included. Following the described procedure figure 10.11 and 10.12 show the y_{21} resolution for all events fulfilling the event selection (cf. section 9.1). Shown is the correlation of y_{21} on the parton and detector level (a), the difference between both (b) and the difference for those events which have a y_{21} on the parton level in the range 0.015-0.025 (c). The y_{21} values are shown in a stepsize of 0.002. The events on the horizontal axis are those which fliped at $y_{21} < 10^{-3}$ on the detector level or are those which have never been a (2+1)-jet event, and vice versa for the vertical axis.

The distributions are not gaussian, however this is clear because the difference is bounded on the lower side and is folded by the steeply falling y_c distribution of the events. The resolution estimate, obtained by a gaussian fit in the region indicated by the curves, is in the order of

0.005 and the shifts are below 0.005. They are always negative as is expected if one measures with a certain resolution a quantity which has a steeply falling distribution. The resolution in (b) is dominated by the very soft non perturbative part at low y_c.

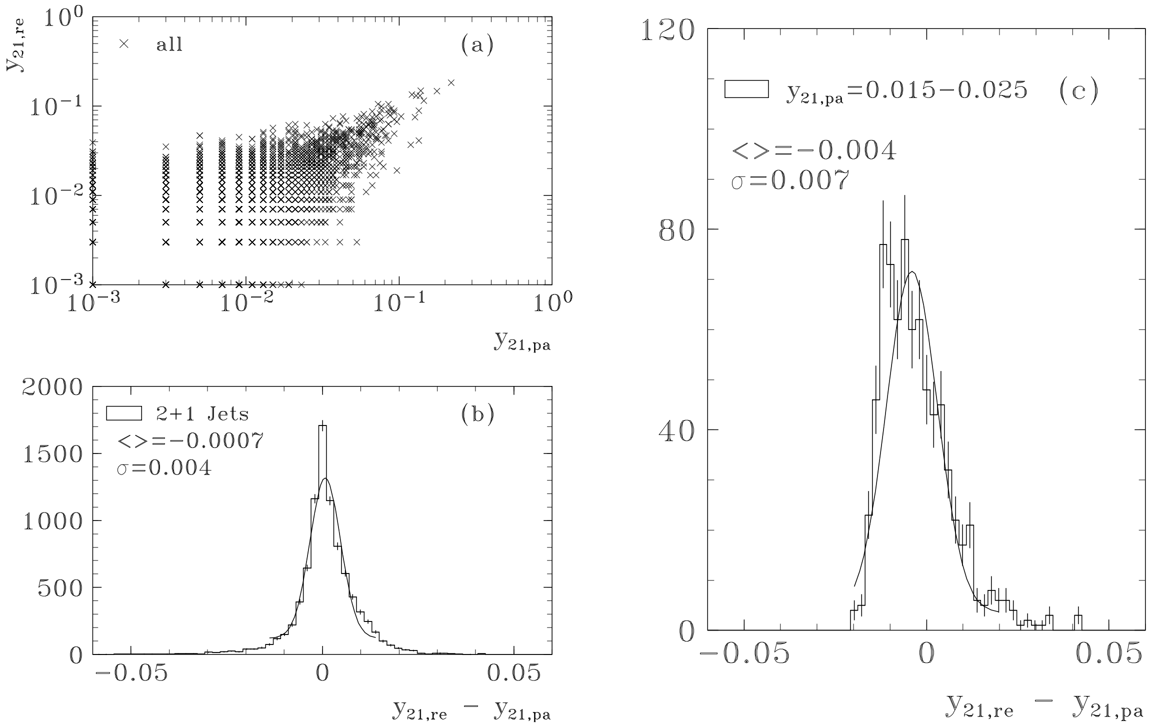

Figure 10.11: y_{21} *correlation for the BEMC sample. For explanations see text.*
- *(a)* *The correlation of the flip values on the parton level (pa) and the reconstructed detector level (re). The stepsize is 0.002.*
- *(b)* *The difference of both for all (2+1)-jet events.*
- *(c)* *The difference restricted to the region* $0.015 < y_{21,pa} < 0.025$.

10.3.3 Jet rate and jet four vectors

With all these ingredients the jet rates on the various levels can be inspected. Figure 10.13 shows the jet rates for LEPTO61 in the MEPS mode and using the PDF *MRSD°* on the parton, hadron and detector level, for both the BEMC and the LAr sample, without jet cuts. At low y_c the curves are quite different, this is due to the fact that one looks into the jets and splits them into parts. The more objects exists, the more likely this is, so usually one gets more jets the further the event has evolved from the parton level via the hadron level to the detector level. If $y_c \to 0$ the algorithm would resolve every single object. The lower the y_c the more the jet rates are affected by the fragmentation where those effects get important. At $y_c = 0.02$ the

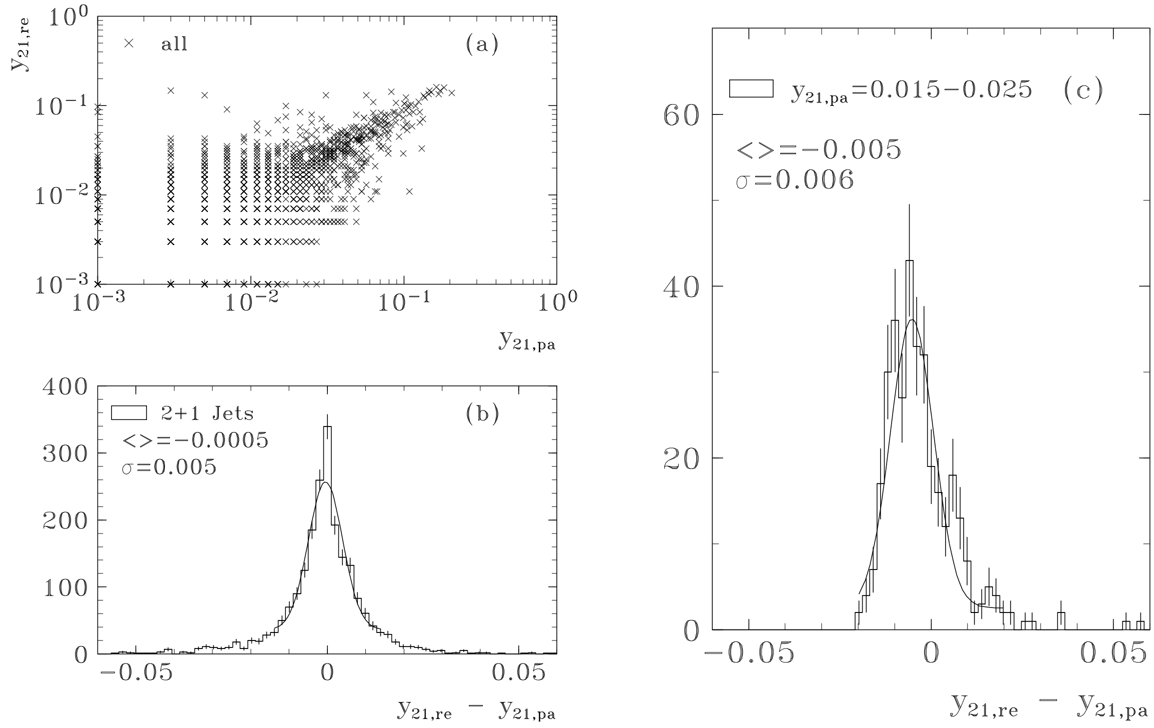

Figure 10.12: y_{21} *correlation for the LAr sample. For explanations see text.*
- *(a) The correlation of the flip values on the parton level (pa) and the reconstructed detector level (re). The stepsize is 0.002.*
- *(b) The difference of both for all (2+1)-jet events.*
- *(c) The difference restricted to the region* $0.015 < y_{21,pa} < 0.025$.

difference in rate between the various levels is nearly gone. In addition this improves with Q^2 as can be seen from the LAr sample, the jets get more energetic and thus more collimated.

The interest is not only to get the correct rates but also to estimate the correct jet four vector. To control the jet cuts one needs to know the resolution in the cut variables as well. The figures 10.14 and 10.15 show the resolution in ϑ_{jet} for both samples for $y_c = 0.02$, for those events which are (2+1)-jets on the parton and also on the detector level. The ambiguity of which detector jet one assigns to which parton jet is solved by taking that combination which gives the smaller sum of invariant masses. This is the natural choice for an algorithm which clusters in terms of invariant masses. In (a) the correlation of ϑ_{jet} is shown. The correlation is good but there are tails. The absolute resolution, shown in (b), is 5.4° and 3.4° for the BEMC sample and the LAr sample respectively. The shifts are −1.9° and −0.8°. These values are obtained by fitting a gaussian and a constant to the distributions of (b). The inclusive spectra are shown in (c), the agreement is almost perfect for $\vartheta_{jet} > 10°$. The $p^{\star}_{t,jet}$ resolution is seen in the figures 10.16 and 10.17 which show similar distributions as discussed before for the ϑ_{jet} resolution. In (a) the good correlation is demonstrated which leads to inclusive distributions

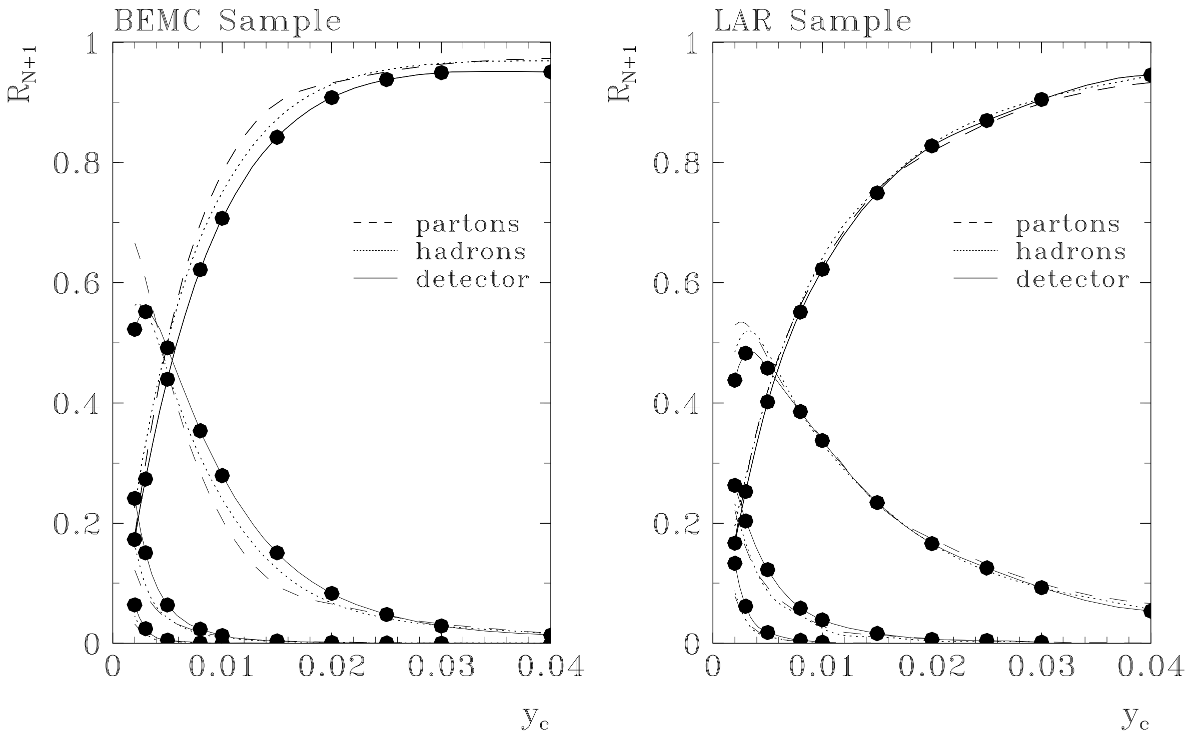

Figure 10.13: *Jet rates at various levels. The parton level (dashed lines), the hadron level (dotted lines) and detector level (full lines with points on top), are shown for both samples. For explanations see text.*
(a) The BEMC sample.
(b) The LAr sample.

(b), which agree well. The relative and absolute resolutions are shown in (c) and (d).

In summary it is seen that jet reconstruction improves with Q^2. This concerns the rate measurement and the resolutions in ϑ_{jet} and $p^{\star}_{t,jet}$. For $Q^2 > 100\ GeV^2$ the jets are measured with 18% $p^{\star}_{t,jet}$ resolution, 3.4° ϑ_{jet} resolution and a small shift of $-0.8°$.

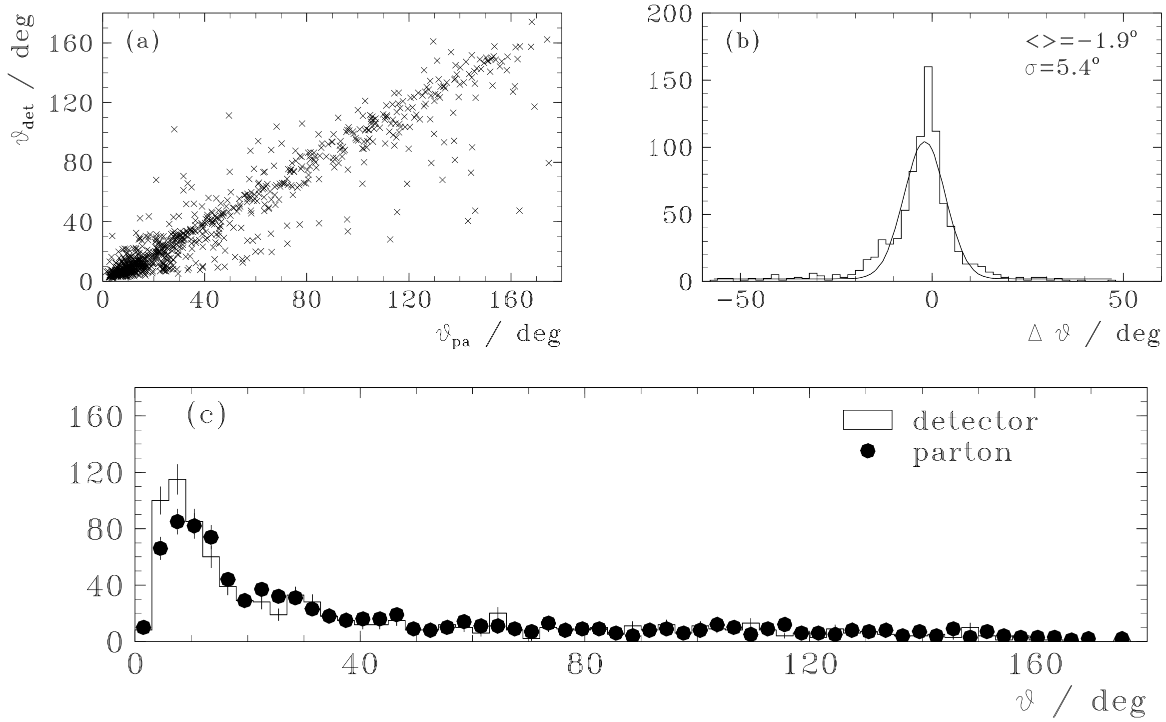

Figure 10.14: *ϑ_{jet} resolution for the BEMC sample using all events which are (2+1)-jets on both levels.*
(a) The ϑ_{jet} correlation between the parton level (pa) and detector level (det) jets.
(b) The difference $\Delta\vartheta = \vartheta_{det} - \vartheta_{pa}$, together with the fit (curve).
(c) The inclusive ϑ_{jet} spectra.

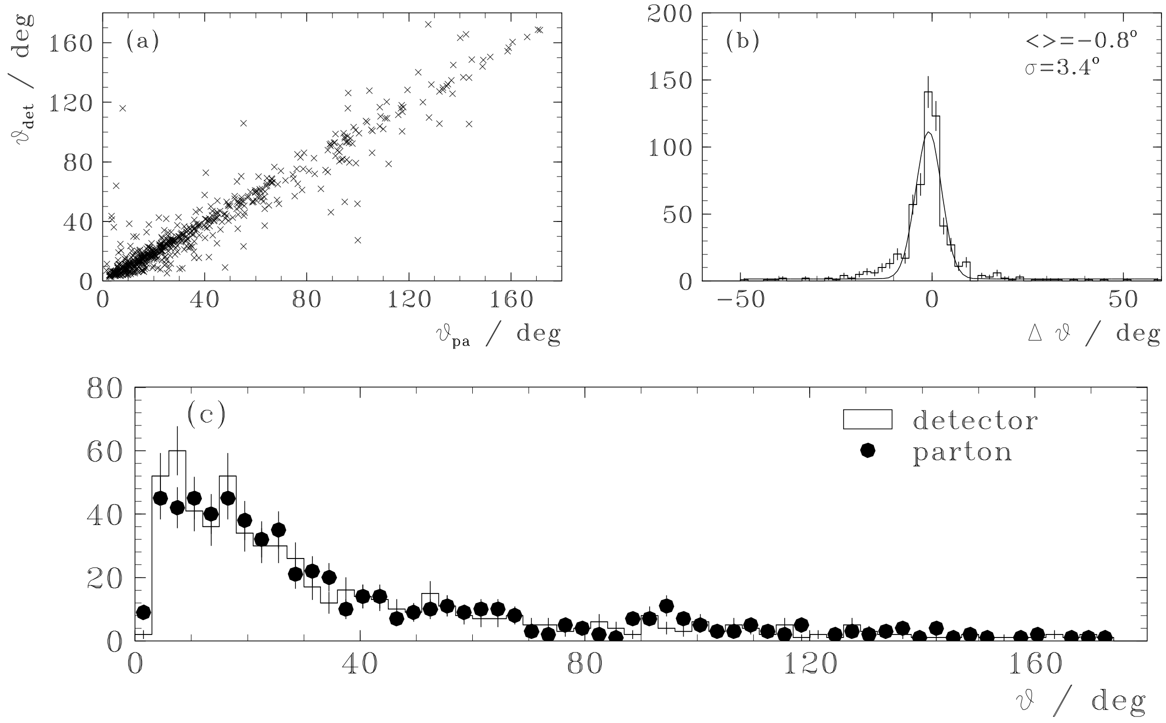

Figure 10.15: *ϑ_{jet} resolution for the LAr sample using all events which are (2+1)-jets on both levels. Ordering and definition of the figures are as in figure 10.14.*

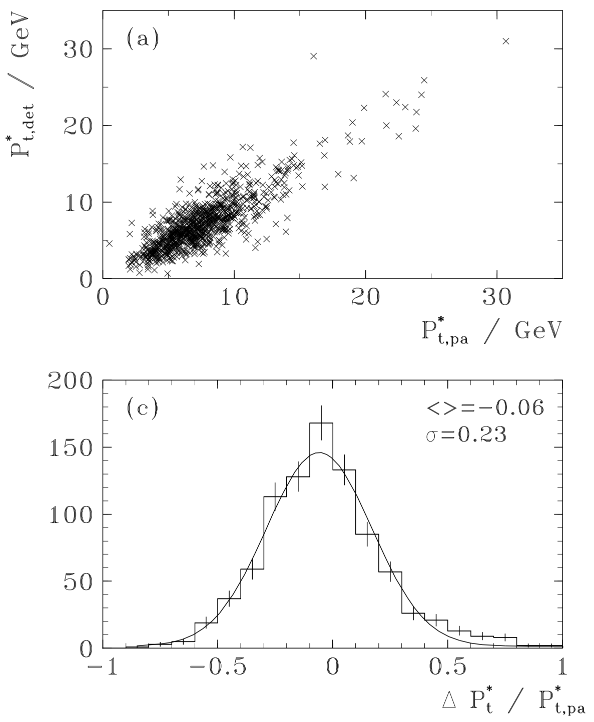

Figure 10.16: $p^\star_{t,jet}$ *resolution for the BEMC sample using all events which are (2+1)-jets on both levels.*
(a) The $p^\star_{t,jet}$ *correlation between the parton level (pa) and detector level (det) jets.*
(b) The inclusive $p^\star_{t,jet}$ *spectra.*
(c) The difference of both $\Delta p^\star_{t,jet} = p^\star_{t,det} - p^\star_{t,pa}$, *scaled by the value on parton level, together with the fit (curve).*
(d) The absolute difference of both in GeV, together with the fit (curve).

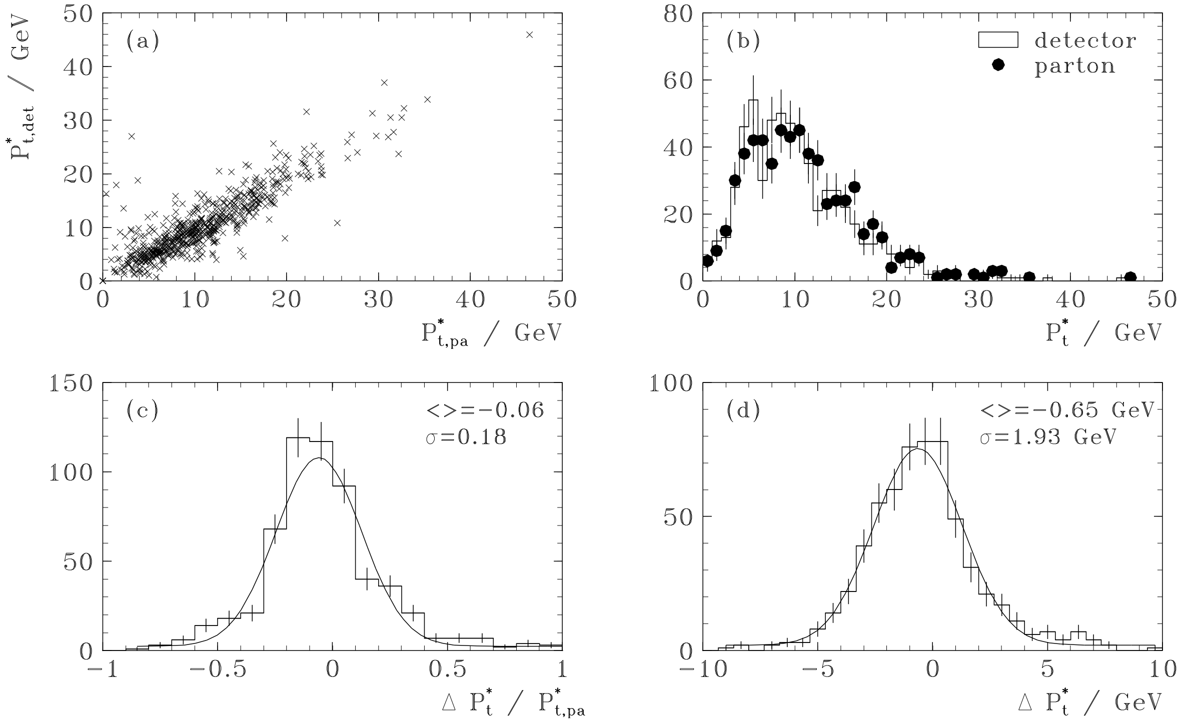

Figure 10.17: $p^\star_{t,jet}$ *resolution for the LAr sample using all events which are (2+1)-jets on both levels. Ordering and definition of the figures are as in figure 10.16.*

10.3.4 The correction to the parton level

The observed jet rate on detector level has to be converted to a jet rate on parton level in order to be able to compare to PROJET. To include the effects of the event selection and the jet reconstruction in one step the following procedure is applied.

The jet rate on parton level is defined by selecting the events as described in section 9.1 using only generated quantities and then performing the jet algorithm on parton level, with all phase space restrictions discussed in the last sections. This rate is then compared to the one obtained by using only reconstructed objects for the event selection and running the jet algorithm on detector level as described in section 10.1. The correction factor f is defined as

$$R_{2+1,pa}(Q^2, y_c) = f \cdot R_{2+1}(Q^2, y_c) \tag{10.2}$$

The measured jet rate in the experiment has to be multiplied with f to get the expected jet rate on parton level [2].

		Bin 1	Bin 2	Bin 3	Bin 4	Bin 5
$y_c = 0.02$		0.90 ± 0.06	1.10 ± 0.11	1.22 ± 0.12	1.16 ± 0.09	0.99 ± 0.09
	$p^\star_{t,jet} > 5\ GeV^2$	1.27 ± 0.13	1.42 ± 0.19	1.68 ± 0.23	1.27 ± 0.11	1.04 ± 0.10
	$\xi > 0.01$			1.71 ± 0.14	1.16 ± 0.09	1.03 ± 0.09
	$p^\star_{t,jet}$ and ξ			2.36 ± 0.29	1.26 ± 0.11	1.05 ± 0.10
$y_c = 0.03$		1.36 ± 0.18	1.59 ± 0.29	1.77 ± 0.32	1.19 ± 0.13	1.05 ± 0.12
	$p^\star_{t,jet} > 5\ GeV^2$	1.57 ± 0.23	1.82 ± 0.37	2.26 ± 0.48	1.31 ± 0.15	1.12 ± 0.14

Table 10.1: *Correction factors from the detector level to the parton level for two y_c values 0.02 and 0.03, and for various cut scenarios. The numbers are the correction factors f from equation 10.2. Making only the ϑ_{jet} cut leads to the values in line 1 and 4, if one applies in addition the $p^\star_{t,jet}$ cut one gets the values quoted in line 2 and 5. Line three shows the correction factors for applying the ϑ_{jet} cut and in addition a cut on ξ for the (1+1)-jet events.*

Table 10.1 shows the correction factors for various cut scenarios. The correction factors f are obtained in each bin in Q^2 and separately for each jet requirement, using MEPS with the *MRSD*$^-$ parton density. The $R_{2+1}(Q^2, y_c)$ values are based on fully simulated and reconstructed Monte Carlo events, with the statistics as quoted in table 9.1. The $R_{2+1,pa}(Q^2, y_c)$ values can be obtained from the generator alone, and are based on a statistics of 25000 events per bin after the event selection. The errors quoted of the correction factors (cf. table 10.1) are the statistical errors of the fully simulated and reconstructed events. Due to the lack of Monte Carlo statistics at present the errors are large.

The general behaviour is the following. The more additional features of the jets one requires the higher the correction factors get. The shifts in the cut quantities $p^\star_{t,jet}$ and ϑ_{jet} lead to a

[2] Note that here Q^2 is differently measured on the both sides of the equation. For $R_{2+1,pa}(Q^2, y_c)$ it is the generated one, whereas for $R_{2+1}(Q^2, y_c)$ it is reconstructed from the electron.

loss of events on the detector level compared to the parton level. For instance, if one cuts at $p^{\star}_{t,jet} > 5\ GeV$, due to the shift in the reconstructed $p^{\star}_{t,jet}$ (cf. section 10.3.3), one effectively cuts at a higher value, thereby loosing events. One can either correct for this by shifting the cut value according to the Monte Carlo studies, which would decrease the remaining correction factors, or by applying the correction factors directly. The second choice is taken here. The correction factors for the low Q^2 bins are much higher than the corrections for $Q^2 > 100\ GeV^2$ where the jet reconstruction works better, leading to correction factors in the order of unity. This correction takes into account everything which happenes from a generated parton jet to a seen detector jet, which may distort the measurement of the jet four vector. It does not correct for higher order effects, but only for hadronization and detector effects. Although MEPS is the favourite generator (cf. section 7) it would be helpful to evaluate the model dependence of the correction factors by using another QCD inspired model e.g. the CDM model. At the moment, due to the limited statistics available, this is not possible.

10.4 Jet rate determination uncertainties

10.4.1 Calorimetric cells versus calorimetric clusters

The choice of objects to cluster is quite obvious. The H1 tracking devices do not have full acceptance at the moment, due to technical problems. Therefore, tracks alone or combinations of tracks with calorimetric objects can not be used at the moment. The question is whether to choose calorimetric cell energy information or calorimetric energy clusters formed by the calorimetric pattern recognition which adds up several cells. The cells have the advantage of giving a higher granularity but also assignments of low energy objects to the wrong jet are more likely. A reason for using calorimetric clusters is the minimization of the used computer time per event. The number of possible pairs $(i,\ j)$ increase rapidly with the number of considered objects and so does the used CPU time. Figure 10.18 shows the jet rates by using either calorimetric clusters or cells. The differences are found to be marginal for all y_c. At $y_c = 0.02$ the deviation is smaller than the statistical precision which again is smaller than the size of the symbols. The choices are equally good and so the faster one is chosen.

10.4.2 Recombination scheme uncertainty

An interesting aspect is the sensitivity of jet rates to the recombination scheme in which the clustering is performed (cf. table 4.1). The schemes differ in the definition of m^2_{ij} and the choice of how to combine two objects $(i,\ j)$ into k (cf. table 4.1). The test quantity m^2_{ij} can be either the invariant mass of two objects $(i,\ j)$ or the approximate invariant mass neglecting the individual masses m^2_i, m^2_j.

On the matrix element level this is not important because the partons are massless and the calculations in PROJET are NLO and not NNLO, in consequence one combines at most four to three partons in the (2+1)-jet case and three to two partons in the (1+1)-jet case but never tries to combine an object which has got a mass by preceding combinations.

After parton showering the situation changes and a recombined object with mass $m^2_k > 0$ may be combined with another object. Obviously this gives a freedom which one can use either in the m^2_{ij} measure, as done in the JADE scheme or in the recombination procedure, where one either conserves energy (E0 scheme) or momentum (P and P0 scheme) in order to get the combined vector massless. The difference between P und P0 is that the later corrects for the

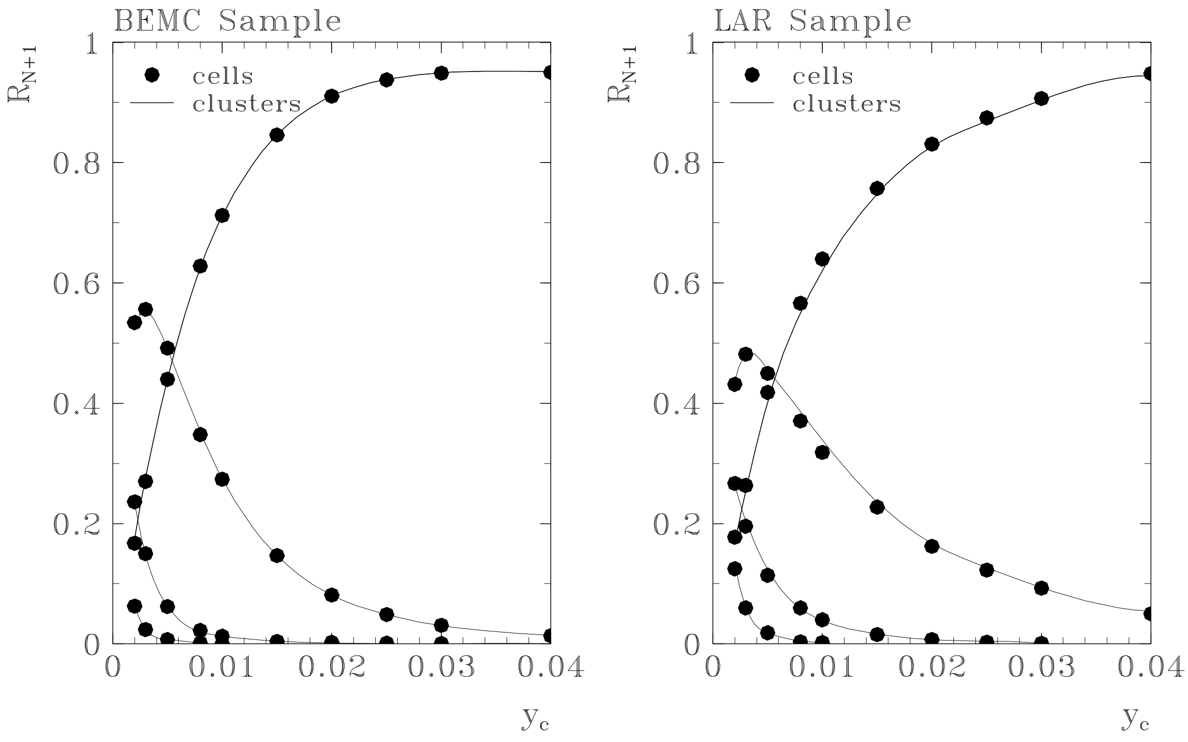

Figure 10.18: *jet reconstruction from calorimetric clusters versus cells. The jets obtained from cells are shown as symbols with error bars, which as usual are smaller than the symbol size, the one from calorimetric clusters as full line. Both samples, the BEMC (a, left) and the LAr sample (b, right), are considered.*

not conserved energy by updating the scale after each violation of energy conservation. These schemes are not Lorentz invariant. If one wants to keep the Lorentz invariance one uses the E scheme which conserves both energy and momentum to the cost of having massive objects.

Because the procedure is not fixed by the NLO calculation the scheme which gives the best correlation between parton level jets and detector level jets can be chosen. The figures 10.19 and 10.20 show the jet rates on parton and detector level for the various schemes discussed above, using MEPS with PDF $MRSD^-$, for all events fulfilling the event requirements defined in section 9.1. The differences between the P, E0 and JADE scheme are marginal, whereas the Lorentz invariant E scheme gives totally different jet rates on the parton and the detector level. Similar results were obtained by the LEP experiments [48]. The choice made here is to use the original JADE scheme.

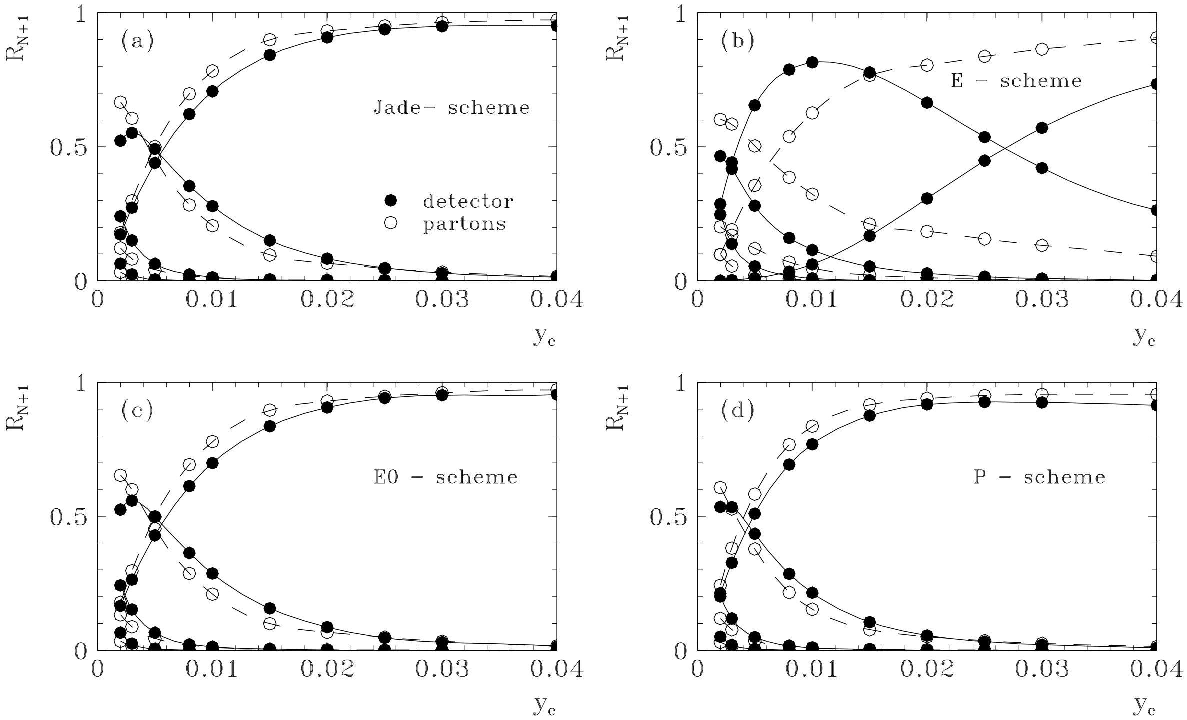

Figure 10.19: *Recombination scheme dependence for the BEMC sample. The figures a-d show the jet rates for various recombination schemes explained in table 4.1. The points are connected with lines to guide the eye. The full lines are the detector level the dashed ones the parton level.*

(a) The JADE recombination scheme.
(b) The E recombination scheme.
(c) The E0 recombination scheme.
(d) The P recombination scheme.

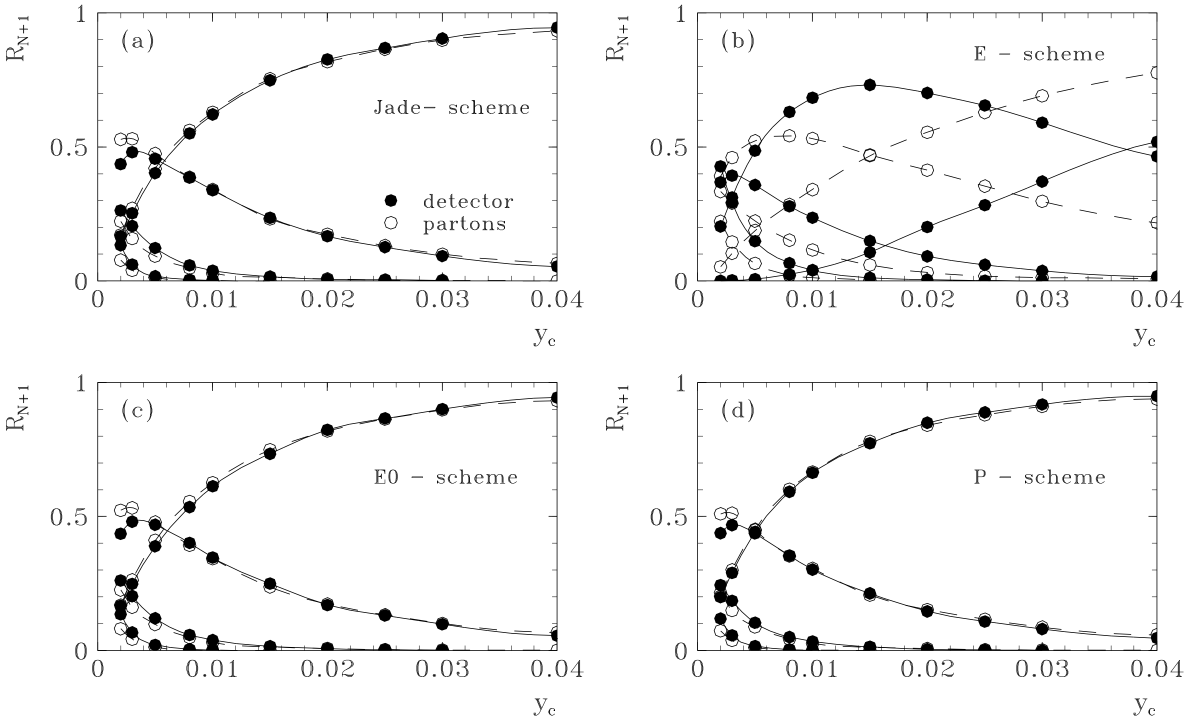

Figure 10.20: *Recombination scheme dependence for the LAr sample. Ordering and definition of the figures are as in figure 10.19.*

10.5 Confronting the k_t algorithm with DIS events

As already discussed in section 5.2 calculations in resummed techniques are expected to be performed for *ep* scattering. In this section, this is investigated from an experimental point of view to see if it is feasible to define jets in terms of the k_t algorithm. The procedure of the jet algorithm, which is applied here is taken from [24] and was discussed in section 4.2.2. The jet algorithm is studied for the two samples and using it in two reference frames, the laboratory frame and the Breit frame. According to [24] the E_t scale is defined in the order of Q^2, namely chosen is $Q^2/2$ in both frames.

The figures 10.21 and 10.22 show the result. In order to blow up the low y_c and high y_c region the same plot is shown twice, on a logarithmic scale (cf. figure 10.21) and on a linear scale (cf. figure 10.22). The general behaviour is that the Lorentz frame does not make too much difference. The performance is similar in both frames. The dependence on Q^2 however is strong. In the Lar sample the inclusive jet rates on detector and parton level agree quite well, the result in the Breit frame being a bit better in that respect. However, at low Q^2 the jet rates do not coincide on both levels, it is even hard to recognize the various contributions. The jet rate which has the highest fraction at $y_c \to 1$ is the one with the lowest multiplicity.

It is clear that for $Q^2 \approx 20\ GeV^2$ and $y_c = 0.05$ one uses k_t values of $0.25\ GeV$, which means the fragmentation region is probed. At $y_c = 1$ the relative transverse momentum of the hard subsystem, for instance in a BGF event, reaches $5\ GeV$. In general compared to invariant masses of $> 100\ GeV^2$, that are obtained when using the JADE algorithm at $W^2 > 5000\ GeV^2$ and $y_c = 0.02$, these values are rather small. In this way of using the k_t algorithm it is not useful for $Q^2 < 100\ GeV^2$, however in the LAr sample the performance looks good from an experimental point of view.

Using the k_t algorithm on the LAr sample gives encouraging results when comparing parton and detector level jets and the algorithm also gives a good description of the data. However, although it seems to be a feasible jet algorithm for $Q^2 > 100\ GeV^2$, from an experimental point of view, it can not test QCD unless theoretical calculations in NLO are available in the k_t algorithm. Therefore, here no attempt is made to tune the parameters to get a better performance of the k_t algorithm in the BEMC sample. However, other studies exist, for example a procedure to use the k_t algorithm by using a fixed scale is studied in [49].

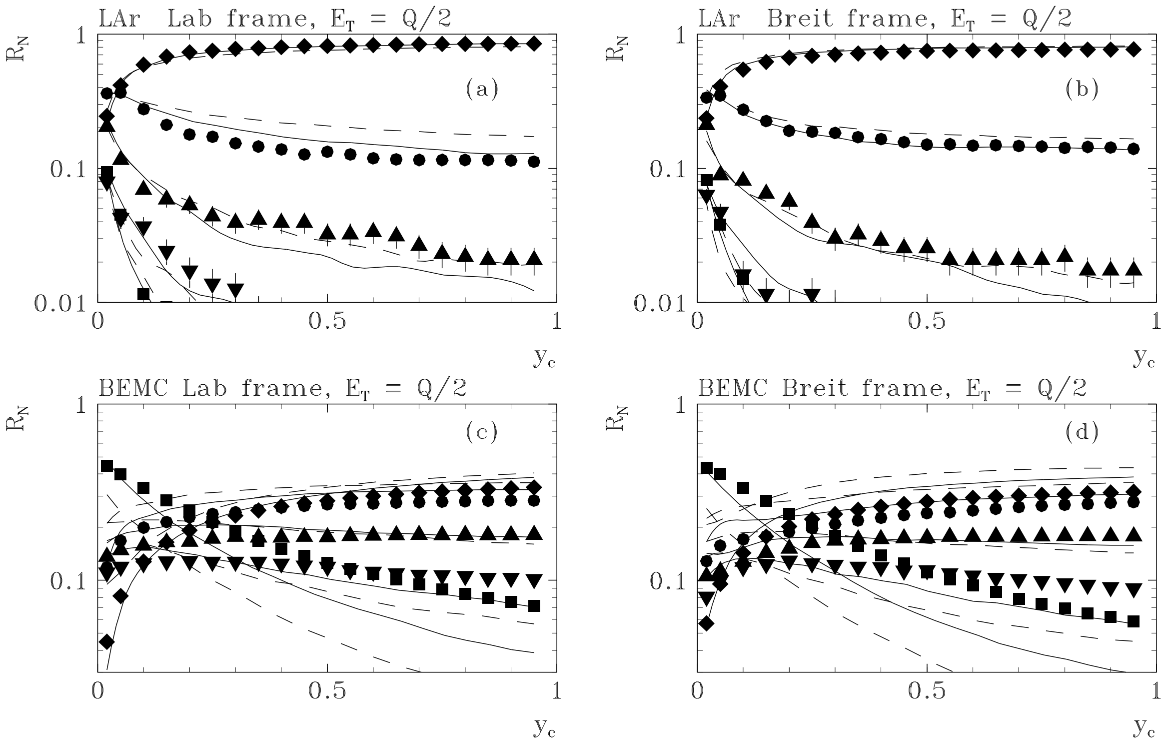

Figure 10.21: *k_t algorithm compared to H1 data on a logarithmic scale. The full lines represent the MEPS prediction on detector level, the dashed ones the parton level expectation. The points are the H1 data with the following notation. The one jet events are shown as rotated squares, the two jets as circles, the three jets as triangles, the four jets as upside down triangles and the rate of more than four jets as squares. The remnant is not counted in this scheme. The zero jet rate is small, the remaining fraction up to unity, and not shown.*
The two top figures contain the LAr sample results, the lower ones those of the BEMC sample. The scale is always defined as $E_t = Q/2$

(a) Lar sample with jet algorithm performed in the laboratory frame.
(b) Lar sample with jet algorithm performed in the Breit frame.
(c) BEMC sample with jet algorithm performed in the laboratory frame.
(d) BEMC sample with jet algorithm performed in the Breit frame.

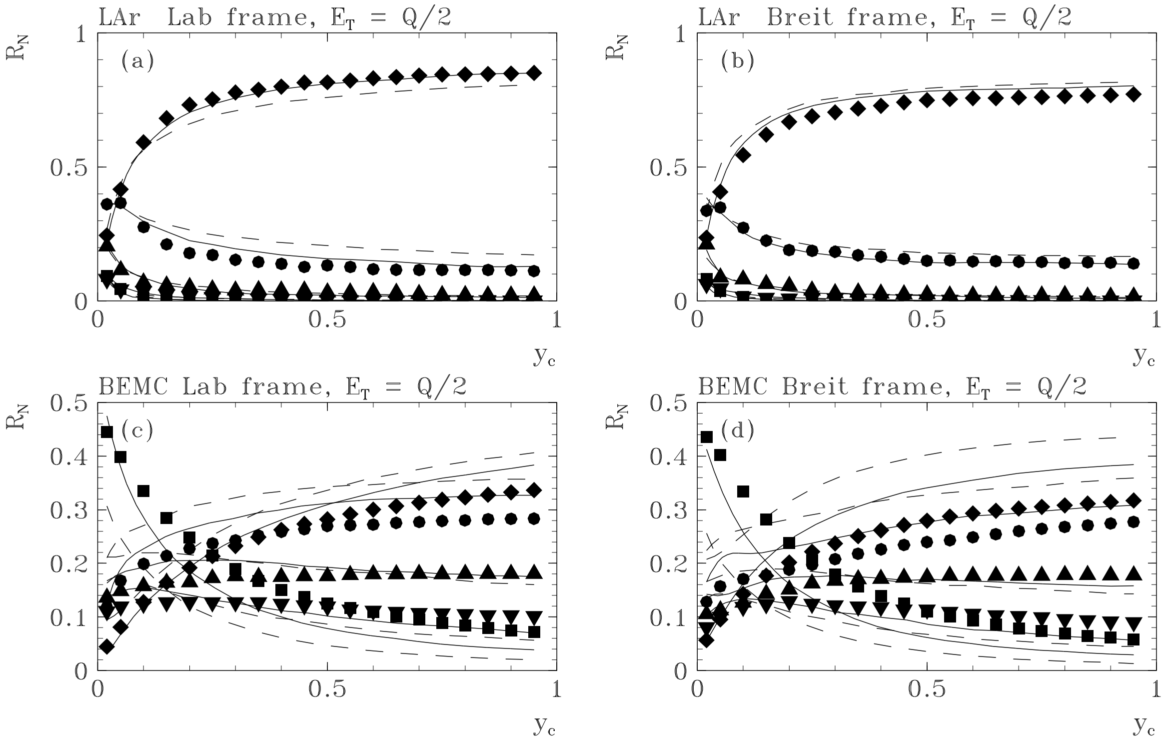

Figure 10.22: *k_t algorithm compared to H1 data on a linear scale. The content is identical to the one in figure 10.21, only the region of large y_c is shown in more detail on the linear scale.*

Chapter 11

Results

After all necessary tools are prepared and cross checks are made, this section deals with the results, which will come in three parts. First comparisons of the H1 data with the existing event generators will be discussed, concentrating on jet distributions and the (2+1)-jet rate evolution as a function of Q^2.

Then the feasibility of the measurements of the differential jet distribution and the jet cross section will be demonstrated.

The biggest part concerns the comparison of the H1 data to a QCD prediction, based only on fundamental parameters in QCD, in the framework of PROJET, namely the measurement of α_s from jet rates. A preliminary result is obtained. Then the pros and cons and the present limitations will be addressed, closing with an outlook to what may be attained in the near and distant future.

11.1 Jet rate distributions compared to the Event Generators

The R_{N+1} distributions and the $R_{2+1}(Q^2, y_c)$ ratio are considered here and compared to the predictions made by various event generators discussed in section 7. For details of the use of these event generators see [46].

Figure 11.1 shows the R_{N+1} distributions as a function of y_c for the BEMC (a) and LAr (b) sample without applying any jet cuts in terms of ϑ_{jet} and $p^{\star}_{t,jet}$. The H1 data is compared with the predictions of MEPS, HERWIG, CDM and DJANGO using $(W \cdot Q)$ as the maximum virtuality scale in a pure parton shower approach. The chosen PDF is $MRSD^{\circ}$ for all models. For the Monte Carlo predictions the corresponding luminosity is always less than the H1 data luminosity. For the various models only a limited statistics is available using $MRSD^{\circ}$ as PDF. For the MEPS model using $MRSD^{-}$ as PDF higher statistics is available (cf. table 9.1).

In the BEMC sample the descriptions by HERWIG and MEPS are fair, whereas CDM and DJANGO generate too many (2+1)-jet events. Although the Monte Carlo statistics in the LAr sample is low it can be seen that MEPS and CDM describe the data best. DJANGO again predicts to many (2+1)-jet events and HERWIG produces less than the data. From this it is clear that only MEPS is able to describe the evolution of (2+1)-jet events with Q^2. This is seen in figure 11.2, where $R_{2+1}(Q^2, y_c)$ is plotted for $y_c = 0.02$, this time applying the ϑ_{jet} cut. After suppressing the parton shower the results using HERWIG fall too low, over the whole Q^2 range and the DJANGO prediction is much too high. CDM gives a too flat Q^2 behaviour, it

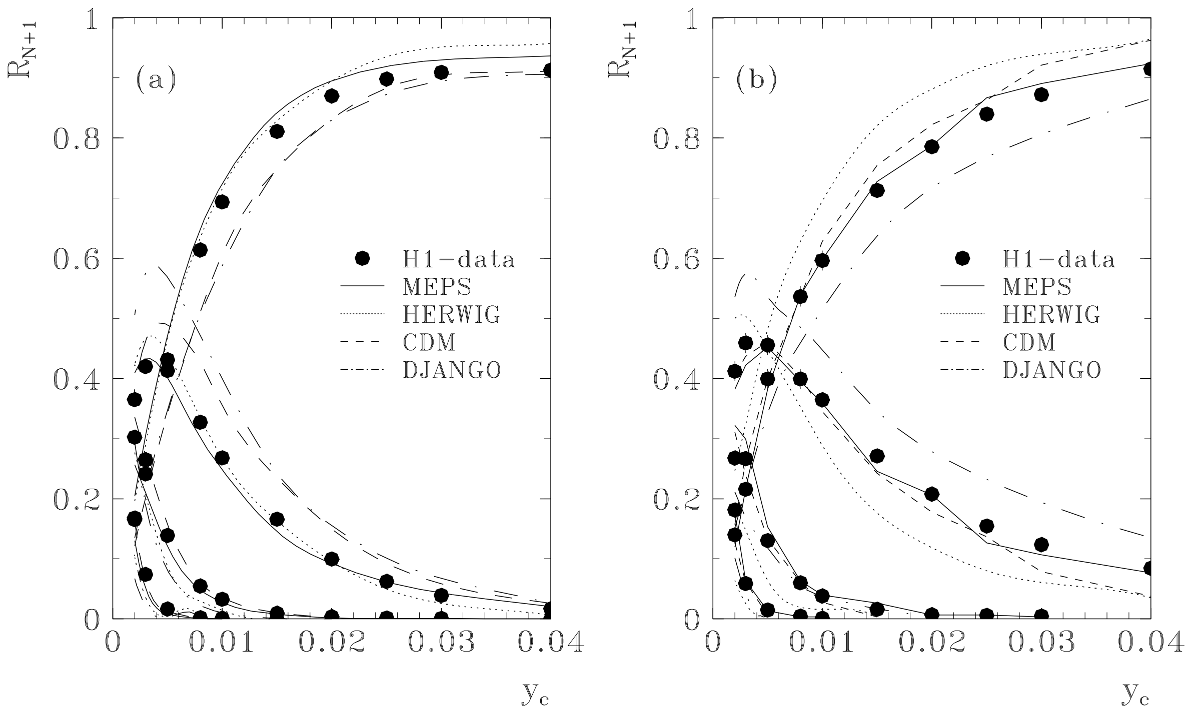

Figure 11.1: R_{N+1} *distribution compared to various event generators. The points represent the H1 data, the lines are the Monte Carlo predictions on the detector level for the BEMC (a) and the LAr (b) sample. Considered here are MEPS (full lines), Herwig (dotted lines), the colour dipol model CDM (dashed lines) and DJANGO (dash dotted lines) all using MRSD° as the PDF.*

overshoots the data in the BEMC region and undershoots it in the last two bins. Only MEPS describes all features of the jet rates quite reasonably. This confirms earlier results, obtained using 1992 H1 data, which can be found in [46].

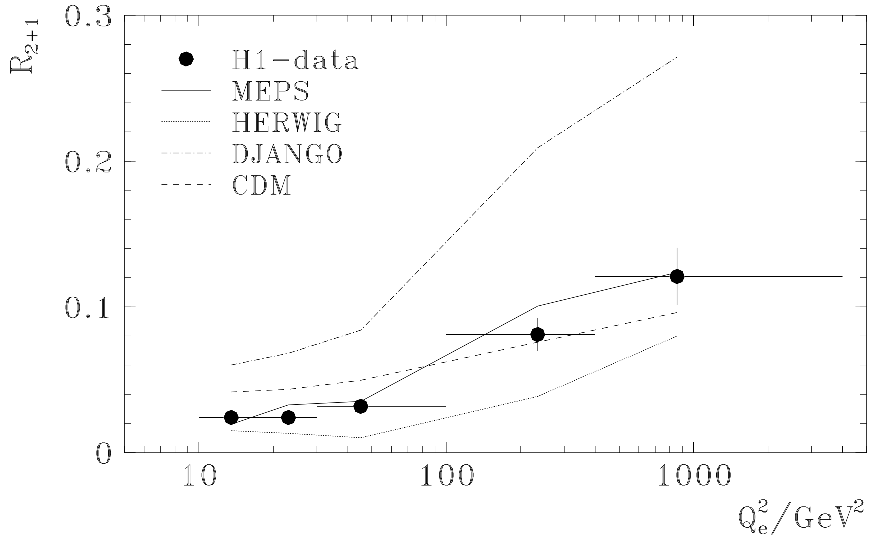

Figure 11.2: *Uncorrected $R_{2+1}(Q^2, y_c)$ ratio compared to event generators. The definitions are as in figure 11.1, but the ϑ_{jet} cut is applied to suppress the parton showers. For explanations see text.*

11.2 H1 jet data compared to the MEPS predictions

Because LEPTO61 is used to correct from the detector to the parton level, the agreement of LEPTO61 with the observed H1 data before and after the jet cuts described in section 10.2 is explored in more detail. Considered are the jet rates and the jet kinematic in terms of ϑ_{jet} and $p^{\star}_{t,jet}$ spectra.

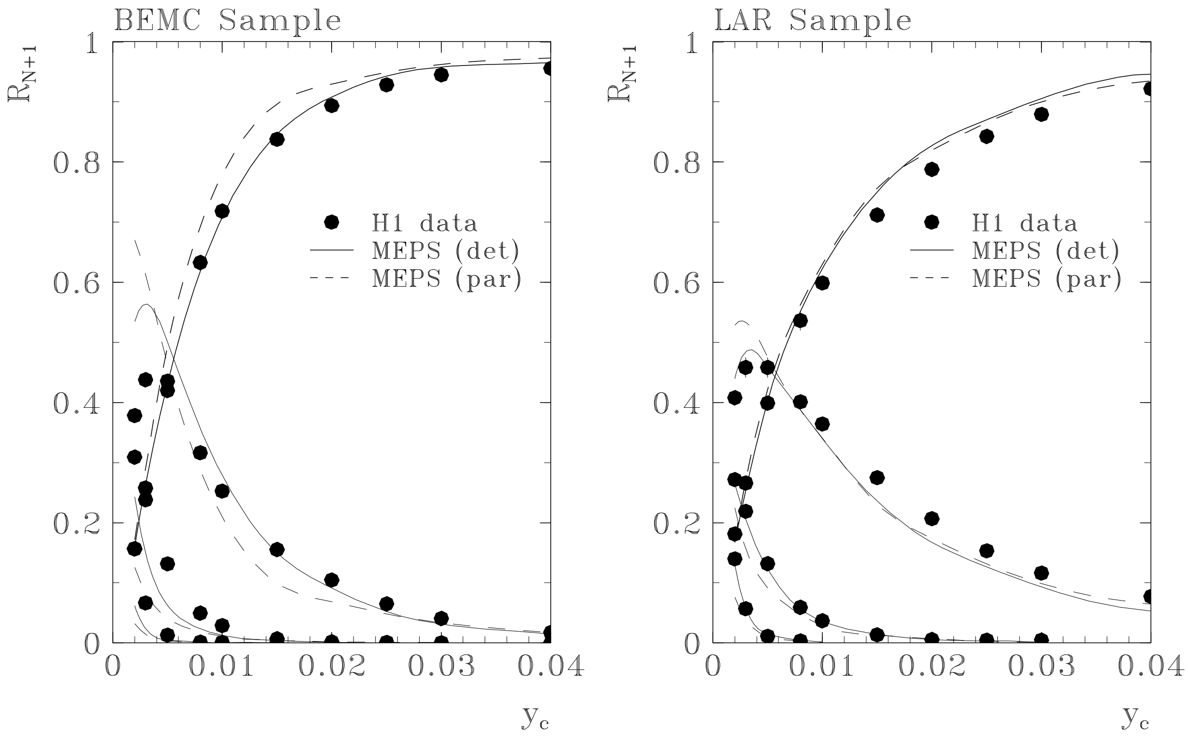

Figure 11.3: *R_{N+1} distribution compared to MEPS without PS suppression. Shown are the observed jet rates as data points and the MEPS predictions as lines. The full line represents the jets on the detector level and the dashed line the ones on the parton level. The used PDF is MRSD$^-$.*

Figure 11.3 show the jet rates in the BEMC and LAr sample once more, this time using *MRSD*$^-$ as the PDF and with much higher statistics in the LAr sample (cf. table 9.1) than in section 11.1. The jet cuts are not applied. The H1 data is shown as points, the errors are smaller than the symbol size, the full line is the MEPS prediction on detector level and the dashed line is the prediction for the parton level jets. For the BEMC sample the description of the jet rate above $y_c = 0.02$ is good whereas below that MEPS predicts fewer jets than are observed in the data. For the LAr sample the result is different. The description below $y_c = 0.01$ is almost perfect for all multiplicities. The high jet multiplicities >(3+1)-jets are described perfectly, but there is a significant difference in the (2+1)-jet rate and correspondingly in the (1+1)-jet rate for $y_c > 0.02$. After imposing the ϑ_{jet} cut for all events which are (2+1)-jet events at $y_c = 0.02$

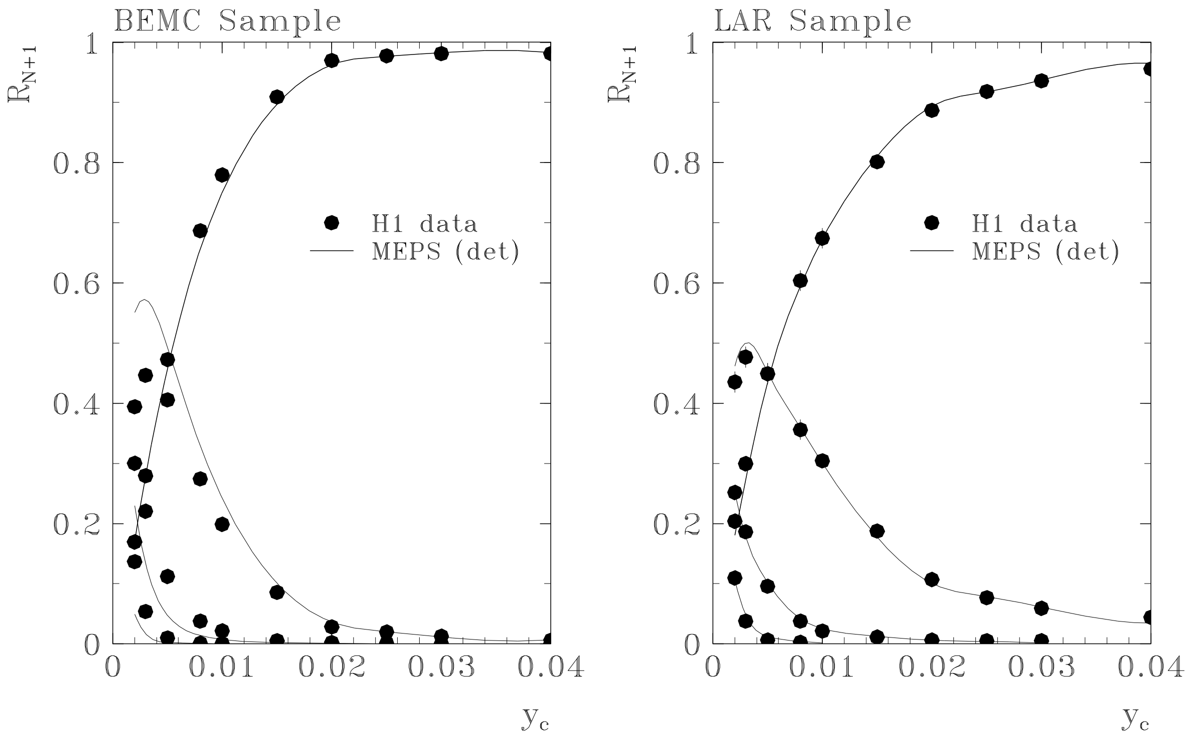

Figure 11.4: *R_{N+1} distribution compared to MEPS with PS suppressed. The ϑ_{jet} cut is applied only for those events which are (2+1)-jet events at $y_c = 0.02$. Shown are the observed jet rates as data points and the MEPS predictions on detector level as full line. The used PDF is MRSD$^-$.*

(cf. figure 11.4) the description of the seen jet rates by MEPS is perfect for the LAr sample for all y_c, for the BEMC sample the discrepancy at low y_c remains. For $y_c > 0.015$ the rates are described well in both samples.

Concerning the ϑ_{jet} and $p^\star_{t,jet}$ distributions, the prediction by MEPS is reasonably good, both before and after reduction of PS. The exception is the low ϑ_{jet} region, where the data show more jets than predicted by MEPS. This can be seen from the figures 11.5 and 11.6, which contain the inclusive ϑ_{jet} and $p^\star_{t,jet}$ spectra for all (2+1)-jet events at $y_c = 0.02$ on the detector level. The distributions are all normalized to unit area. The distributions (a, c) are without, while (b, d) are with reduction of PS. After applying the cuts one observes a small shift in $p^\star_{t,jet}$ in both samples.

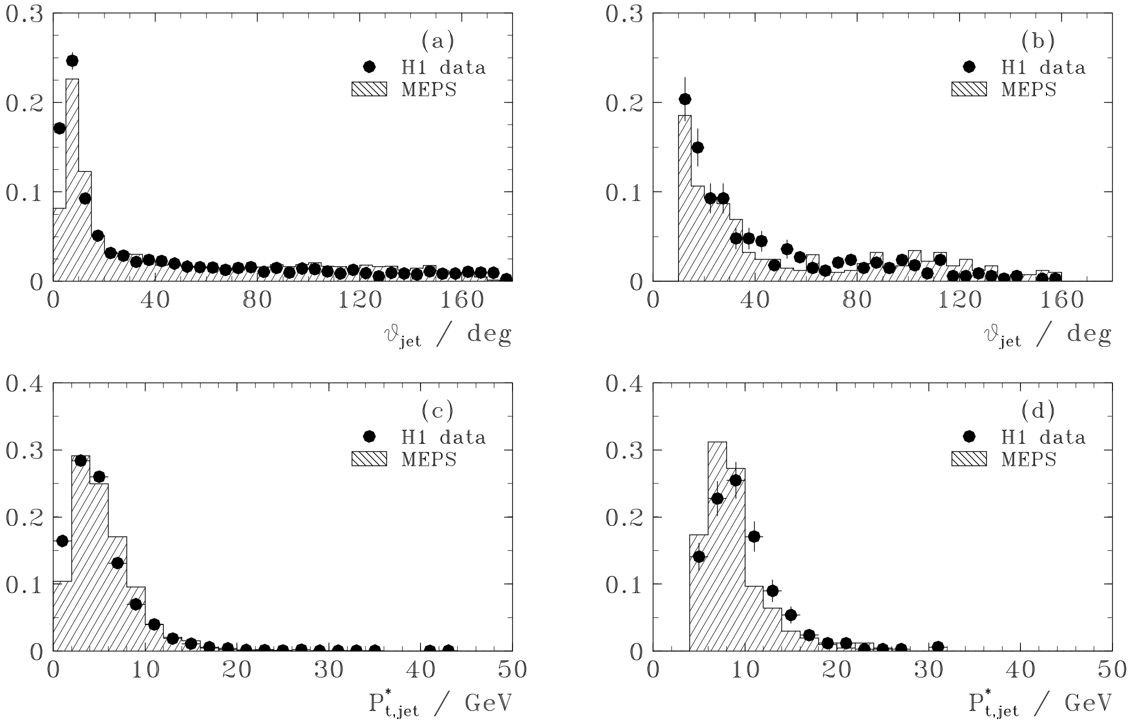

Figure 11.5: *The inclusive* ϑ_{jet} *and* $p^{\star}_{t,jet}$ *distributions for the BEMC sample compared to MEPS. The data are represented by the points, the Monte Carlo by the histogram.*

(a) *The* ϑ_{jet} *distribution before the cuts.*
(b) *The* ϑ_{jet} *distribution with both cuts applied.*
(c) *The* $p^{\star}_{t,jet}$ *distribution before the cuts.*
(d) *The* $p^{\star}_{t,jet}$ *distribution with both cuts applied.*

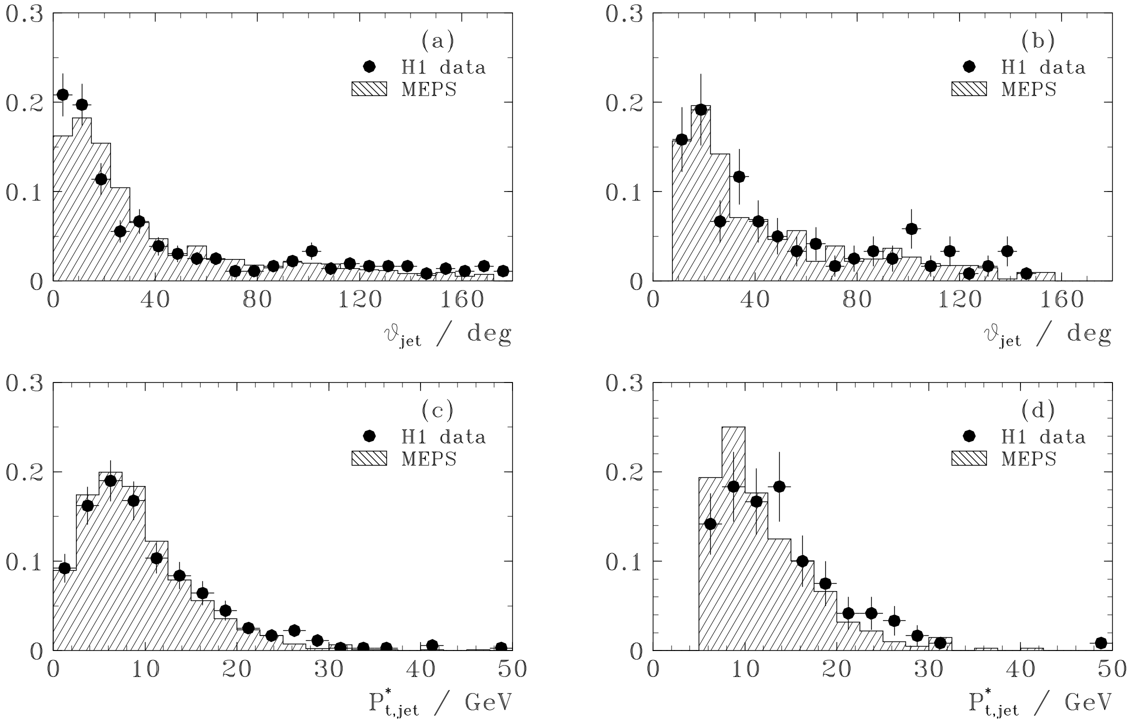

Figure 11.6: *The inclusive* ϑ_{jet} *and* $p^{\star}_{t,jet}$ *distributions for the LAr sample compared to MEPS. The definitions and ordering of figures a-d are as in figure 11.5.*

11.3 Measurement of the $D_2(y_c)$ distribution

As discussed in section 6.2 the $D_2(y_c)$ distribution is the preferred one to use if one wants to fit the y_c behaviour of the (2+1)-jet rate. Although this will not be used in this work, the general feasibility will be demonstrated. Figure 11.7 contains the $D_2(y_c)$ distribution as measured by the H1 experiment together with the $D_3(y_c)$ and $D_4(y_c)$ distribution, defined in equation 6.7 and 6.8 respectively and compared to the MEPS prediction on the parton level and the detector level, for both samples. All differential jet rates are well described in the LAr sample whereas

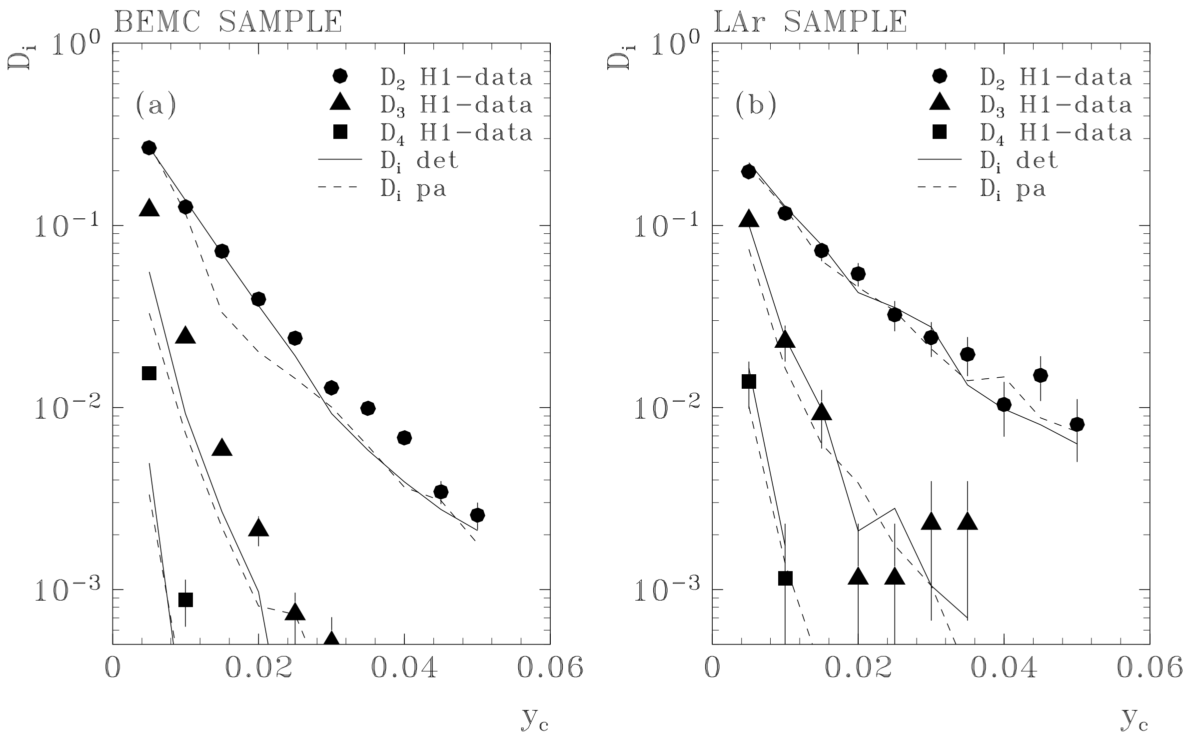

Figure 11.7: *The measured differential jet rates compared to MEPS. The points represent the H1 data, the lines are the MEPS prediction for the detector level (det) and the parton level (pa). No further jet cuts are applied. The used PDF is MRSD$^-$.*
(a) The BEMC sample.
(b) The LAr sample.

in the BEMC sample the description fails for $D_3(y_c)$ and $D_4(y_c)$ in the low y_c region and for $D_2(y_c)$ at high y_c. Certainly more work is needed to correct the $D_2(y_c)$ distribution to the parton level. The y_c behaviour in the whole range has to be studied. The low y_c region is dominated by non perturbative effects which have to be investigated in future.

11.4 Measurement of the (2+1)-jet cross section

As outlined in section 6.3 the (2+1)-jet cross section is a good quantity to measure α_s also at low Q^2, because it does not suffer from the PDF uncertainty at low ξ values. Here only the method will be outlined, therefore the simple and wrong assumption is used that all efficiencies are 100%.

		Bin 1	Bin 2	Bin 3	Bin 4	Bin 5
$y_c = 0.02$	N_{tot}	5151	3322	2966	568	273
	N_{2+1}	124	80	94	46	33
	$R\,[\%]$	2.4	2.4	3.2	8.1	12.1
$y_c = 0.03$	N_{tot}	5002	3243	2901	564	272
	N_{2+1}	49	35	43	25	19
	$R\,[\%]$	1.0	1.1	1.5	4.4	7.0

Table 11.1: *Uncorrected H1 data event distribution for five bins in Q^2 (cf. table 9.2). The $p^{\star}_{t,jet}$ cut is not applied.*

This assumption may be wrong by 10 to 20 %, but it is accurate enough for this purpose. Table 11.1 shows the uncorrected observed event distribution in the five bins in Q^2, with only the ϑ_{jet} cut applied for $y_c = 0.02$ and 0.03. The measured cross sections are derived from this table by using.

$$N_{ev} = \sigma \cdot \mathcal{L}_{int} \tag{11.1}$$

They are shown in table 11.2 together with the NLO PROJET estimate for the PDF's $MRSD^{\circ}$ and $MRSD^{-}$. The prediction for the total cross section is in the range of the measured values in all bins in Q^2, with $MRSD^{-}$ giving the higher values at low Q^2 and x. The (2+1)-jet cross section prediction agrees quite well for $Q^2 > 100\ GeV^2$, whereas below more jets are seen in the data than predicted by PROJET with the expectation being always lower for $MRSD^{-}$ than for $MRSD^{\circ}$. Consequently higher α_s values than used in the integration are favoured.

This demonstrates the feasibility of the measurement, however several experimental uncertainties are not covered here. At the moment the H1 Luminosity measurement has an uncertainty of $\approx 7\%$. This uncertainty is directly proportional to the error in α_s and therefore sets at this stage the lower limit of accuracy possible at the moment using this method.

			Bin 1	Bin 2	Bin 3	Bin 4	Bin 5
$y_c = 0.02$	H1-data	σ_{tot} [pb]	13599	8770	7830	1397	672
		σ_{2+1} [pb]	328	211	248	113	81.2
	MRSD°	σ_{tot} [pb]	11158	7610	7152	1317	603
		σ_{2+1} [pb]	191	177	260	101	78.7
	MRSD⁻	σ_{tot} [pb]	15522	9603	8155	1350	589
		σ_{2+1} [pb]	179	161	241	92.9	75.1
	GRV	σ_{tot} [pb]	17847	11007	9221	1445	590
		σ_{2+1} [pb]	203	183	258	94.9	75.2
$y_c = 0.03$	H1-data	σ_{tot} [pb]	13205	8562	7659	1388	669
		σ_{2+1} [pb]	129	92.4	114	61.5	46.7
	MRSD°	σ_{tot} [pb]	11148	7601	7142	1316	603
		σ_{2+1} [pb]	102	94.4	144	60.0	50.9
	MRSD⁻	σ_{tot} [pb]	15508	9601	8153	1349	589
		σ_{2+1} [pb]	91.8	85.5	128	55.5	49.3

Table 11.2: *Uncorrected H1 data 'cross section' compared to PROJET. The H1 data cross sections are derived from table 11.1, using equation 11.1, for a simple model of* $\epsilon \equiv 1.0$. *The PROJET NLO cross section predictions are shown for the PDF's MRSD° and MRSD⁻ for* $\Lambda_{4,\overline{MS}} = 215\ MeV$ *and for GRV for* $\Lambda_{4,\overline{MS}} = 200\ MeV$, *the default values.*

11.5 The α_s determination and systematic uncertainties

The theoretical expectation of PROJET for the default α_s value in the PDF's roughly agree with the observed number of events in the H1 experiment. However, the (2+1)-jet cross section prediction is too low for both of the investigated PDF's. This indicates a higher value of α_s than that used while fitting the PDF's. Here one word of clarification is needed.

A value for α_s was already derived while fitting the PDF's to existing data. According to the chosen strategy (cf. section 6.1) of this analysis α_s is varied while fitting $R_{2+1}(Q^2, y_c)$. It seems as if one has to perform a combined fit of α_s and the PDF's to the H1 data, however this is a higher order correction.

Schematically what is done while calculating the (2+1)-jet cross section is a convolution of the PDF's with a matrix element.

$$\begin{aligned} \hat{O}(\Lambda^2) &\sim PDF \cdot ME \\ \hat{O}(\Lambda^2) &\sim \left(\Phi^{\circ}_{i/p} + \alpha_s(\Lambda'^2)\, \Phi^{1}_{i/p}\right) \cdot \left(\alpha_s(\Lambda'^2)\, A + \alpha_s^2(\Lambda'^2)\, B\right) \end{aligned} \tag{11.2}$$

If one changes $\alpha_s(\Lambda'^2)$ to $\alpha_s(\Lambda^2)$ only in the second term, as is done here while fitting α_s, one gets.

$$\hat{O}(\Lambda^2) \sim \left(\Phi^{\circ}_{i/p} + \alpha_s(\Lambda'^2)\, \Phi^{1}_{i/p}\right) \cdot \left(\alpha_s(\Lambda^2)\, A + \alpha_s^2(\Lambda^2)\, B\right) \tag{11.3}$$

Inserting for $\alpha_s(\Lambda'^2)$ a similar expression as equation 2.7, which can be derived by differentiation with respect to Λ (cf. section 2.2), this can be written as

$$\hat{O}(\Lambda^2) \sim \left(\Phi^{\circ}_{i/p} + \alpha_s(\Lambda^2) \cdot \left[1 + \frac{\beta_0}{4\pi} \cdot \log\frac{\Lambda'^2}{\Lambda^2} \cdot \alpha_s(\Lambda^2)\right] \Phi^{1}_{i/p}\right) \cdot (\alpha_s(\Lambda^2) A + \alpha_s^2(\Lambda^2) B) \tag{11.4}$$

By multiplying the two factors it is seen that to $\mathcal{O}(\alpha_s^2)$ there is no change. The correction is formally to $\mathcal{O}(\alpha_s^3)$ because the parton densities are folded with a quantity which starts at $\mathcal{O}(\alpha_s)$. Consequently there is no need to fit the PDF as well.

The result of the fit to α_s is shown in figure 11.8 assuming $MRSD^\circ$ is the correct PDF. Figure 11.8 (a) shows the measured $R_{2+1}(Q^2, y_c)$ ratio corrected to the parton level (cf. table 10.1) for $y_c = 0.02$ and as a function of Q^2. The errors are the statistical errors only. They are obtained by adding in quadrature the statistical error from the data and the correction factors. Unfortunately at this stage, due to lack of Monte Carlo statistics, the errors for the correction factors are comparable to the statistical errors of the data. The lines are the PROJET predictions for various values of Λ. This information is translated in five measurements of α_s, figure 11.8 (b), using equation 6.1. Then the MINUIT program [50] is used to fit two model assumptions (cf. equation 6.5). The horizontal band shows the α_s value together with its one standard deviation errors quoted by MINUIT [1], for the assumption that α_s is constant and has no variation with Q^2. The band which lies on top of the data is obtained in a similar way, this time using the 2-loop α_s expression equation 2.5 and fitting Λ. The solution taken here is to integrate the cross sections for the $\Lambda_{4,\overline{MS}}$ value which is quoted together with the PDF ($\Lambda_{4,\overline{MS}} = 215\ MeV$ for $MRSD^\circ$ and $MRSD^-$), to calculate from that the $A_{ij}(Q^2, y_c)$ coefficients (cf. section 6.1), and to vary α_s in the fit program without integrating at every Λ variation during the fit procedure. The consistency is checked by integrating using PROJET for $\Lambda_{4,\overline{MS}} = 400\ MeV$ and fitting α_s again.

[1] A one standard deviation error of a parameter in MINUIT is defined as follows. The parameter is varied around the fitted value in a range corresponding to a change in χ^2_{min} of ± 1. The corresponding change in the parameter is quoted as it's error, which may be asymmetric.

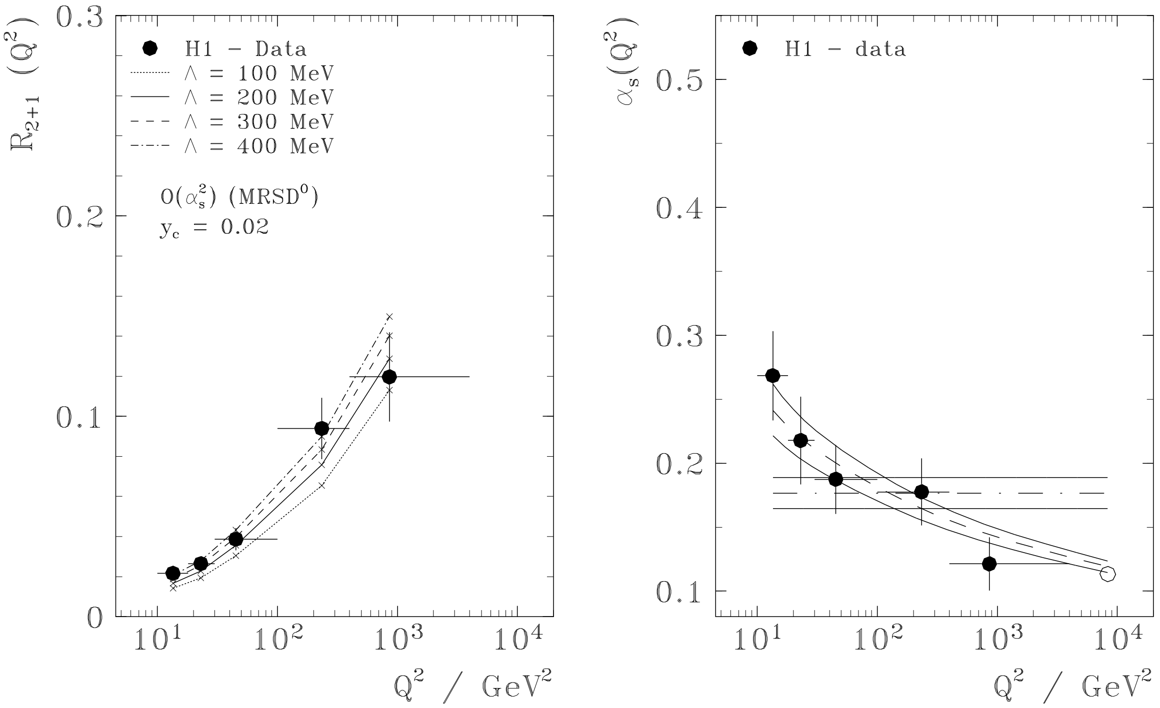

Figure 11.8: *α_s fit using MRSD° at $y_c = 0.02$. The full points represent the H1 measurement corrected to the parton level, the PROJET prediction in (a) are the small crosses connected by lines for different values of $\Lambda_{4,\overline{MS}}$. The results of the fits in (b) are shown as bands of the fitted values and the $\pm$ 1 standard deviation parameter error lines. Errors on the data are only statistical. The open circle is the mean value of α_s obtained by the particle data group together with its error (cf. table 1.1).*

- *(a)* *The $R_{2+1}(Q^2, y_c)$ jet rate as a function of Q^2 at $y_c = 0.02$, together with the PROJET prediction for MRSD° at various Λ values.*
- *(b)* *The α_s measurement, together with two fit scenarios. For both the fit value and the $\pm 1\sigma$ curves are displayed. The two scenarios are α_s= const and running α_s using equation 2.5.*

The α_s result in figure 11.8 is the same, leading to a difference in $\Lambda_{4,\overline{MS}}$ of 2 MeV. This error, due to the chosen cpu time saving strategy, is neglected.

The data unambiguously favours the running of α_s. Extrapolating to the mass of the Z° one gets $\alpha_s(M_z^2) = 0.119\,^{+0.004}_{-0.005}$. The fit has a reasonable probability leading to $\chi^2/dof = 0.58$, whereas the assumption of α_s being constant is unlikely, giving $\chi^2/dof = 3.88$ [2].

This shows for the first time a result consistent with the running of α_s using one observable in one single experiment operated at a constant center of mass energy of the accelerator. The systematic uncertainties are discussed next, always taking conservative estimates of the systematic errors.

11.5.1 Dependence on jet requirements and energy scale

This section deals with the uncertainty of α_s by different selection criteria and its dependence on the hadronic energy scale. As long as one stays in the perturbative regime the change in $R_{2+1}(Q^2, y_c)$ by changing the requirements should be described by PROJET, leaving α_s unchanged.

In the following, three subjects will be discussed.

- The dependence of α_s on y_c
- The dependence of α_s on the $p^\star_{t,jet}$ cut
- The dependence on the hadronic energy scale

Figure 11.9 shows the α_s fit using $MRSD^\circ$ at $y_c = 0.03$. The statistical precision gets weaker due to the rapid drop in $R_{2+1}(Q^2, y_c)$ with y_c. The fit leads to $\alpha_s(M_z^2) = 0.124\,^{+0.006}_{-0.007}$ which is higher than the value obtained at $y_c = 0.02$. From this difference (cf. table 11.3) a y_c error on α_s as half the spread of the measurements without $p^\star_{t,jet}$ cut is derived $\Delta\alpha_s(M_z^2) = 0.003$.

In the last two figures the $p^\star_{t,jet}$ cut was not applied. At least in the two lowest Q^2 bins there are good reasons to introduce this hard scale (cf. section 10.2). The uncertainty due to this cut is demonstrated in figure 11.10 which shows the fit analogous to figure 11.8 but this time applying the $p^\star_{t,jet}$ cut. The obtained value is $\alpha_s(M_z^2) = 0.116\,^{+0.006}_{-0.007}$. This is a bit lower than in figure 11.8. From table 11.3 an error of $\Delta\alpha_s(M_z^2) = \pm 0.003$ is derived from the full spread for $y_c = 0.02$ within $MRSD^\circ$. To summarize, using the table 11.3, it can be stated that the errors are of the order of the actual statistical precision.

The hadronic energy scale of the LAr detector is at present known to an accuracy of $\approx 5\%$. The effect of the hadronic energy scale only partly cancels in the jet algorithm while dividing m_{ij}^2 by W^2. m_{ij}^2 depends quadratically on the energy scale because it contains $E_i \cdot E_j$, W^2 has only a linear dependence on the energy scale. No matter how one calculates W^2 it always contains an energy from the initial proton or electron (cf. equation 3.11 and 10.1). Therefore the jet rates depend linearly on the hadronic energy scale. The effect of this is studied by rescaling of the hadronic energy by $\pm 5\%$ and recalculating the jet rate. The error on the jet rate is $\approx 7\%$ leading to an uncertainty in α_s of $\Delta\alpha_s(M_z^2) = \,^{+0.006}_{-0.007}$.

In all these considerations, it is assumed that $MRSD^\circ$ is the correct PDF, which isn't the case. Measurements of F_2 at HERA have shown that for the inclusive cross section the parametrization $MRSD^-$ is favoured [19]. The impact of the PDF choice is evaluated in the next section.

[2] The model assumption of a constant α_s is shown only for illustration. This model is not a consistent description, because in the PROJET expectation also those terms of the matrix elements which would not exist if α_s were constant are considered.

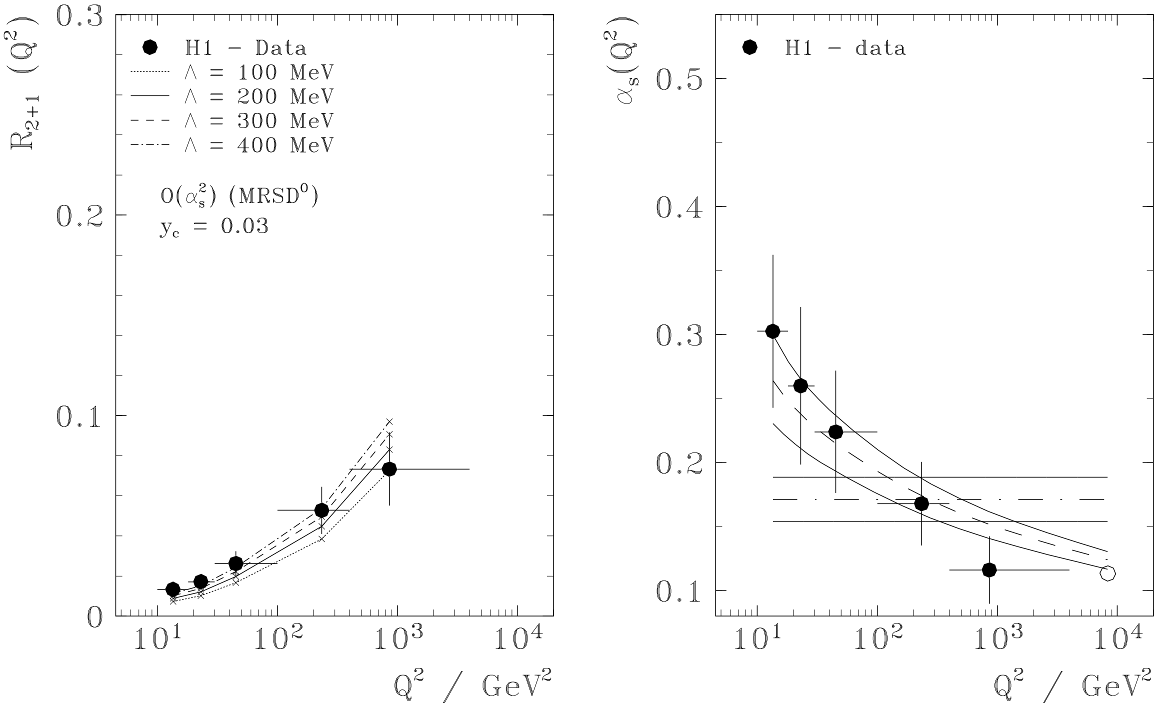

Figure 11.9: *α_s fit using MRSD° at $y_c = 0.03$. The ordering of the figures and the definitions are as in figure 11.8.*

PDF	y_c	$p^\star_{t,jet}$ [GeV]	$\alpha_s(M_z^2)$	$\Lambda_{4,\overline{MS}}$ [MeV]	χ^2/dof
MRSD°	0.02		$0.119^{+0.004}_{-0.005}$	345^{+80}_{-74}	0.58
	0.02	5	$0.116^{+0.006}_{-0.007}$	289^{+104}_{-91}	0.44
	0.03		$0.124^{+0.006}_{-0.007}$	433^{+139}_{-129}	0.61
	0.03	5	$0.119^{+0.007}_{-0.008}$	335^{+140}_{-121}	0.38
MRSD⁻	0.02		$0.135^{+0.004}_{-0.004}$	673^{+105}_{-105}	1.72
	0.02	5	$0.131^{+0.006}_{-0.007}$	575^{+155}_{-147}	1.50
	0.03		$0.138^{+0.006}_{-0.007}$	763^{+171}_{-174}	1.64
	0.03	5	$0.131^{+0.007}_{-0.008}$	585^{+185}_{-176}	1.38
GRV	0.02		$0.135^{+0.004}_{-0.004}$	681^{+107}_{-108}	1.75
	0.02	5	$0.131^{+0.006}_{-0.007}$	577^{+158}_{-150}	1.51

Table 11.3: *α_s fits for various scenarios without ξ cut.*

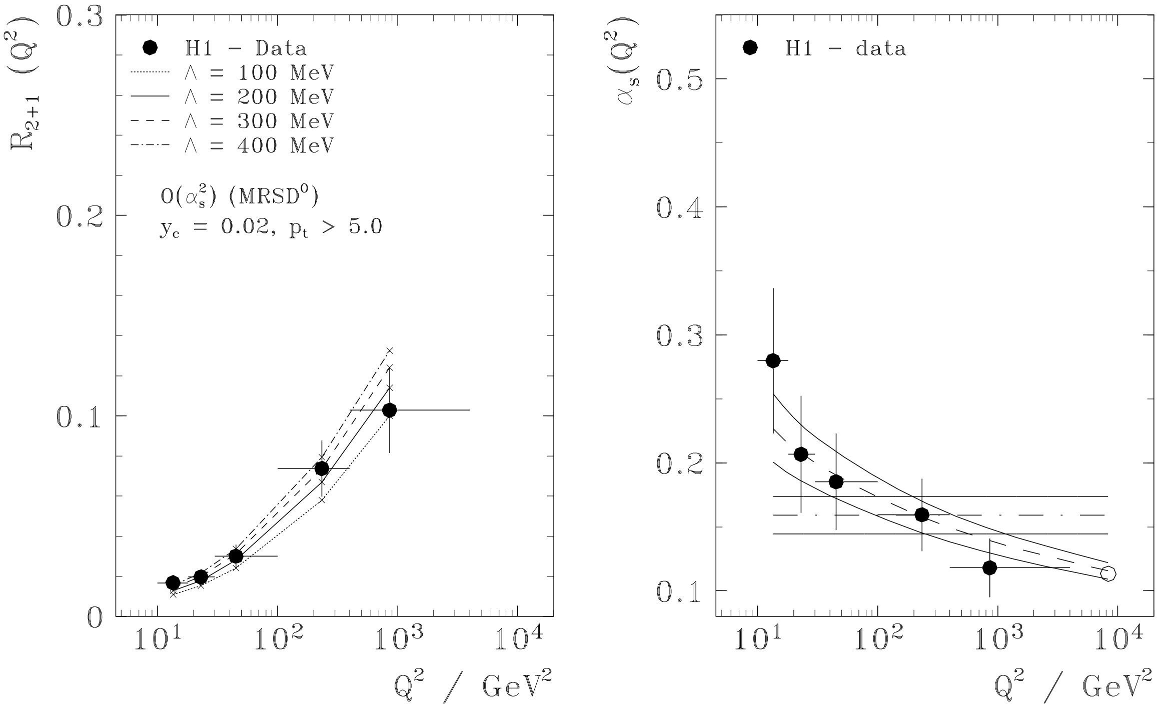

Figure 11.10: *α_s dependence on the $p^{\star}_{t,jet}$ cut. $p^{\star}_{t,jet} > 5$ GeV is required. The ordering of the figures and the definitions are as in figure 11.8.*

11.5.2 Dependence on parton densities

At HERA an unmeasured region in ξ is explored. The uncertainty in the PDF's in this regime $\xi < 10^{-2}$ is large as can be seen from figure 3.8.

The influence on the fitted α_s value is shown in figure 11.11 using the same requirements as in figure 11.8 but this time using *MRSD*$^-$ as PDF. This fit leads to a value of $\alpha_s(M_z^2) = 0.135 \pm 0.004$. This is significantly different to the value obtained in figure 11.8. The reason

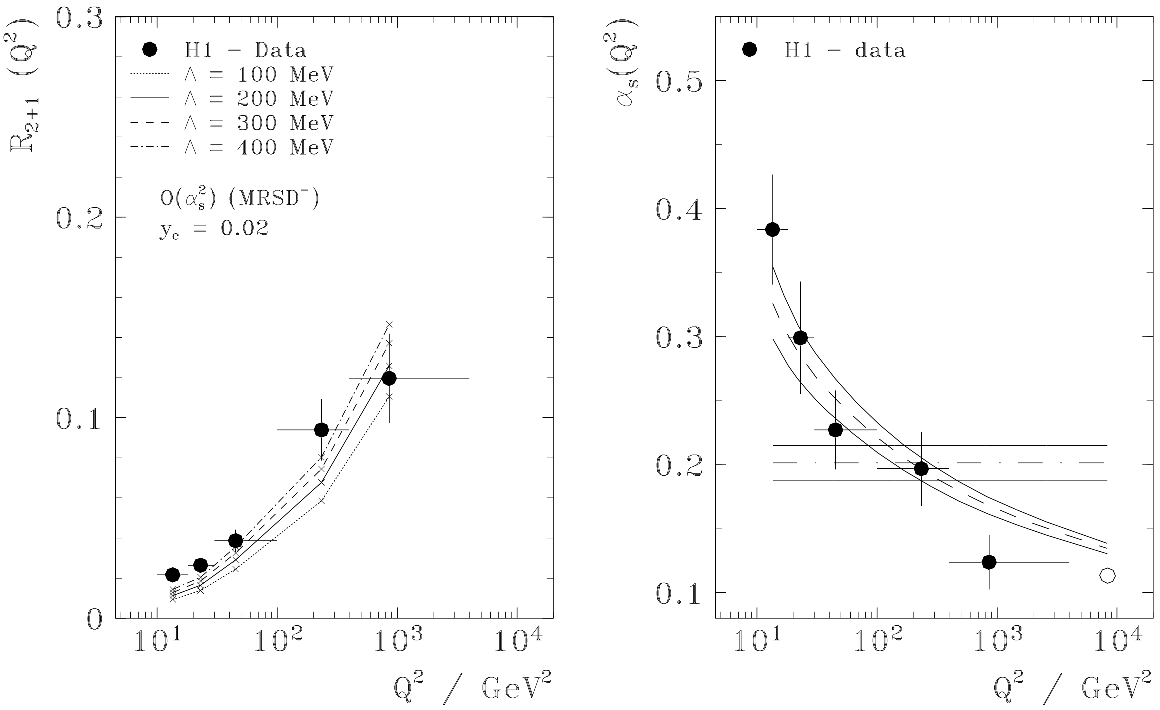

Figure 11.11: α_s *fit using MRSD*$^-$ *at* $y_c = 0.02$. *The ordering of the figures and the definitions are as in figure 11.8.*

being mainly the uncertainty in the total cross section (cf. table 11.2) in the low Q^2 bins. Here the measured $R_{2+1}(Q^2, y_c)$ lies significant above the *MRSD*$^-$ prediction. In this region however the sensitivity to α_s is largest (cf. figure 2.3). The uncertainty of the $R_{2+1}(Q^2, y_c)$ rate is in the order of 55% for $Q^2 = 13.5\ GeV^2$ decreasing to 10% at $Q^2 = 234\ GeV^2$ (cf. Bin 1 and 4 of table 11.2). The prediction for the (2+1)-jet cross section however, differ only by 11% and 8% in the same Q^2 range.

As already discussed in section 6.3 this can be circumvented by applying a ξ cut for the (1+1)-jet events, which in this case is equivalent to a x cut. The chosen cut is $\xi > 10^{-2}$ for the (1+1)-jet events, the (2+1)-jet events are unaffected by this. For the two lowest Q^2 bins, $x < 10^{-2}$ (cf. figure 9.1), so they are lost due to this cut. The figures 11.12 and 11.13 show the result of this cut using *MRSD*$^-$ and *MRSD*$^\circ$. Because it only acts on the denominator and

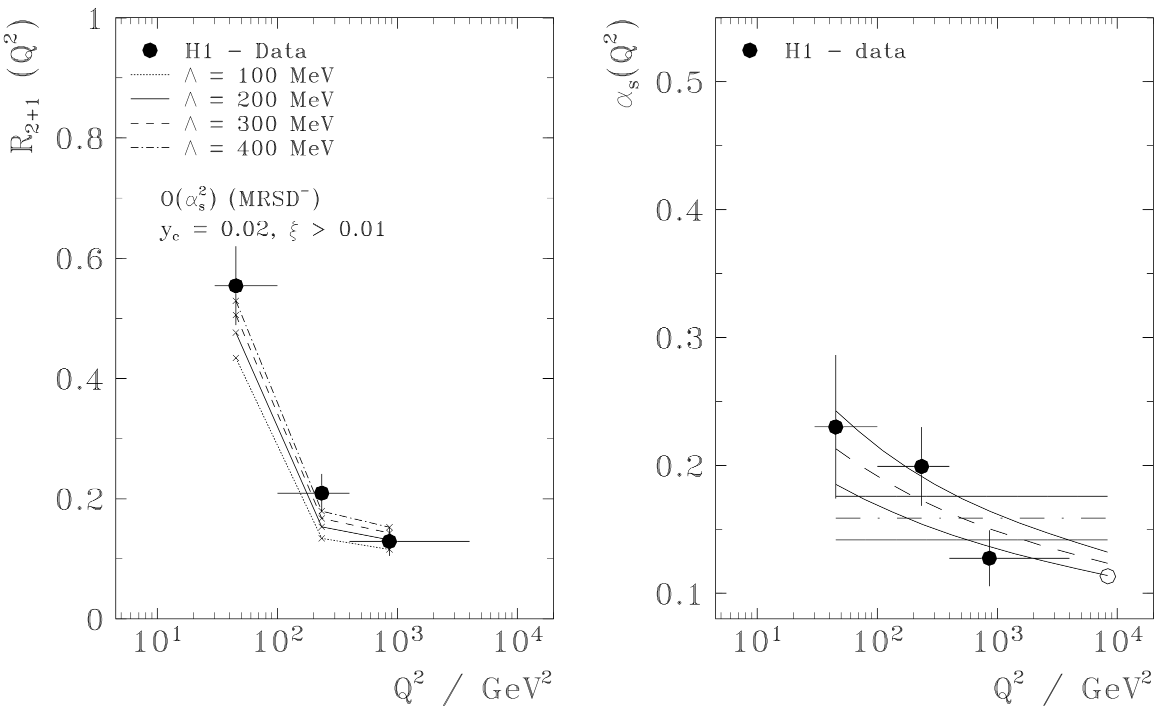

Figure 11.12: *α_s fit using MRSD$^-$ at $y_c = 0.02$ and $\xi > 0.01$. The ordering of the figures and the definitions are as in figure 11.8.*

gives a stronger reduction in the lower Q^2 range, the jet rate now decreases as a function of Q^2. The results of the fits are $\alpha_s(M_z^2) = 0.123\,^{+0.009}_{-0.010}$ for *MRSD*$^-$ and $\alpha_s(M_z^2) = 0.120\,^{+0.009}_{-0.010}$ for *MRSD°*. The statistical precision gets weaker, but now the dependence on the PDF is nearly gone (cf. table 11.4). Although the jet rates are totally different compared to the ones without the ξ cut the α_s values agree within statistical errors. This can be seen by comparing the figures 11.8 and 11.13. However *MRSD*$^-$ still gives the higher value. From table 11.4 an error due to the PDF uncertainty is derived as the spread of the extreme values without the $p^\star_{t,jet}$ cut, leading to $\Delta\alpha_s(M_z^2) = \pm 0.003$.

11.5.3 Dependence on the renormalization and factorization scale

In section 2.2 it was discussed that the main uncertainty in the LEP measurement of α_s, from jet rates in the E0 scheme by using fixed order calculation, is due to the unknown renormalization scale. In *ep-* scattering one has to deal with this uncertainty as well and in addition to that with the factorization scale dependence.

Figure 11.14 shows the change of the (2+1)-jet cross section and the $R_{2+1}(Q^2, y_c)$ jet rate as a function of the variation in the scales. The PROJET integration is performed using *MRSD°*

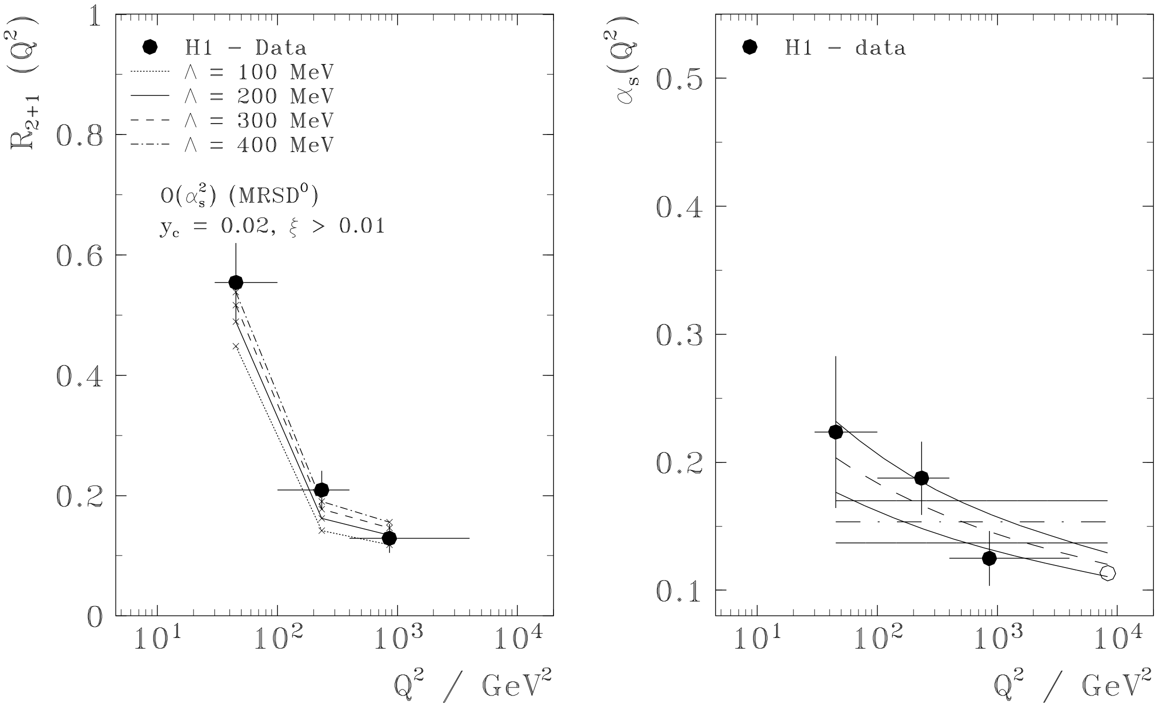

Figure 11.13: *α_s fit using MRSD° at $y_c = 0.02$ and $\xi > 0.01$. The ordering of the figures and the definitions are as in figure 11.8.*

for $Q^2 > 100\ GeV^2$. The variation is done using.

$$\mu = \varrho\ Q \qquad\qquad \mu_f = \varrho_f\ Q \tag{11.5}$$

They are chosen as multiples of Q because in the renormalization of the γq vertex the scale in $\alpha_s(\mu^2)$ depends on Lorentz invariants, which all are of the order of Q^2. Choosing for example W^2 as renormalization scale is therefore strongly disfavoured. Five values of ϱ and ϱ_f for μ^2 and μ_f^2 are considered (1/5, 1/2, 1, 2, 5). A priori it is not clear in what range one should vary the scales. In order to stay safely in the perturbative regime of DIS scattering only scales in μ^2 above 10 GeV^2 are considered, otherwise $\alpha_s(\mu^2)$ gets to large and one leaves the perturbative regime of DIS.

The uncertainty of $R_{2+1}(Q^2, y_c)$ due to the unknown factorization scale figure 11.14 (d) is found to be of the order of 2%, which is negligible at the present state of statistical accuracy and the factorization scale will not be discussed further here.

The renormalization scale, however, is seen to be important, although the scale dependence has been considerably reduced by including the NLO coefficient of the perturbative expansion (cf. figure 11.14 (a, b)). The uncertainty in the (2+1)-jet cross section in NLO is 20% over the whole range compared to 82% in the LO matrix element terms. The corresponding uncertainty of α_s due to this is studied next.

PDF	y_c	$p^\star_{t,jet}$ [GeV]	$\alpha_s(M_z^2)$	$\Lambda_{4,\overline{MS}}$ $[MeV]$	χ^2/dof
MRSD°	0.02		$0.120^{+0.009}_{-0.010}$	363^{+179}_{-144}	0.81
	0.02	5	$0.114^{+0.011}_{-0.012}$	259^{+184}_{-131}	0.65
MRSD⁻	0.02		$0.123^{+0.009}_{-0.010}$	421^{+193}_{-160}	0.98
	0.02	5	$0.117^{+0.011}_{-0.012}$	311^{+206}_{-152}	0.78
GRV	0.02		$0.121^{+0.009}_{-0.009}$	383^{+176}_{-145}	0.87
	0.02	5	$0.116^{+0.011}_{-0.011}$	288^{+189}_{-140}	0.68

Table 11.4: α_s *fits using the high* ξ *region* $\xi > 0.01$ *for various parton densities. In addition to the ones discussed in the text GRV is included as well.*

If one tries to fit for low ϱ values one encounters problems with the convergence of the fit in the lowest Q^2 bins and perturbative QCD is no longer applicable. Therefore the influence is studied by using the bins 4 and 5 alone and ϱ is varied from 1/2 up to 2, meaning that the lowest μ^2 reached in this procedure is 25 GeV^2. Figure 11.15 shows as an example the α_s fit for $\varrho = 1/2$. The results are displayed in table 11.5, for three different values of ϱ and using *MRSD°*. The scale error is derived as half the spread of the α_s values and amounts to $\Delta\alpha_s(M_z^2) = 0.006$. This concludes the systematic investigations made so far.

ϱ	$\alpha_s(M_z^2)$	$\Lambda_{4,\overline{MS}}$ $[MeV]$	χ^2/dof
1/2	$0.114^{+0.010}_{-0.010}$	257^{+157}_{-120}	1.56
1	$0.118^{+0.010}_{-0.011}$	331^{+197}_{-149}	1.47
2	$0.125^{+0.012}_{-0.012}$	457^{+272}_{-204}	1.47

Table 11.5: α_s *dependence on the renormalization scale* μ^2 *for MRSD°, at* $y_c = 0.02$, $\xi > 0.01$ *and* $Q^2 > 100$ GeV^2.

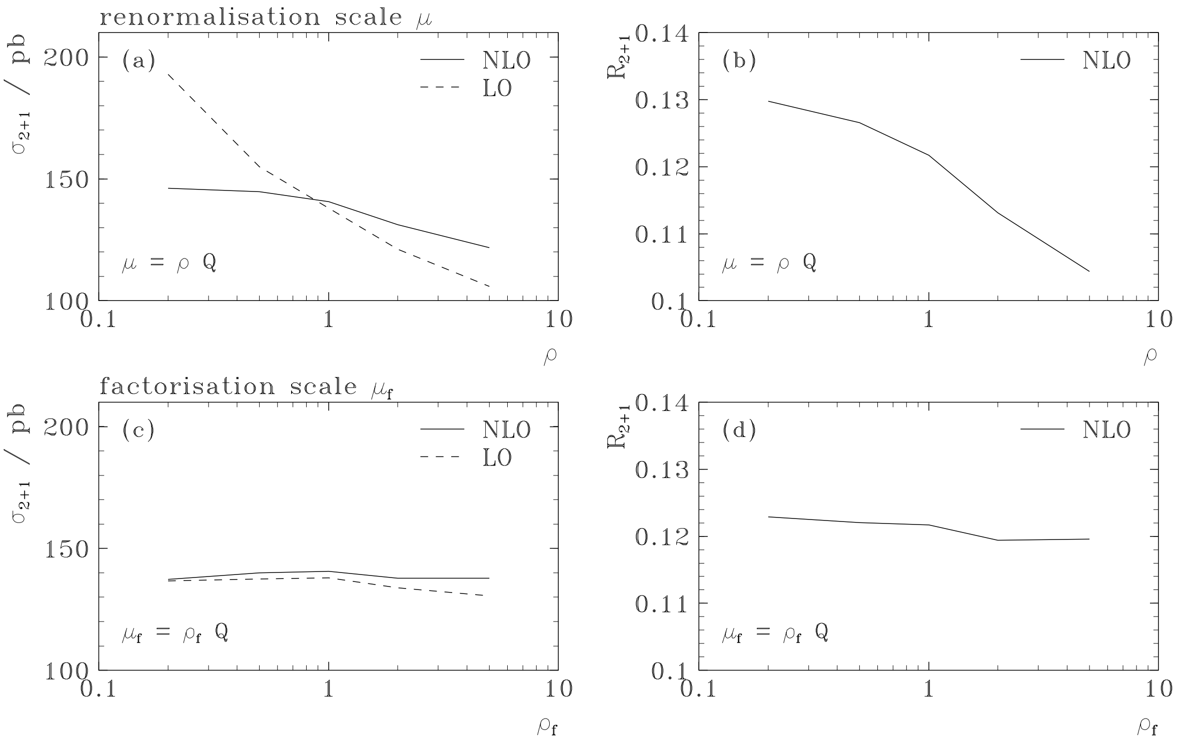

Figure 11.14: *The scale dependencies of NLO cross sections using MRSD° at $y_c = 0.02$ for Bin 4 and 5. The $p^{\star}_{t,jet}$ cut and the ϑ_{jet} cut are applied. The scales are varied as multiples of Q, with ϱ and ϱ_f being the scale factors. For illustration the scale dependencies of the LO matrix element term in the (2+1)-jet cross section is shown as well.*

(a) The (2+1)-jet cross section variation as a function of ϱ.
(b) The $R_{2+1}(Q^2, y_c)$ variation as a function of ϱ.
(c) The (2+1)-jet cross section variation as a function of ϱ_f.
(d) The $R_{2+1}(Q^2, y_c)$ variation as a function of ϱ_f.

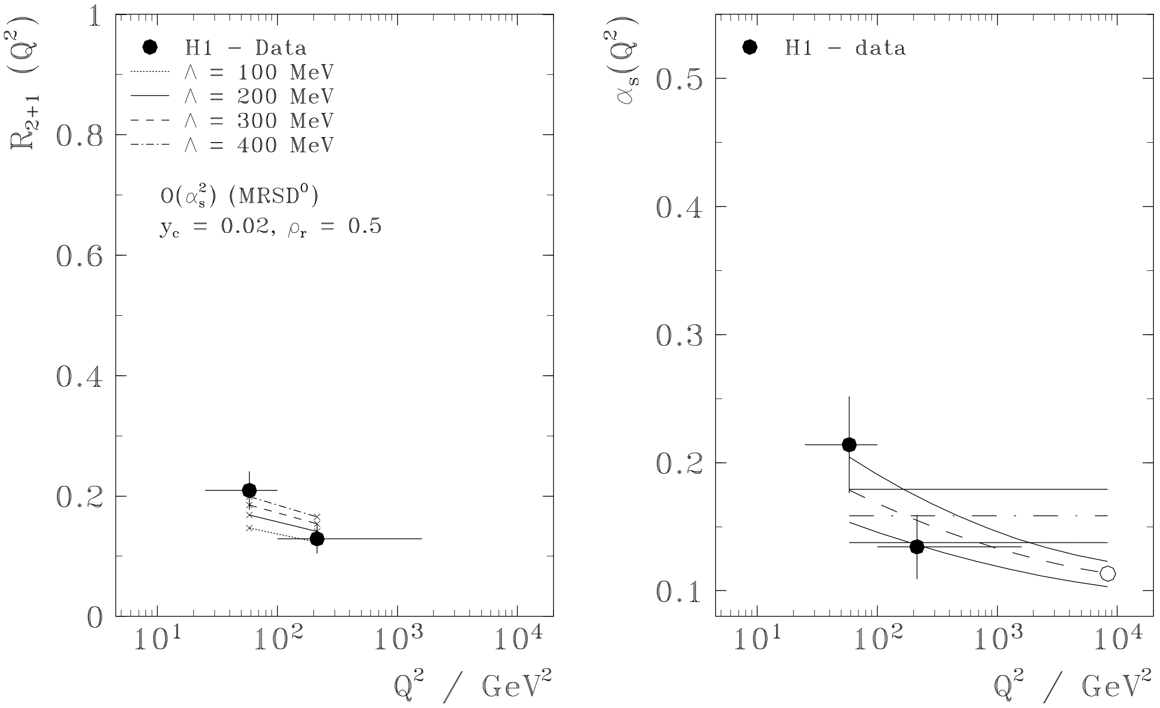

Figure 11.15: *α_s fit using MRSD$^-$ at $y_c = 0.02$ for $\varrho = 1/2$. The ordering of the figures and the definitions are as in figure 11.8.*

11.5.4 Summary of the systematic investigations on α_s

The variation of the fitted α_s value in the various chosen scenarios is displayed in figure 11.16 separately for *MRSD°* (a) and *MRSD⁻* (b).

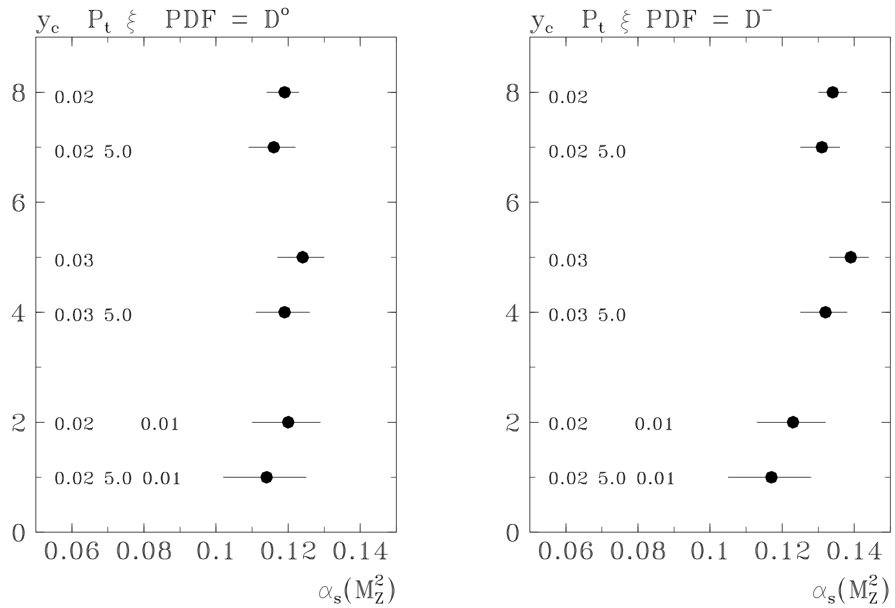

Figure 11.16: *Systematic investigations of the α_s measurement.*

The value of α_s quoted as the measurement from jet rates at H1 is derived as the mean value of the three measurements displayed in table 11.4 without the $p^{\star}_{t,jet}$ cut. The errors are as discussed in the last sections.

This is a preliminary result, because not all uncertainties have been studied fully yet. For example, the correction factors are taken only from LEPTO. No other QCD inspired event generator has been used so far to obtain these correction factors. Especially in the low Q^2 region one deals with jets of low energy and low transverse momenta, which may be sensitive to the details of the underlying QCD process and the fragmentation as modeled by the event generators. Taking into account different models the systematic error of the correction factors, which due to the use of a single generator at the moment is neglected, will increase. That means in turn, that the current systematic error on α_s may be underestimated.

In figure 11.17 the measurement obtained by this analysis is compared to the LEP results discussed in section 2.2, showing how precise the H1 measurement already is at this early stage of data taking.

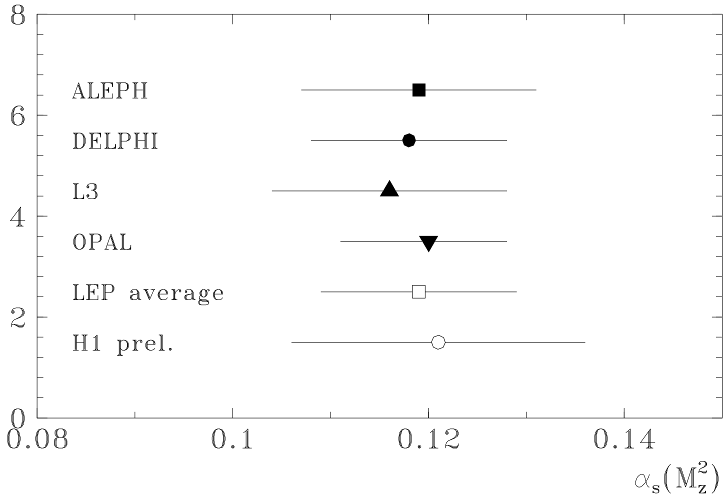

Figure 11.17: *The preliminary α_s measurement from jet rates at H1. For comparison the measurements from jet rates at LEP discussed in section 2.2 are given.*

Chapter 12

Conclusions

A detailed jet analysis on the 1993 H1 data corresponding to an integrated luminosity of $\mathcal{L}_{int} \approx 0.4\, pb^{-1}$ is performed using a modified JADE jet algorithm in which the proton remnant is included in the clustering procedure. This algorithm is found to be well suited for a jet definition in ep scattering, giving a good correlation between jets obtained on the detector level with those obtained from the underlying partonic structure. This concerns the jet rates and the jet four vectors in terms of ϑ_{jet} and $p^{\star}_{t,jet}$. The obtained resolutions for $Q^2 > 100\ GeV^2$ are a 18% $p^{\star}_{t,jet}$ resolution and 3.4° in polar angle.

This good agreement between observed jets and the underlying QCD process allows the data to to be corrected to the partonic level using an event generator. For this purpose at the moment only one QCD inspired generator, LEPTO61, based on LO jet cross sections, is used.

The corrected data are compared to a NLO calculation implemented in a jet cross section Monte Carlo program PROJET. With this QCD prediction the measured jet rate $R_{2+1}(Q^2, y_c)$ can be translated to several measurements of the strong coupling constant $\alpha_s(\mu^2)$ using only one observable in a single experiment. Extrapolating the measured $\alpha_s(\mu^2)$ values to $\mu^2 = M_z^2$, hereby taking in case of asymmetric errors always the higher value leads to

$$\begin{array}{rcllll} \alpha_s(M_z^2) & = & 0.121 \pm 0.010\ (stat) & \pm\, 0.003\ (y_c) & \pm\, 0.003\ (p^{\star}_{t,jet}) \\ & & \pm 0.007\ (E_{had}) & \pm\, 0.003\ (PDF) & \pm\, 0.006\ (\mu^2)\,. \end{array}$$

Adding the errors in quadrature gives $\alpha_s(M_z^2) = 0.121 \pm 0.015$.

This $\alpha_s(M_z^2)$ determination has the great advantage that it is possible to see the running of $\alpha_s(\mu^2)$ using one observable in a single experiment and that the QCD prediction of the RGE can be precisely verified in future.

At the moment the measurement suffers from low data statistics and the uncertainty in the PDF which restricts the measurement to much larger values in Q^2 than can be observed in the experiment. However, these two things interplay. If one could use the whole Q^2 range to fit $\alpha_s(\mu^2)$ with the present statistics and no PDF uncertainty one could measure $\alpha_s(M_z^2)$ already with an statistical error of 0.005.

In future this measurement will be improved in two ways. New PDF's will be fitted to the F_2 measurements at HERA which in turn can be used to perform the $\alpha_s(\mu^2)$ determination at lower Q^2 values, and the coming higher luminosity runs of HERA will reduce the statistical error. Then theoretical uncertainties, such as the scale uncertainty will set the limit on the $\alpha_s(M_z^2)$ measurement which is, as outlined in this work, suited to give a very precise $\alpha_s(M_z^2)$ measurement in the future.

Bibliography

[1] H. Fritzsch, M. Gell-Mann, 16^{th} Int. Conf. on High Energy Physics, Chicago (1972)
H. Fritzsch, M. Gell-Mann, H. Leutwyler, Advantages of the color octet gluon picture, Phys. Lett. **B47**, 365 (1973)
D. Gross, F. Wilczek, Ultraviolet Behaviour of Non Abelian Gauge theories, Phys. Rev. Lett. **30**, 1343 (1973)
H.D. Politzer, Reliable perturbative results for strong interactions?, Phys. Rev. Lett. **30**, 1346 (1973)

[2] S. Bethke, S. Catani, A summary of α_s measurements, CERN-TH. 6484/92

[3] Particle Data Group, Phys. Rev. **D45** (1992)

[4] U. Amaldi, W. de Boer, P.H. Frampton, H. Furstenau, Phys. Lett. **B281**, 374 (1992)

[5] W.J. Marciano, Flavor thresholds and Λ in the modified minimal-substraction scheme, Phys. Rev. **D29**, 580 (1984)

[6] S. Bethke, Hadronic physics in electron-positron annihilations, HD-PY 93/7

[7] S. Bethke, J.E. Pilcher, Tests of perturbative QCD at LEP, HD-PY 92/06 In Jackson, J.D. (ed.) et al. Annual review of nuclear and particle science 251-289

[8] OPAL Collaboration, P.D. Acton et al., A global determination of $\alpha_s(\mu^2)$ at LEP, Z. Phys. **C55**, 59 (1992)

[9] I. Hinchliffe, Status of α_s Measurements, LBL-33952 (1993)

[10] G. Grunberg, Renormalization group improved perturbative QCD, Phys. Lett. **B95**, 70 (1980)

[11] P.M. Stevenson, Resolution of the renormalization scheme ambiguity in perturbative QCD, Phys. Lett. **B100**, 61 (1981)
Optimization and the ultimate convergence of QCD perturbative theory, Nucl. Phys. **B231**, 65 (1984)

[12] S.J. Brodsky, G.P. Lepage, P.B. Mackenzie, On the elimination of scale ambiguities in perturbative quantum chromodynamics, Phys. Rev. **D28**, 228 (1983)
G. Grunberg, Renormalization scheme invariant QCD and QED. The method of effective charges, Phys. Rev. **D29**, 2315 (1984)
A. Dahr,V. Gupta, New perturbative approach to renormalizable field theories, Phys. Rev. **D29**, 2822 (1984)

H.J.Lu, S.J. Brodsky, Relating physical observables in QCD without scale - scheme ambiguity, Phys. Rev. **D48**, 3310 (1993)

[13] E665 Collaboration, M.R. Adams, et al., First Measurements of Jet Production Rates in Deep-Inelastic Lepton-Proton Scattering, Phys. Rev. Lett. **69**, 1026 (1992)
E665 Collaboration, M.R. Adams, et al., Q^2 Dependence of the Average Squared Transverse Energy of Jets in Deep Inelastic Muon-Nucleon Scattering with Comparison to QCD, Fermilab-Pub-93/171-E

[14] U. Bassler, G. Bernardi, Progress on Kinematical Variables Reconstruction. Consequences for DIS Physics Analysis at low x, H1 internal report H1-03/93-274
S.Bentvelsen, J. Engelen, P. Kooijman, Reconstruction of (x, Q^2) and extraction of structure functions in neutral current scattering at HERA, Proc. Workshop 'Physics at HERA', DESY, Hamburg, Vol. 1, 23 (1991)
K.C. Höger, Measurement of x, y, Q^2 in neutral current events, Proc. Workshop 'Physics at HERA', DESY, Hamburg, Vol. 1, 43 (1991)
H. Chaves, R.J. Seifert, G. Zech, Kinematic fitting, in neutral current events Proc. Workshop 'Physics at HERA', DESY, Hamburg, Vol. 1, 57 (1991)

[15] V.Hedberg, G. Ingelman, C.Jacobsson, L. Jönsson, Study of Jet Asymmetries in jet azimuthal angle distributions as a test of QCD Proc. Workshop 'Physics at HERA', DESY, Hamburg, Vol. 1, 331 (1991)

[16] CTEQ Collaboration, edited by G. Sterman, Handbook of Perturbative QCD, and references therein, Fermilab-Pub-93/094

[17] H. Plothow-Bech, PDFLIB: Nucleon, Pion and Photon Parton Density Functions and α_s Calculations CERN-PPE W5051 1993.08.30

[18] K. Charchula, PAKPDF, Version 1.2, A Fortran Package of Parametrizations of Parton Distribution Functions in the Proton

[19] H1 Collaboration, I. Abt et al., Measurement of the proton structure function F_2 (x, Q^2) in the low x region at HERA, Nucl.Phys. **B407**, 515 (1993)

[20] J.E. Huth et al, Towards a Standardization of Jet Definitions, Fermilab-Conf-90/249-E

[21] JADE Collaboration, W. Bartel, et al., Experimental studies on multi - jet production in e^+e^- annihilation at PETRA energies, Z. Phys. **C33**, 23 (1986)

[22] R. Nisius, H1 Internal Panel A meeting 16/6/1991

[23] Ch. Berger, R. Nisius as contribution to D. Graudenz, N. Magnussen, Jet cross section in deeply inelastic scattering at HERA, Proc. Workshop 'Physics at HERA', DESY, Hamburg, Vol. 1, 261 (1991)

[24] S. Catani, Yu.L. Dokshitzer, B.R. Webber, The k_t algorithm for Jets in Deep Inelastic Scattering and Hadron Collisions, CERN-TH. 6473/92

[25] B.R. Webber, Factorization and Jet Clustering Algorithms for DEEP Inelastic Scattering CERN-TH. 6871/93

[26] R.D. Peccei, R. Rückl, energy flow and energy correlations in deep inelastic scattering. Nucl.Phys. **B162**, 125 (1980)
QCD and the transverse properties of jets in deep inelastic scattering, Nucl. Phys **B182**, 21 (1980)

[27] Ch. Rumpf, G. Kramer, J. Willrodt,Jet cross-sections in leptoproduction from QCD, Z. Phys. **C7**, 337 (1981)

[28] J.G. Körner, E. Mirkes, G.A. Schuler, Int. J. Mod. Physics **A4**, 1781 (1989)

[29] D. Graudenz, Der Drei-Jet-Wirkungsquerschnitt zur Ordnung α_s^2 in der Tief-inelastischen Elektron-Proton-Streuung, PhD thesis Hamburg (1990) (in German)
D. Graudenz, Three-Jet Production in Deep-Inelastic Electron-Proton Scattering to Order α_s^2, DESY 90-095
D. Graudenz, Phys. Letters **B256**, 518 (1991)
D. Graudenz, Next-to-Leading Order QCD Corrections to Jet Cross Sections and Jet Rates in Deeply Inelastic Electron Proton Scattering, Phys. Rev. **D49**, 3291 (1994)

[30] T. Brodkorb, J.G. Körner, Z. Phys. **C54**, 519 (1992)

[31] D. Graudenz, PROJET Jet Cross Sections in Deeply Inelastic Electron Proton Scattering Version 3.6 (1993) (unpublished program manual)

[32] JADE-Collaboration, A comparison of measured jet cross sections with QCD calculations for e^+e^- annihilation Z. Phys. **C49**, 29 (1991)

[33] The ALEPH Collaboration, Measurement of α_s in Hadronic Z Decays Using All-Orders Resummed Predictions, CERN-PPE/92-33

[34] NMC Collaboration, Quark and gluon distributions and α_s from nucleon structure functions at low x Phys. Lett. **B309**, 222 (1993)

[35] A. Kwiatkowski, H. Spiesberger, and H.-J. Möhring, Comput. Phys. Commun. **69**, 155 (1992), and references therein A. Kwiatkowski, H. Spiesberger, and H.-J. Möhring, HERACLES 4.1 An event generator for *ep* interactions at HERA including radiative processes Proc. Workshop 'Physics at HERA', DESY, Hamburg, Vol. 3, 1294 (1991)

[36] LEPTO52 unpublished program manual

[37] G.A. Schuler, H. Spiesberger, DJANGO the interface for the event generators HERACLES and LEPTO Proc. Workshop 'Physics at HERA', DESY, Hamburg, Vol. 3, 1419 (1991)

[38] B.R. Webber, HERWIG DESY 91-048, and references therein

[39] G. Ingelman, "LEPTO 6.1", Proc. Workshop 'Physics at HERA', DESY, Hamburg, Vol. 3, 1366 (1991)

[40] T. Sjöstrand and M. Bengtsson, The lund monte carlo for jet fragmentation and e^+e^- physics, JETSET VERSION 6.3, an update, Comput. Phys. Commun. **43**, 367 (1987)
PYTHIA 5.6 and JETSET 7.3, Physics and manual CERN-TH. 6488/92

[41] L. Lönnblad, ARIADNE version 4.03, Comput. Phys. Commun. **71**, 15 (1992), and references therein

[42] G. Altarelli, G. Martinelli, Transverse momentum of jets in electroproduction from Quantum Chromodynamics, Phys. Lett. **B76**, 89 (1978)

[43] H1 Collaboration, I. Abt et al., The H1 detector at HERA, DESY 93-103 (1993), to be submitted to Nucl. Instr. and Meth.

[44] H1 Calorimeter Group, B. Andrieu et al., The H1 Liquid Argon Calorimeter System, Nucl. Instr. and Meth. **A336**, 460 (1993)

[45] H1 Calorimeter Group, B. Andrieu et al., Results from Pion Calibration Runs for the H1 Liquid Argon Calorimeter and Comparisons with Simulations, Nucl. Instrum. Meth. **A336**, 499 (1993)

[46] H1 Collaboration, I. Abt, et al., A Measurement of multi-jet rates in deep inelastic scattering at HERA, Z. Phys. **C61**, 59 (1994)

[47] H1 Collaboration, T. Ahmed et al., Measurement of the hadronic final state in deep inelastic scattering at HERA Phys. Letters **B298**, 469 (1993)

[48] W. de Boer, Review of QCD at LEP and SLC, IEKP-KA/90-06

[49] V.Hedberg, G. Ingelman, C.Jacobsson, L. Jönsson, Study of Jet Reconstruction Algorithms for HERA *ep* collider events, DESY 93-190

[50] F. James, M. Roos MINUIT program manual

List of Figures

List of Tables

Danksagung

Zuvorderst danken möchte ich Herrn Prof. Dr. Christoph Berger, der mich auf das bearbeitete Forschungsthema aufmerksam gemacht hat und die unverzichtbare Kooperation zwischen Experimentatoren und Theoretikern initiierte und nachhaltig förderte. Besonders danken möchte ich ihm für sein in mich und meine Forschungstätigkeit gesetztes Vertrauen und seine motivierende Fähigkeit, den Blick auf das Wesentliche zu lenken.

Dr. Dirk Graudenz gilt mein Dank für die Einweihung in einige der Geheimnisse der perturbativen QCD, für seine Geduld in vielen für mich erhellenden Diskussionen und nicht zuletzt für die Bereitstellung des PROJET Monte Carlos und seine permanente Kooperation bei der Adaption von PROJET an die Bedürfnisse eines Hochenergieexperimentes.

Herrn Prof. Dr. Siegfried Bethke danke ich für die Übernahme des Korreferates und für die Bereitstellung von Ergebnissen anderer Experimente zur Messung der starken Kopplungskonstanten. Mein besonderer Dank gilt jedoch seiner vielfältigen, freundlich gewährten Unterstützung während der Erstellung dieser Arbeit.

Dr. Gunnar Ingelman erschloß mir die physikalische Basis und Programimplementation der Parton-Schauer in LEPTO.

Dr. Peter Schleper hat in vielen Diskussionen meinen Blick für die Eigenschaften des H1 Detektors geschärft und mir, mit seinem Wissen über die Tücken der H1 Software, eine Menge Arbeit erspart. Ihm und Lynn Johnson danke ich für die Durchsicht der Rohfassungen des Manuskriptes. Sie haben nachhaltig dazu beigetragen dem geneigten Leser das Nachvollziehen meiner Gedankengänge zu erleichtern, und die Sprache wurde durch ihren Einfluß der englischen näher gebracht.

Viele haben in ihnen eigener Weise zum Gelingen dieser Arbeit beigetragen, ob ihrer Diskussionsbereitschaft möchte ich neben den oben genanten Personen namentlich den Herren Dr. Albert De Roeck, Peter Lanius, Richard Kaschowitz, Thomas Merz und Christian Leverenz danken.

Die Deutsche Forschungsgemeinschaft erleichterte mir die Konzentration auf meine Forschungstätigkeit durch die im Rahmen des Graduierten-Kollegs, *Starke und elektroschwache Wechselwirkung bei hohen Energien*, der RWTH Aachen gewährte Unterstützung.

Ich danke dem DESY Direktorat für die Bereitstellung der Arbeitsmöglichkeiten bei DESY in Hamburg und allen Mitarbeitern von HERA und H1 für die erfolgreiche Datennahme, welche die Basis meiner Untersuchungen darstellt.

Mein Dank gilt auch dem Deutschen Steuerzahler, der mir in diesen wirtschaftlich schwierigen Zeiten dennoch die Möglichkeit gab, in internationaler Zusammenarbeit Grundlagenforschung zu betreiben, welche nicht kurzfristig profitorientiert ist, sondern erkenntnisstrebend.

Lebenslauf

20.07.61	geboren als Sohn der Hausfrau Käthe Nisius geb. Holzapfel und des Bundesbankbeamten Aloys Nisius in Aachen
1967 – 1971	Besuch der Grundschule Franzstraße in Aachen
1971 – 1980	Besuch des Couven – Gymnasium in Aachen bis zum Abitur
01.07.80 – 30.6.82	Soldat bei der Bundeswehr
Okt 82	Beginn des Studiums der Physik an der RWTH-Aachen
26.04.85	Abschluß der Vordiplomprüfungen
März 1987	Beginn der Diplomarbeit am I Phys. Inst. im Rahmen des Fréjus Experimentes
Okt 1989	Abgabe der Diplomarbeit mit dem Titel: Suche nach Oszillationen atmosphärischer Neutrinos mit dem Fréjus Detektor, PITHA-89/21
21.05.90	Abschluß der Diplomprüfungen
seit 13.10.90	Mitarbeiter der H1 Gruppe F34 bei DESY
seit 01.01.92	Promotionsstipendiat der DFG